



저작자표시-비영리-변경금지 2.0 대한민국

이용자는 아래의 조건을 따르는 경우에 한하여 자유롭게

- 이 저작물을 복제, 배포, 전송, 전시, 공연 및 방송할 수 있습니다.

다음과 같은 조건을 따라야 합니다:



저작자표시. 귀하는 원저작자를 표시하여야 합니다.



비영리. 귀하는 이 저작물을 영리 목적으로 이용할 수 없습니다.



변경금지. 귀하는 이 저작물을 개작, 변형 또는 가공할 수 없습니다.

- 귀하는, 이 저작물의 재이용이나 배포의 경우, 이 저작물에 적용된 이용허락조건을 명확하게 나타내어야 합니다.
- 저작권자로부터 별도의 허가를 받으면 이러한 조건들은 적용되지 않습니다.

저작권법에 따른 이용자의 권리는 위의 내용에 의하여 영향을 받지 않습니다.

이것은 [이용허락규약\(Legal Code\)](#)을 이해하기 쉽게 요약한 것입니다.

[Disclaimer](#)

Thesis submitted in partial fulfillment
for the M. Sc. Degree requirement

Pressure-Induced Structural Changes in Sodium-
Aluminosilicate Glasses and Crystalline Magnesium-
Silicates using High-Resolution Solid-State NMR and
Quantum Chemical Calculations: Implications for Atomic
Structure of Melts in Earth's interior

2 차원 고상 핵자기공명 분광장치와 양자화학 계산을
이용한, 압력에 의한 비정질 Na-알루미노 규산염과
결정질 Mg-규산염 광물의 원자 구조변화: 지구 내부의
규산염 용융체의 고압 구조에 대한 고찰

Yi Yoo Soo

The Faculty of Graduate Studies
Seoul National University
School of Earth and Environmental Science

February 2010

Pressure-Induced Structural Changes in Sodium-
Aluminosilicate Glasses and Crystalline Magnesium-
Silicates using High-Resolution Solid-State NMR and
Quantum Chemical Calculations: Implications for Atomic
Structure of Melts in Earth's interior

2 차원 고상 핵자기공명 분광장치와 양자화학 계산을
이용한, 압력에 의한 비정질 Na-알루미노 규산염과
결정질 Mg-규산염 광물의 원자 구조변화: 지구 내부의
규산염 용융체의 고압 구조에 대한 고찰

지도교수 이성근

이 논문을 석사학위 논문으로 제출함

2010 년 2 월

서울대학교 대학원

지구환경과학부

이유수 (李儒秀)

이유수의 이학석사 학위논문을 인준함

2010 년 2 월

위원장	_____ 이 용 일 _____ (인)
부위원장	_____ 이 준 기 _____ (인)
위원	_____ 이 성 근 _____ (인)

Abstract

Despite the significant importance and implications for geochemical processes in Earth's interior including chemical differentiation, the pressure-induced changes in atomic configurations of silicate glasses and melts and their densification mechanisms at high pressure have not been well understood due to the lack of suitable experimental techniques and theoretical methods. The recent progresses and advances in high-resolution solid-state NMR, synchrotron X-ray Raman scattering, and first-principle calculations allow us to investigate the previously unknown details of the pressure-induced structural changes in silicate glasses and melts at high pressure. In this study, we explored the effect of Na content on the pressure-induced structural and topological changes in the aluminosilicate glasses using 2-dimensional triple-quantum (3Q) magic-angle spinning (MAS) NMR (in Chapter 1). We also explore the pressure-induced changes in local electronic bonding structures of diverse crystalline Mg-silicate polymorphs using first-principle calculations to have better insight into the experimental X-ray Raman scattering spectra for silicate glasses and the nature of bonding transitions in oxides at high pressure in general (in Chapter 2).

In chapter 1, we present the ^{27}Al and ^{17}O MAS and 2D 3QMAS NMR spectra for peralkaline, partially depolymerized Na-aluminosilicate glasses with varying chemical composition and pressure from 1 atm to 8 GPa. The

current results show that the higher degree of polymerization of silicate melts at ambient pressure could facilitate a further polymerization of silicate melts at high pressure at the expense of non-bridging oxygen. The degree of polymerization in Na-aluminosilicate glasses, therefore, increases with increasing pressure but decreases with network modifying Na content, while the nature of polymerization in silicate melts at high pressure affects their macroscopic properties of silicate melts at high pressure.

In chapter 2, we present the results of theoretical calculations of oxygen K-edge features for MgSiO_3 and SiO_2 crystalline polymorphs based on full-potential linearized augmented plane wave (LAPW) methods. The calculated oxygen K-edge electron excitation spectra for various crystalline Mg-silicates (e.g., x-ray absorption spectroscopy, electron energy loss spectroscopy, and x-ray Raman scattering spectroscopy) show that diverse oxygen configurations in these high pressure polymorphs have characteristic oxygen K-edge features. Particularly, a corner-sharing oxygen (${}^{[6]}\text{Si-O-}{}^{[6]}\text{Si}$) in MgSiO_3 perovskite leads to a oxygen K-edge features around 540 eV while a edge-sharing oxygen (${}^{[6]}\text{Si-O-}2{}^{[6]}\text{Si}$) in MgSiO_3 post-perovskite results in features around 545 eV. This trend and a magnitude of changes (≈ 5 eV) are similar to what has been reported for pressure-induced changes in oxygen K-edge features in MgSiO_3 glasses. As the edge-sharing oxygen in MgSiO_3 post-perovskite has similar atomic configuration with that of oxygen tri-clusters (i.e., oxygen coordinated by three highly coordinated Si atoms), the current results imply that the previous assignment of the ≈ 545 eV feature as oxygen tri-cluster in Mg-silicate glass

at high pressure about 20 GPa is likely to be correct. The experimental and theoretical results and methods in the current study will provide improved understanding of the atomistic origins of diverse macroscopic properties and geophysical and geochemical properties in Earth's interior.

Key Words: Na-aluminosilicate glass, high pressure, network modifying cation, NMR, Mg-silicates, oxygen K-edge

Student Number: 2008-20409

Table of Contents

Introduction	1
1. The Effect of Network Modifying Cation on Pressure-Induced Structural Changes in Na-aluminosilicate glasses and melts: high-resolution solid-state NMR study	4
1.1. Introduction	4
1.2. Theoretical Backgrounds.....	5
1.2.1. <i>Introduction to NMR Spectroscopy</i>	5
1.2.2. <i>Principles of NMR Spectroscopy</i>	7
1.2.3. <i>Natures of Glasses and Melts</i>	14
1.3. Results and Discussions	16
1.3.1. <i>Experiments</i>	16
1.3.2. <i>Results</i>	18
1.3.3. <i>Discussions</i>	23
2. Theoretical Studies of the Local Electronic Environments of Oxygen in Mg-silicates at high pressure using ELNES (Energy-Loss Near-Edge Structure)	44
2.1. Introduction	44
2.2. Theoretical Backgrounds.....	47
2.2.1. <i>Principles of Non-Resonant X-ray Raman Scattering Spectroscopy</i>	47
2.2.2. <i>Principles of the First-Principle Calculation Methods</i>	54
2.3. Results and Discussions	61
2.3.1. <i>Experiments and Calculations</i>	61
2.3.2. <i>Results</i>	64
2.3.3. <i>Discussion</i>	69
3. Conclusion	72
References	86
국문 요약	91
감사의 글	94

List of Figures and Tables

Figure 1. The ^{27}Al 1D MAS spectra of Na-aluminosilicate glasses with varying pressure	27
Figure 2. The ^{27}Al 2D 3QMAS spectra of Na-aluminosilicate glasses with varying pressure (total 20 contour lines are drawn from 4 to 98%).....	28
Figure 3. The proportion of each $^{\text{IV}}\text{Al}$ in Na-aluminosilicate glasses with varying pressure	29
Figure 4. The average coordination number of Na-aluminosilicate glasses at 6 GPa.....	30
Figure 5. The overlapped ^{27}Al 2D 3QMAS spectra of Na-aluminosilicate glasses at ambient pressure.....	31
Figure 6. The isotropic projection of ^{27}Al 2D 3QMAS spectra of Na-aluminosilicate glasses at ambient pressure	32
Figure 7. The quadrupolar coupling products (P_q) of ^{27}Al in Na-aluminosilicate glasses with varying pressure	34
Figure 8. The ^{17}O 1D MAS spectra of Na-aluminosilicate glasses with varying pressure	35
Figure 9. The ^{17}O 2D 3QMAS spectra of Na-aluminosilicate glasses with varying pressure (total 20 contour levels from 4 to 98%, added lines at 5 and 6.5%)	36
Figure 10. The isotropic projection of ^{17}O 2D 3QMAS spectra of Na-aluminosilicate glasses.....	37
Figure 11. The schematic picture of atomic structure of polymerization process in Na-aluminosilicate glasses. (A) $^{\text{IV}}\text{Si-O-}^{\text{IV}}\text{Al} + \text{Na-O-}^{\text{IV}}\text{Si}$. (B) $^{\text{IV}}\text{Si-O-}^{\text{V}}\text{Al} + \text{Na}^*$	38
Figure 12. The proportion of $^{\text{IV}}\text{Al-O-}^{\text{IV}}\text{Al}$ high energy cluster in NAS150520 glasses with varying pressure.....	39
Figure 13. The quadrupolar coupling products (P_q) of ^{17}O in Na-aluminosilicate glasses with varying pressure (P_q values are estimated from its peak position except $^{\text{IV}}\text{Si-O-}^{\text{IV}}\text{Si}$ which is calculated from its center of gravity of peak.).....	41

Figure 14. The schematic picture of atomic structure for decreasing $^{44}\text{Si-O-}^{44}\text{Si}$ bond angle	42
Figure 15. The pressure dependence of Ar gas solubility of Anorthite ($\text{CaAl}_2\text{Si}_2\text{O}_8$) glasses [15, 17, 18]	43
Figure 16. The crystal structures of SiO_2 and MgSiO_3 polymorphs. (A) the crystalline SiO_2 polymorphs; alpha-quartz, coesite, stishovite. (B) the crystalline MgSiO_3 polymorphs; ilmenite, ortho-enstatite (pyroxene), perovskite, post-perovskite	76
Figure 17. The oxygen K-edge experimental XRS and calculated ELNES spectra of alpha-quartz and crystalline MgSiO_3 polymorphs	77
Figure 18. The calculated and experimental results of SiO_2 alpha-quartz. (A) the oxygen K-edge ELNES spectra. (B) the partial density of states (p-DOS) of oxygen. (C) the directional components in p-orbital of oxygen.....	78
Figure 19. The calculated results of SiO_2 coesite. (A) the oxygen K-edge ELNES spectra. (B) the partial density of states of oxygen. (C) the directional components in p-orbital of oxygen.....	79
Figure 20. The calculated results of SiO_2 stishovite. (A) the oxygen K-edge ELNES spectra. (B) the partial density of states of oxygen. (C) the directional components in p-orbital of oxygen.....	80
Figure 21. The calculated and experimental results of MgSiO_3 pyroxene (Py; ortho-enstatite). (A) the oxygen K-edge ELNES spectra. (B) the partial density of states of oxygen. (C) the directional components in p-orbital of oxygen.....	81
Figure 22. The calculated and experimental results of MgSiO_3 ilmenite (ilm). (A) the oxygen K-edge ELNES spectra. (B) the partial density of states of oxygen. (C) the directional components in p-orbital of oxygen.....	82
Figure 23. The calculated and experimental results of MgSiO_3 perovskite (Pv). (A) the oxygen K-edge ELNES spectra. (B) the partial density of states of oxygen. (C) the directional components of p-orbital of oxygen.....	83
Figure 24. The calculated results of MgSiO_3 post-perovskite (pPv). (A) the oxygen K-edge ELNES spectra. (B) the partial density of states of oxygen. (C) the directional components in p-orbital of oxygen.	84

Figure 25. The oxygen K-edge XRS spectra of MgSiO_3 glasses at 1 atm and ≈ 39 GPa and calculated ELNES spectra of MgSiO_3 perovskite (Pv) and post-perovskite (pPv)..... 85

Table 1. The composition of prepared sample..... 26

Table 2. The isotropic chemical shift of ^{27}Al in Na-aluminosilicate glasses. 33

Table 3. The proportion of $^{[4]}\text{Al}$ -O- $^{[4]}\text{Al}$ in NAS150520..... 40

Table 4. The crystallographic information of SiO_2 and MgSiO_3 polymorphs 75

Introduction

Aluminosilicate glasses and melts are one of the most common components of magmatic melts in Earth's interior, thus affect to the geophysically and geochemically important properties such like densification of magmatic melts, seismological anomalies in core-mantle boundary, and elements partitioning between silicate melts and crystals, etc. There exist many fundamental questions of aluminosilicate melts at Earth's deep inside; how does the local structure of silicate melts changes at high pressure, how this distorted local atomic structure affects to their macroscopic and thermodynamic properties, and also global geological processes. In spite of these importances of exploring the properties of aluminosilicate melts and glasses, the pressure-induced structural changes and their compositional effect on local atomic structure have not been fully understood, even though there have been enormous advances in both optical spectroscopic techniques for exploring the atomic structure of amorphous materials and experimental probes to reconstruct the extreme condition relevant to Earth's interior.

Recent advances in spectroscopic techniques especially for solid-state NMR with developments of experimental techniques, which could realize a relatively high pressure condition relevant to Earth's interior, allow us to explore the atomic structure of aluminosilicate glasses synthesized at high pressure. The structure of aluminosilicate glasses

synthesized at high pressure have been studied particularly about their ordering behavior of framework cation, however the fundamental effect of network modifying cation on structural changes with increasing pressure has not been understood clearly including the densification mechanism of multi-component melts in Earth's interior. The quantum chemical calculations provide the complementary insight about the valuable properties of silicate glasses and amorphous structure at extreme condition relevant to Earth's deep inside, where it is very difficult and laborious doing in-situ experiments the materials of Earth's deep inside. The theoretical approaches of exploring Earth materials are relatively easy to access the extreme pressure-temperature condition than the experimental apparatus, since the improvement of computation techniques provides the accurate results comparing with corresponding experimental results.

In this paper, we worked about mainly two topics of exploring Earth materials. In the first chapter, we present our recent NMR results which show the effect of network modifying cation on pressure-induced structural changes of Na-aluminosilicate glasses including its implications to the properties of magmatic melts at Earth's interior. In the second chapter, we present the theoretical studies of oxygen K-edge excitation spectra of crystalline Mg-silicate polymorphs to investigate their electronic bonding structure, and apply to understanding the not well-known electronic bonding structure of amorphous MgSiO_3 at high pressure. From the applications of these new and advanced techniques, high resolution solid-state NMR and first-principle calculations which have being

developed recently, we could note that these experimental and theoretical approaches to Earth materials at high pressure could shed light on the numerous new and significant geophysical and geochemical applications including the atomic structure of amorphous silicate oxides at high pressure-temperatures conditions. This text is organized in 3 chapters. The first chapter shows the results and discussions of ^{27}Al and ^{17}O solid-state NMR spectroscopic experiments with briefly summarized principles of NMR spectroscopy. The second chapter shows the calculated oxygen K-edge energy-loss near-edge structure (EELS) spectra for crystalline SiO_2 and MgSiO_3 polymorphs with relevant x-ray Raman scattering spectroscopic experimental results to understand the electronic bonding structure of MgSiO_3 glass at high pressure. The third chapter shows the conclusions of this work with implications on geophysical and geophysical properties in Earth's interior.

1. The Effect of Network Modifying Cation on Pressure-Induced Structural Changes in Na-aluminosilicate glasses and melts: high-resolution solid-state NMR study

1.1. Introduction

Despite the significant importance in understanding the nature of chemical differentiation and crystal-melt partitioning of elements in Earth's interior, the pressure-induced structural changes of aluminosilicate glasses and their densification mechanisms at high pressure have not been fully understood due to the lack of suitable experimental probes. The nuclear magnetic resonance (NMR) spectroscopy, which has been used to characterize organic molecules in liquid phase, is recently advanced in high-resolution solid-state NMR spectroscopy allowing us to explore the unknown atomic structural characteristics of silicate glasses and melts. The solid-state NMR spectroscopy, thus, has made the major contributions in elucidating the atomic structure of glasses and melts. Most of the previous works of verifying structural properties of silicate glasses and melts have focused on the pressure and temperature effects on the structure of amorphous Earth materials to understand the anomalous dynamic properties of glasses and melts [1, 2]. The systematic effects of composition (i.e., the role of network modifying cation, also called network modifier) in polymerization process of melts at high pressure, therefore, remains to be

explored because of the difficulties of designing appropriate sample system; and the results are expected to provide valuable information for exploring the magmatic melts in Earth's interior more systematically.

In this study, we explore the effect of Na content on the pressure-induced structural changes in the aluminosilicate glasses using 2D 3QMAS and 1D MAS NMR experiments. The ^{27}Al and ^{17}O MAS and 2D 3QMAS NMR spectra of highly polymerized glasses (i.e., silica rich) and relatively depolymerized glasses (i.e., Na rich) quenched from melts at 1 atm, 6 GPa, and 8 GPa were prepared, details of samples are summarized in experiments section. The results from these experiments suggest the possibility of that the network modifying cation could affect the polymerization of aluminosilicate melts at high pressure, and account for densification mechanism of geophysically important magmatic melts, providing enhanced prospects for crystal-melts partitioning, and chemical differentiation of magmas in Earth's interior.

1.2. Theoretical Backgrounds

1.2.1. Introduction to NMR Spectroscopy

The NMR spectroscopy allows us to explore the element specific atomic structure different from other conventional optical spectroscopic methods. The specific transition energy of each target nucleus induced

from external magnetic field, called the Zeeman Effect, is caused from the nuclear spin number which is one of the intrinsic properties of nuclei. Then, this separated energy level is used to probe the atomic structure by comparing the nuclei specific transition energy with that of standard sample (i.e., commonly used with external reference in solid-state NMR). In spite of the various possibilities of this element specific spectroscopic technique for exploring the amorphous system, there are still remaining problems to verify the condensed phase system comparing with liquid sample because of the relatively short relaxation time of condensed sample than that of liquid sample showing broad spectrum where the delta-function like spectrum in frequency domain (i.e., has high resolution enough to reconstruct atomic structure of organic materials in liquid phase such as protein) is appeared in liquid sample. Not only the shorter relaxation time but also the various quantum mechanical perturbations such as quadrupolar coupling effect affect to the NMR spectrum of solid-state sample. Several methods have been developed to improve the resolution of NMR spectrum with decreasing the perturbation effects for exploring the atomic structure of solid-state sample; DAS (dynamic angle spinning), MAS (magic angle spinning), and MQMAS (multiple-quantum transition MAS) [3-5].

The experimental results of NMR spectroscopy provide the atomic structural disorder of silicate glasses such as chemical short-range order distribution (i.e., especially the oxygen linkages in this work; Si-O-Si, Si-O-Al, etc.) and topological disorder which shows the state of order that stems

from the bond angle and bond length distribution of the system. From this information obtained from solid-state NMR spectroscopy, we could investigate structure of amorphous materials including silicate oxide glasses and melts.

1.2.2. Principles of NMR Spectroscopy

The briefly summarized methodologies of NMR spectroscopy are referred from following materials [3-7].

(i) The Zeeman Effect

The nuclear magnetic effect, of which the magnetic field induces the separated energy level of nuclear spin, is used in NMR spectrometer, and this effect is called as the Zeeman Effect. This separated energy levels make the characteristic spectral feature of nucleus (i.e., induced from different spin-relaxation time) providing the NMR spectroscopic information, 1-dimensional single and 2-dimensional triple quantum magic-angle spinning (1D MAS and 2D 3QMAS) spectrum. And the energy gap of this discrete energy level increases with increasing external magnetic field strength with relatively decreasing various perturbation effects (i.e., chemical anisotropy, quadrupolar interaction, etc.).

The total Hamiltonian (H) of nucleus, which is induced by an external magnetic field (B), is affected by the various perturbation effects

(H') comes from the magnetic dipole moment (μ). The spin (S) and angular (L) momentum are coupled (J) with considering the relativistic effect (g-factor) on the nucleus. The appropriate gyromagnetic ratio '2' on the total spin momentum should be considered due to the relativistic effects.

$$\hat{H} = \hat{H}_0 + \hat{H}', \quad \hat{H}' = -\vec{\mu} \cdot \vec{B} \quad (1-1)$$

$$\vec{\mu} = -\mu_B g \vec{J}, \quad \vec{J} = \vec{L} + 2 \cdot \vec{S} \quad (1-2)$$

(ii) Fundamental properties of spin and NMR signal

The external magnetic field induces not only the splitting of energy level but also the Larmor precession which is exerted by the torque between magnetic dipole moment of nuclear spin and external magnetic field (i.e., This description is a macroscopic view, the atomic origins of the Larmor precession comes from the general solution of time-dependent of Schrödinger equation solving spin-orbital function, the expectation S_x and S_y component oscillate with corresponding Larmor frequency with respect to z-axis external magnetic field.). The Larmor frequency (ω_0) provides an information of the frequency domain (ppm = frequency shift/ ω_0) in NMR spectrum. The FID (free induction decay) signal of NMR experiment is acquired with spin polarization induced from stimulating RF field of NMR spectrometer. This spin polarization provides the two intrinsic properties of the spin system called the spin-lattice relaxation (T_1) and transverse relaxation (T_2), and then the NMR spectrometer measures this relaxation signal radiated from the spin precession. This detected FID signal is transformed into frequency domain with the Fourier transformation

providing the chemical shift information which is originated from the magnetic shielding by local electronic environment.

(iii) Differences between the solid and liquid-state NMR spectroscopy

The NMR spectroscopy, especially the liquid-state NMR spectroscopy, has been being used in bio-science to investigate the multi-atomic molecular structure like protein with its high atomic structure resolving abilities in liquid phase sample; because the peak shape is similar to delta-function in the liquid-state NMR spectrum due to the decreasing of quantum mechanical perturbations including quadrupolar coupling effect which takes most part of the perturbation effects in solid-state NMR system. The isotropic liquids have a few percents of quadrupolar effect even the anisotropic liquids (i.e., the dipole-dipole coupling, quadrupolar coupling effect, etc.). These quantum mechanical perturbation effects make the peak shape broader than that of solid-state system, henceforth the spectrum is harder to resolve in frequency domain.

**(iv) The methods for reducing quantum mechanical perturbations
Magic-angle spinning (MAS) method**

The conventional NMR techniques of liquid-state NMR spectroscopy could not be used in exploring the atomic structure of solid phase materials. However, the recent advances in NMR techniques of solid-state NMR spectroscopy allow us to resolve the atomic structure of solid-state materials using NMR spectroscopy. There are many theoretical and

mechanical methods which could improve the resolution of peak with reducing or deselecting the perturbation effects induced from neighboring nucleus. One of the most used mechanical techniques is called MAS of which the sample rotor is spun in specific angle (i.e., magic angle; $3\cos^2\theta - 1 = 0$) to improve the peak resolution with removing the first order perturbation effect which comes from the chemical anisotropy of sample (H_{CS}) and makes the chemical shift anisotropy (δ_{CSA}).

$$H_{CS} \propto [\gamma B_0 + \{\delta_{iso} + \frac{1}{2} \delta_{CSA}(3 \cos^2 \theta - 1)\}] \quad (1-3)$$

Quadrupolar effect

The internal Hamiltonian of the nucleus has various perturbation terms, mainly first and second order perturbation effects; the first order perturbation effect is induced from the chemical shift anisotropy, dipolar coupling interactions, etc.; the second order perturbation effect is quadrupolar interaction. The second order quadrupolar interaction remains even though the chemical shift anisotropy is almost removed by MAS method; and this remaining quadrupolar interaction could be reduced in two ways. The first one is the stronger external magnetic field; the high magnetic field increases the Zeeman Effect and relatively reduces the perturbation effects. The other method averages the perturbation effects using mechanical probe called dynamic angle spinning (DAS); rotor is rotated in two specific angles, 37.38° and 79.19° and the corresponding equations are presented at below with tensor notation (i.e., the

conventionally expressed equations are could be found at related references).

$$\omega_Q^{(1)} = \frac{e^2 q Q}{4I(2I+1)} \{3m^2 - I(I+1)\} W_{20}^Q \quad (1-4)$$

$$\omega_Q^{(2)} = - \left(\frac{e^2 q Q}{4I(2I-1)} \right)^2 \frac{2}{\omega_0} m \cdot [\{I(I+1) - 3m^2\} V_{00}^Q + \{8I(I+1) - 12m^2 - 3\} V_{20}^Q + \{18I(I+1) - 34m^2 - 5\}] V_{40}^Q \quad (1-5)$$

$$V_{k0}^Q = \sum_n D_{n0}^k(\alpha, \beta, \gamma) A_{kn} \quad (1-6)$$

The multiple-quantum magic-angle spinning (MQMAS) method

The multiple-quantum transition (i.e., odd number excitation; 1, 3, 5 ...) is not affected by the second order quadrupolar interaction, this MQ transition could not be observed directly, differently from single-quantum transition. The quantum transition is treated as simple quantum coherence; however these two concepts are different because of the number of spins in the system. The spins, which are explored with NMR spectroscopy, have to be provided with thermal sensitivity using the concept of the ensemble average. This MQ transition evolves by the RF pulse and transferred into SQ transition with their corresponding quantum coherences. The MQ transition could be observed indirectly with varying evolving time (t_1) as time variable used in SQ excitation relaxation time (t_2). The first order quadrupolar interaction could be effectively removed with implementing multiple-quantum transition pulse sequence without changing MAS probe. The second order quadrupolar interaction could be, then, removed with allowing the spins to evolve in two time variables (i.e., MQ evolving time

and SQ relaxation time). The isotropic spectrum, of which the quadrupolar effects are removed, could be obtained in evolution time domain (t_1) with MQ pulse sequence.

(v) The calculation of NMR parameters

The various NMR parameters presented in this article could be calculated using these equations as below. These equations are referred from previous work. The chemical shift as peak maximum position in isotropic dimension (δ_{3QMAS}) and the center of gravity of the same peak in MAS dimension (δ_{MAS}) are correlated with this equation where the second order quadrupolar coupling product (δ_{iso}^{2Q}) is represented the quadrupolar coupling product (P_q). Furthermore, this quadrupolar coupling product is related with the quadrupolar coupling constant (C_q) which expressed with the atomic symmetry parameter (η) of target nuclear. And these equations are expressed with some parameters suchlike the quadrupolar moment (eQ), the principle component of the electric field gradient (eq), and the Larmor frequency (ω_0) of target nuclide.

$$\delta_{3QMAS} = -17/31 \delta_{iso}^{CS} + 10/31 \delta_{iso}^{2Q}, \quad \delta_{MAS} = \delta_{iso}^{CS} + \delta_{iso}^{2Q} \quad (1-6)$$

$$\delta_{iso}^{2Q} = -6000 \cdot \frac{P_q^2}{\omega_0^2} \left(\text{if spin} - \frac{5}{2} \right) \quad (1-7)$$

$$P_q = C_q \left(1 + \eta^2/3 \right)^{\frac{1}{2}} \quad (1-8)$$

$$C_q = \frac{e^2 q Q}{h} \quad (1-9)$$

$$\delta_{iso}^{CS} = -\frac{31}{27}\delta_{3QMAS} + \frac{10}{27}\delta_{MAS} = \dots = -\frac{31}{17}\delta_{3QMAS} + \frac{10}{17}\left[-6000 \cdot \frac{1}{\omega_0^2} \cdot e_{2qQh1+\eta23}\right] \quad (1-10)$$

$$\delta_{iso}^{2Q} = \frac{12}{27}\delta_{MAS} - \frac{31}{27}\delta_{3QMAS} \quad (1-11)$$

$$P_q = \sqrt{-\frac{\omega_0^2}{6000}(\delta_{MAS} - \delta_{iso}^{CS})} \quad (1-12)$$

1.2.3. Natures of Glasses and Melts

We had explored the quenched silicate glasses at high pressure, and many other previous studies also had worked with quenched glasses to elucidate the various properties of materials in liquid or molten phases. The quenched silicate glasses, however, does not have same physical and structural properties compared to silicate melts. The differences between silicate melts and quenched glasses have been being debated for a long time; however that have not been being clearly distinguished till now. The quenched silicate glasses are made from silicate melts by rapidly cooling the molten materials to prevent the formation of opaque crystals; therefore the quenched glasses are also called as super-cooled liquids[8, 9].

The quenched silicate glasses are commonly treated as an amorphous solid not liquids or melts because of their similar mechanical properties to solids with extremely high viscosity, which means that the flows of quenched glasses could not be observed in experimental research time scale. This high rigidity of quenched glasses is originated from the trapped translational and rotational degree of freedom in phase space indicating the reduced atomic mobility. On the other hand, sometimes the quenched glasses are classified into liquids because of their thermodynamic characteristics. The first-order thermodynamic variables such as volume, enthalpy, and entropy are continuously changed during the glass transition, whereas the second-order thermodynamic variables like thermal expansion coefficient and heat capacity are discontinuously changed during the glass

transition. These thermodynamic characteristics indicate the distinct phase transition of quenched glasses from common phase transition between solids and liquids. The quenched glasses are stable under glass transition temperature; however that could be transformed into more relaxed structure (i.e., similar to crystalline phase) because of their relatively lower activation energy of phase transition, showing the possibility of that the quenched glasses are local-table phase at relevant condition with lower activation barrier or meta-stable phase. Although the various thermodynamic properties of quenched glasses are changed from melts during the glass transition, we expect that the atomic configuration of melts is still remained in quenched glasses because the atomic configurations are trapped in their coordination during the rapid quenching of molten materials, and then, the structural information of quenched glasses allow us explore the atomic structural and macroscopic properties of silicate melts.

1.3. Results and Discussions

1.3.1. Experiments

Sample preparations

Two different types of aluminosilicate glasses were prepared; NAS150560, NAS150540 and NAS150520 were synthesized from the mixture of Na_2CO_3 , Al_2O_3 , and 40% ^{17}O enriched SiO_2 . 0.2 wt% of cobalt oxide (i.e., Cobalt (II) Oxide: CoO) was added for reducing the spin-lattice relaxation time. The details of synthesized samples are summarized in Table 1. The glass starting materials were synthesized at 1 atm by fusing the sample mixture for 1 hrs at 1473~1773 K in a Ar gas environment tube furnace, and were loaded into a multi-anvil press apparatus with a 10/5 and 18/11 (octahedron edge length/truncated edge lengths of the anvils) assembly. The samples were fused at 1923~2173 K for 20 minutes and quenched to glasses at a pressure range of 6 and 8 GPa; the initial quench rate was estimated to be larger than 50 °C. The sample has different SiO_2 molar fraction for each composition; hence their NBO/T (i.e., the number of non-bridging oxygen per tetrahedral cation, and reflects the extent of polymerization of silicate melts varying from 0, fully polymerized to 4, fully depolymerized) values are, also, different. Highly Na contained NAS150520 has 0.67, implying more depolymerized phase; and NAS150560 has 0.29 due to the higher SiO_2 molar fraction. All the samples are explored at 1 atm condition with NMR spectrometer; ex-situ experiments. The high

pressure NAS150540 samples are synthesized by Prof. Mibe at Tokyo University, Japan for 6 and 8 GP using multi-anvil press.

NMR spectroscopy

NMR spectra of ^{27}Al and ^{17}O were collected on a Varian Solid-State NMR 400 MHz spectrometer (9.4 T) where the Larmor frequency of each ^{27}Al and ^{17}O is 104.23 and 54.23 MHz. The Varian MAS 3.2 mm double resonance probe was used with ZrO_2 rotor, which was spun at 15 kHz for magic-angle spinning experiments. For each nuclide, ^{27}Al and ^{17}O , the almost same pulse sequence (experimental condition) was used to explore the system. In the 1D MAS experiments, relaxation delay was set to 1 s with 0.3 μs RF (i.e., radio frequency) pulse length; and then this pulse enhances 15 degree tip angle for the central transition in solid materials. After that, 2D 3QMAS spectra were collected with fast amplitude modulation shifted echo pulse which is represented with two hard pulses, duration were 3 μs and 0.6 μs , and one soft pulse, duration was 1 s.

1.3.2. Results

The ^{27}Al NMR results

The ^{27}Al 1D MAS and 2D 3QMAS spectra show the oxygen coordination number of each Al site indicating the changes of local atomic structure near the Al nucleus with increasing pressure and the topological disorder of the system.

The Figure 1 and Figure 2 are ^{27}Al 1D MAS and 2D 3QMAS spectra of Na-aluminosilicate glasses, showing that the proportions of highly coordinated Al (i.e., $^{[5,6]}\text{Al}$) increase with increasing pressure. The existence of $^{[5]}\text{Al}$, which does not exist in crystalline aluminosilicate polymorphs and indicates the evidence of amorphous nature of samples synthesized at high pressure [10].

The Figure 3 shows that the proportions of pressure-induced highly coordinated Al with increasing pressure, and those highly coordinated Al sites have relatively smaller proportions in NAS150520 (i.e., highly Na contained aluminosilicate glass). The Figure 4 shows this feature more clearly; the average coordination number of Al of NAS glasses at 6 GPa, which is obtained from product of proportion and coordination number of each coordinated Al site, decreases with increasing the content of Na in the system. The proportion of each coordinated Al site was scaled with their quadrupolar efficiency because the nucleus with different magnetic shielding has different quadrupolar excitation efficiency.

Furthermore, we could observe the changes in shape of peak and its region for ambient pressure samples in Figure 5 showing distorted off-Gaussian peak, even though the conventional isotropic projection should have Gaussian-like peak for each observed component [4]. This result could be presented more clearly in isotropic projection as Figure 6, and this distortion and broadening of spectrum is obviously more progressed in NAS150520 than that of NAS150560. This distortion appeared in NAS150520 may be caused from the local inhomogeneity around the Al sites implying the increases of configurational disorder, which is induced from the Na⁺ ion in the system. And the peak position shifting is, also, observed in NAS150520 due to the relatively long range interaction of Na cation field which reduces the magnetic shielding of Al nucleus (i.e., increasing the isotropic chemical shift of Al site).

The various NMR parameters calculated from 2D 3QMAS spectra provide more detailed structural changes with increasing pressure [10]. The isotropic chemical shift of each Al site is listed in Table 2, and this value of larger in NAS150520 than that of NAS150560 about 4~5 ppm implying the reduced magnetic shielding of Al by strong cation field of Na. And those isotropic chemical shift values increase with increasing pressure suggesting the decreasing inter-atomic distance between Na and Al. The quadrupolar coupling product (P_q) in Figure 7, which reflects the local distortion of electric field gradient (EFG; positive correlation with P_q) affecting to the

magnetic shielding of Al site, of each Al site increases with increasing pressure, and this could indicate the positive correlation between pressure-induced structural changes and distortion of EFG with changes of atomic arrangements around Al sites. The drops of P_q of Al in NAS150520 indicate the possibility of that the addition of network modifying cation (Na) would enhance the depolymerization of melts at high pressure, because the decreasing of P_q represents the increased bond angle and bond length of Al sites with increasing their symmetry, which means that the network modifying cation had the capability of reducing the pressure effect on polymerization of silicate melts.

The ^{17}O NMR results

Differently from ^{27}Al NMR data, the NMR spectra of ^{17}O provide the short-range chemical order of Na-aluminosilicate glasses such as oxygen linkage connected with cation (i.e., Si-O-Si, Al-O-Si, and Na-O-Si, etc.). The Figure 8 shows the ^{17}O 1D MAS spectra of Na-aluminosilicate with varying pressure, however this result could not be resolved to identify each oxygen linkages in sample. Even the pressure effects on the system could not be distinguished in 1D MAS spectrum, the compositional differences by Na contents are verified in -50~0 ppm region indicating the proportional difference of bridging oxygen (BO) and non-bridging oxygen (NBO). The Figure 9 is the collection of ^{17}O 2D MAS spectra for Na-aluminosilicate glasses providing more resolved spectral features of the oxygen linkages than that of 1D MAS data. The decreasing proportion of

NBO and increasing proportion of ${}^4\text{Si-O-}^{[5,6]}\text{Al}$ with increasing pressure presenting the expense of NBO for forming pressure-induced highly coordinated Al sites. And the Figure 10, the total isotropic projection of ${}^{17}\text{O}$ 2D 3QMAS spectra of Na-aluminosilicate glasses manifest the increasing proportion of ${}^4\text{Si-O-}^{[5,6]}\text{Al}$ with increasing pressure more dramatically than conventional ${}^{17}\text{O}$ 2D spectra. This polymerization process of oxygen linkage at high pressure could be illustrated as Figure 11; ${}^4\text{Si-O-}^{[4]}\text{Al} + \text{Na-O-}^{[4]}\text{Si} = {}^4\text{Si-O-}^{[5]}\text{Al} + \text{Na}^*$. Not only the pressure effect on NAS glasses but also the compositional differences of samples are more clearly shown in ${}^{17}\text{O}$ 2D 3QMAS spectra; the highly Na contained NAS150520 has more NBO (i.e., $\text{Na-O-}^{[4]}\text{Si}$), and the proportion of ${}^4\text{Si-O-}^{[4]}\text{Si}$ is relatively smaller than that of NAS150560. The Figure 12 and Table 3 show the proportion of relatively high energy cluster of NAS150520, ${}^4\text{Al-O-}^{[4]}\text{Al}$, which decreases apparently with increasing pressure implying that the chemical disorder may decrease with increasing pressure and correlated with forming ${}^4\text{Si-O-}^{[5,6]}\text{Al}$ linkages at high pressure [11].

The Figure 13 provides the quadrupolar coupling products (P_q) of ${}^{17}\text{O}$ in Na-aluminosilicate glasses with varying pressure. The P_q of ${}^4\text{Si-O-}^{[4]}\text{Si}$ decreases with increasing pressure in both samples implying the possibility of decreasing bond angle of this oxygen linkage in amorphous network system at high pressure as Figure 14. The previous NMR experiments and first-principle calculation results provide the negative correlation between asymmetry parameter of oxygen and bond angle in Si-O-Si linkage while the asymmetry parameter is negatively correlated with

P_q implying the P_q implying the positive correlation between Si-O-Si bond angle and P_q in amorphous network system (i.e., vitreous silica) [12, 13]. This result (i.e., decreasing P_q of Si-O-Si linkage with increasing pressure) could suggest the formation of more confined closed-ring like atomic clusters which could be one of the densification mechanisms of silicate melts at high pressure; and this intermediate order structural change of NAS glasses could contribute to the inert gas solubility in Earth's interior [14, 15]. The P_q value of $^{[4]}\text{Si-O-}^{[4]}\text{Al}$ show a small positive correlation with pressure implying the pressure-induced inter atomic length contraction and pressure-induced densification, and the $^{[4]}\text{Si-O-}^{[5,6]}\text{Al}$ linkage has relatively larger P_q values than that of $^{[4]}\text{Si-O-}^{[4]}\text{Al}$ since the atomic structure around the highly coordinated Al would be more distorted than that of $^{[4]}\text{Al}$ site. The definite correlation between P_q of Na connected oxygen linkage (i.e., Na-O- $^{[4]}\text{Si}$) and pressure is not observed in this result. Although the pressure effects observed in ^{17}O NMR results are shown in the calculated P_q values, the compositional effect on pressure-induced structural changes or chemical disorder could not be clearly observed. This result may provide the effect of Na ion on the pressure-induced densification in NAS glasses at high pressure with enhancing the depolymerization.

1.3.3. Discussions

In this work, we explore the Na-aluminosilicate glasses synthesized at high pressure varying chemical composition to elucidate the effect of network modifying cation on pressure-induced structural changes of silicate melts using ^{27}Al and ^{17}O 1D MAS and 2D 3QMAS NMR experiments. These NMR results of NAS glasses show the polymerization occurred with increasing pressure, while the network modifying cation (i.e., Na in this case) enhances the depolymerization of silicate glasses with its strong cation field. Hence, it means that the highly polymerized silicate melts at ambient pressure can facilitate the further polymerization of high pressure with expense of non-bridging oxygen. Relatively more depolymerized silicate glass, NAS150520, might have smaller topological entropy at high pressure than that of NAS150560 because the ^{27}Al and ^{17}O 2D 3QMAS spectra and estimated quadrupolar coupling product of Al provide the lower degree of polymerization of highly Na contained glass. There exists the strong correlation between the pressure-induced structural changes of silicate glasses and their local electronic environment such as electronic field gradient around the target nuclei (i.e., the Al and O); and the strong cation field of network modifying cation also affects to the local electronic environments. The calculated P_q values of Al and O provide that the local electronic environment could be affected by not only pressure-induced structural changes but also strong cation field of Na as indicated by the changing P_q values of Al. These results demonstrate that the

network modifying cation such as Na^+ could enhance the depolymerization of aluminosilicate glasses at high pressure with its strong cation field, and also imply that the higher degree of polymerization of aluminosilicate glasses at ambient pressure can facilitate the further polymerization of glasses at high pressure at the expense of NBO (non-bridging oxygen), which is one of the substantial densification mechanisms of silicate melts at high pressure.

These atomic structural investigations of Na-aluminosilicate glasses quenched at high pressure could suggest the valuable information about the geophysical and geochemical properties in Earth's deep interior [1, 14, 15]. Our experimental results acquired from solid-state NMR provide the valuable information of atomic configurations in amorphous network system of silicate glasses, and this obtained atomic structural information causes the macroscopic properties of Earth materials with showing their local atomic structure and electronic environments. In the next two paragraphs, the applications of geophysical and geochemical properties in Earth's interior will be discussed with their atomistic origins. We explored the very simple compositional sample whereas the real magmatic melts are multi-component silicate melts at high pressure and temperature affected by the various network modifying cations like Mg, Na, and Ca, etc..

In this study, we explored the relatively lower pressure region (~ 8 GPa) where the pressure dependence of Ar solubility has linear-like positive correlation. The ^{27}Al and ^{17}O NMR experimental results provide

various evidences of structural changes of silicate glasses in this lower pressure region. The existence of highly coordinated Al and increasing P_q of Al with increasing pressure indicate the pressure-induced polymerization and distortion of local atomic structure around Al, and the decreasing P_q of $^{[4]}\text{Si-O-}^{[4]}\text{Si}$ with increasing pressure suggest a decreasing Si-O-Si bond angle in silicate amorphous network. And these local atomic structural changes of silicate melts could suggest the circumstances of pressure effects on inert gas solubility with affecting to intermediate atomic structure of silicate melts such as forming confined closed-ring like clusters with expanse of non-bridging oxygen at high pressure. The further polymerization may occur at higher pressure region which show the dramatic breakdown of the amorphous network connections to denser atomic structure including oxygen tri-clusters in silicate melts structure [16]. And these polymerizations, as the main densification mechanism of silicate melts at high pressure, should be combined with equilibration of partial pressure of inert gas molecules to see the atomistic origins of anomalous features of pressure dependence of Ar gas solubility in silicate melts represented in Figure 15.

Table 1. The composition of prepared sample

Sample	Composition	NBO/T
NAS150520	$\text{Na}_2\text{O}:\text{Al}_2\text{O}_3:\text{SiO}_2 = 15:5:20$	0.67
NAS150540	$\text{Na}_2\text{O}:\text{Al}_2\text{O}_3:\text{SiO}_2 = 15:5:40$	0.40
NAS150560	$\text{Na}_2\text{O}:\text{Al}_2\text{O}_3:\text{SiO}_2 = 15:5:60$	0.29

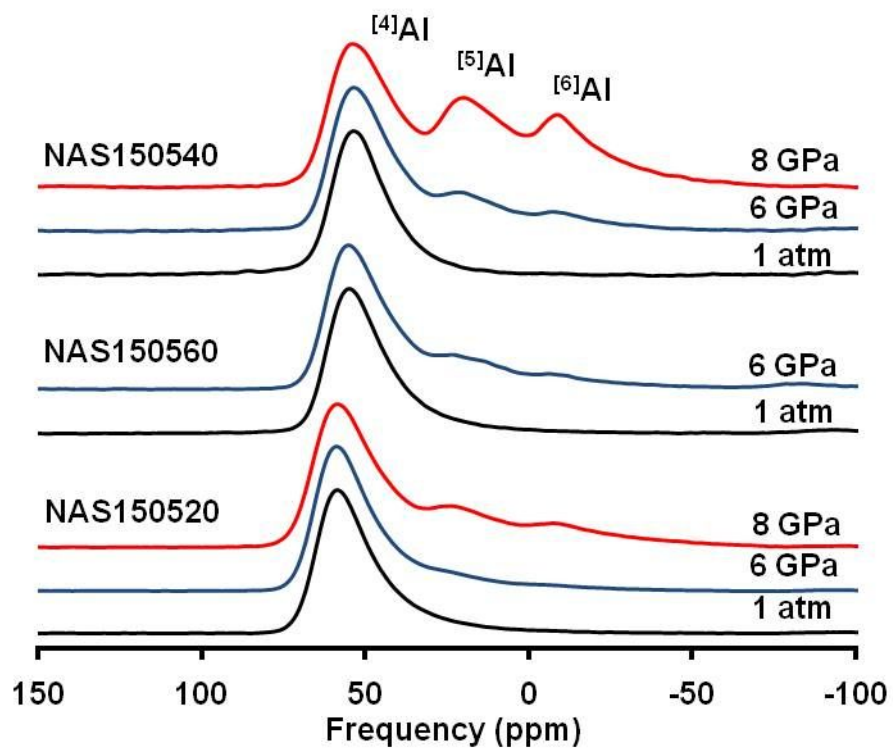


Figure 1. The ^{27}Al 1D MAS spectra of Na-aluminosilicate glasses with varying pressure

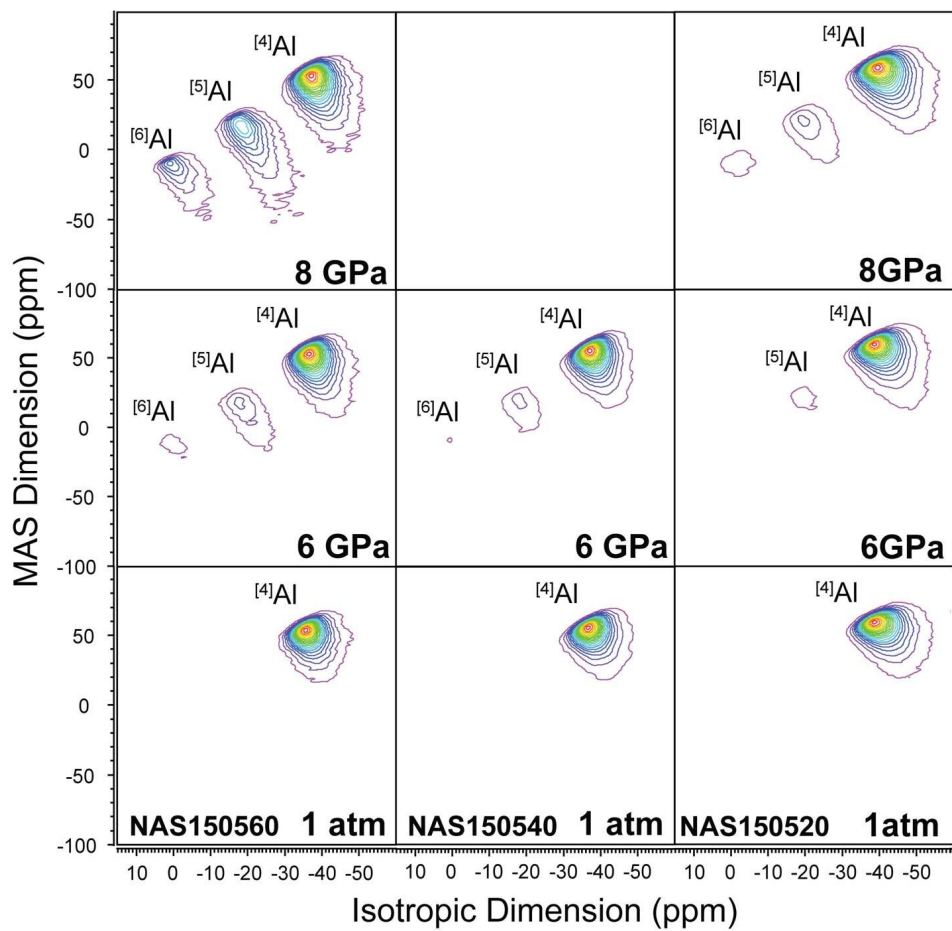


Figure 2. The ^{27}Al 2D 3QMAS spectra of Na-aluminosilicate glasses with varying pressure (total 20 contour lines are drawn from 4 to 98%)

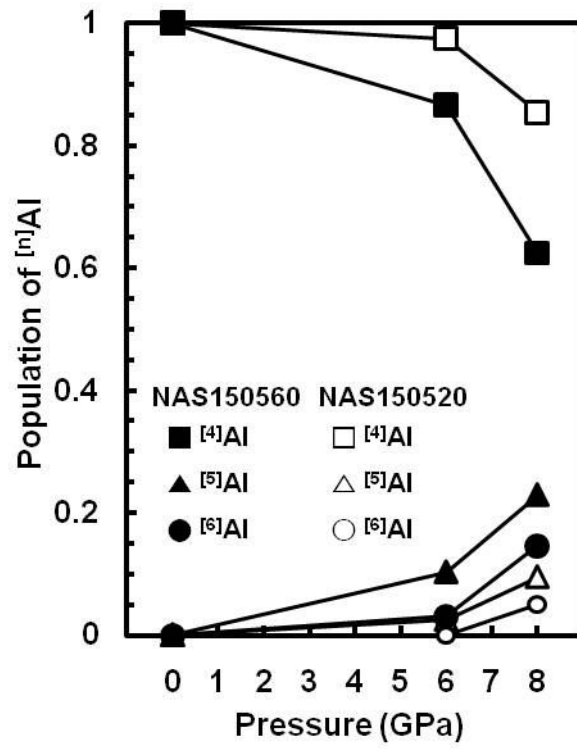


Figure 3. The proportion of each $[n]Al$ in Na-aluminosilicate glasses with varying pressure

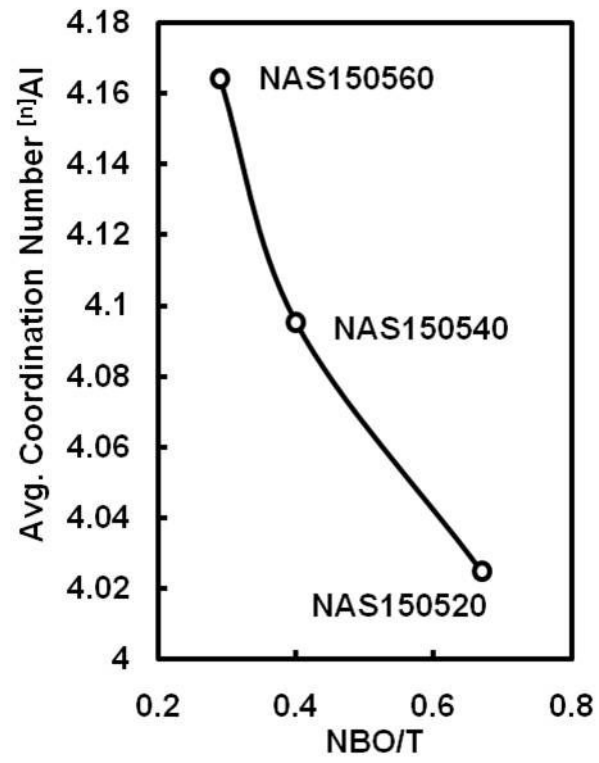


Figure 4. The average coordination number of Na-aluminosilicate glasses at 6 GPa

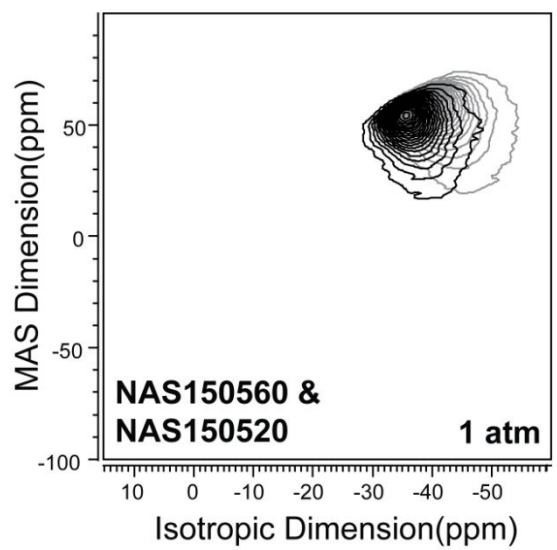


Figure 5. The overlapped ^{27}Al 2D 3QMAS spectra of Na-aluminosilicate glasses at ambient pressure

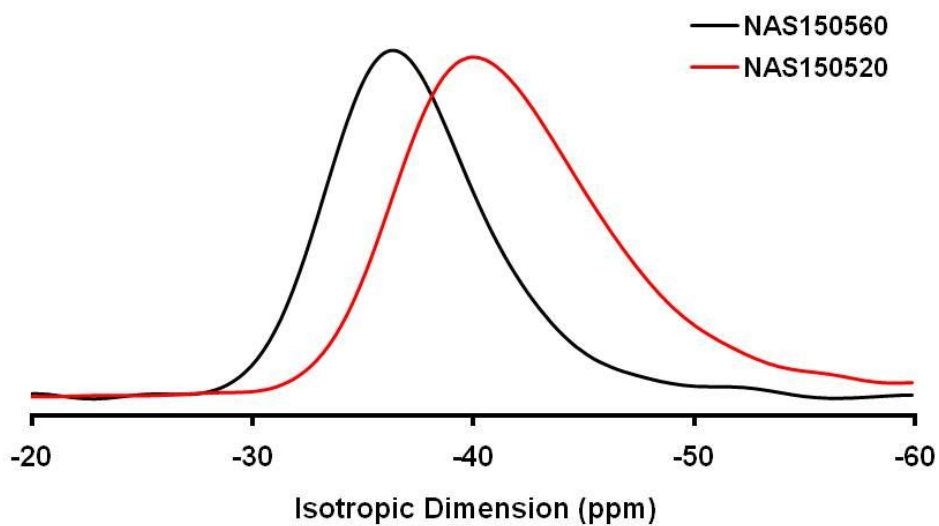


Figure 6. The isotropic projection of ^{27}Al 2D 3QMAS spectra of Na-aluminosilicate glasses at ambient pressure

Table 2. The isotropic chemical shift of ^{27}Al in Na-aluminosilicate glasses

		NAS150560			NAS150520		
Pressure		$^{[4]}\text{Al}$	$^{[5]}\text{Al}$	$^{[6]}\text{Al}$	$^{[4]}\text{Al}$	$^{[5]}\text{Al}$	$^{[6]}\text{Al}$
δ_{iso} (ppm)	1 atm	60.4±0.2			66.3±0.4		
	6 GPa	61.3±0.2	26.7±0.8	-2.2±6.7	66.6±0.2	30.8±4	
	8 GPa	62.0±0.1	27.3±0.4	-2.9±0.9	67.1±0.3	30.2±1	1.5±0.1

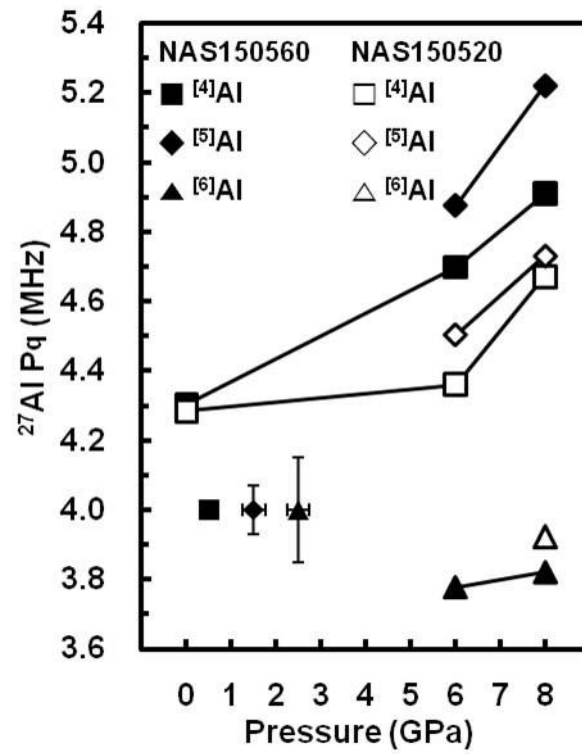


Figure 7. The quadrupolar coupling products (P_q) of ^{27}Al in Na-aluminosilicate glasses with varying pressure

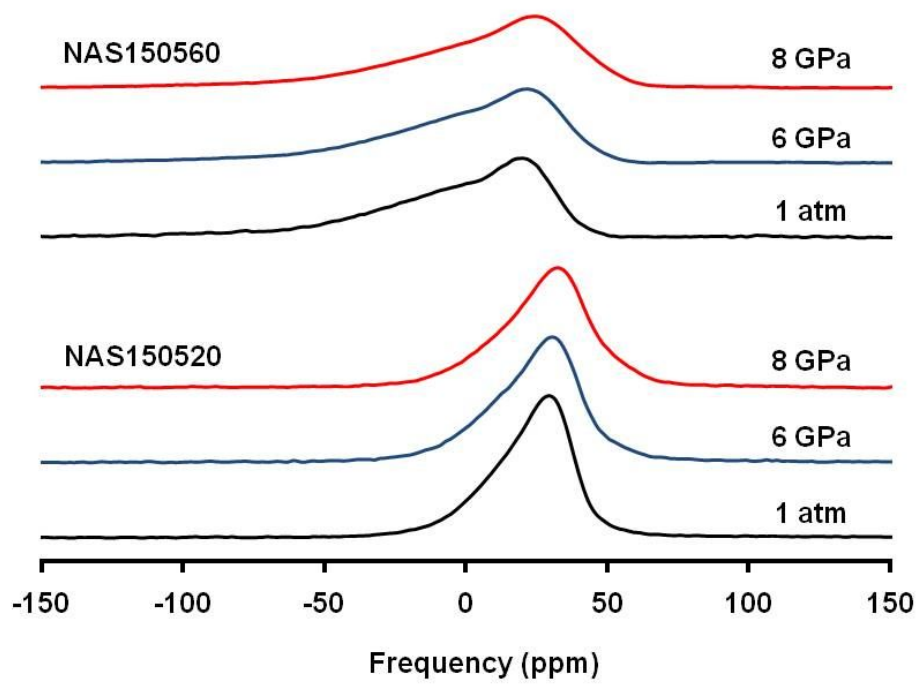


Figure 8. The ^{17}O 1D MAS spectra of Na-aluminosilicate glasses with varying pressure

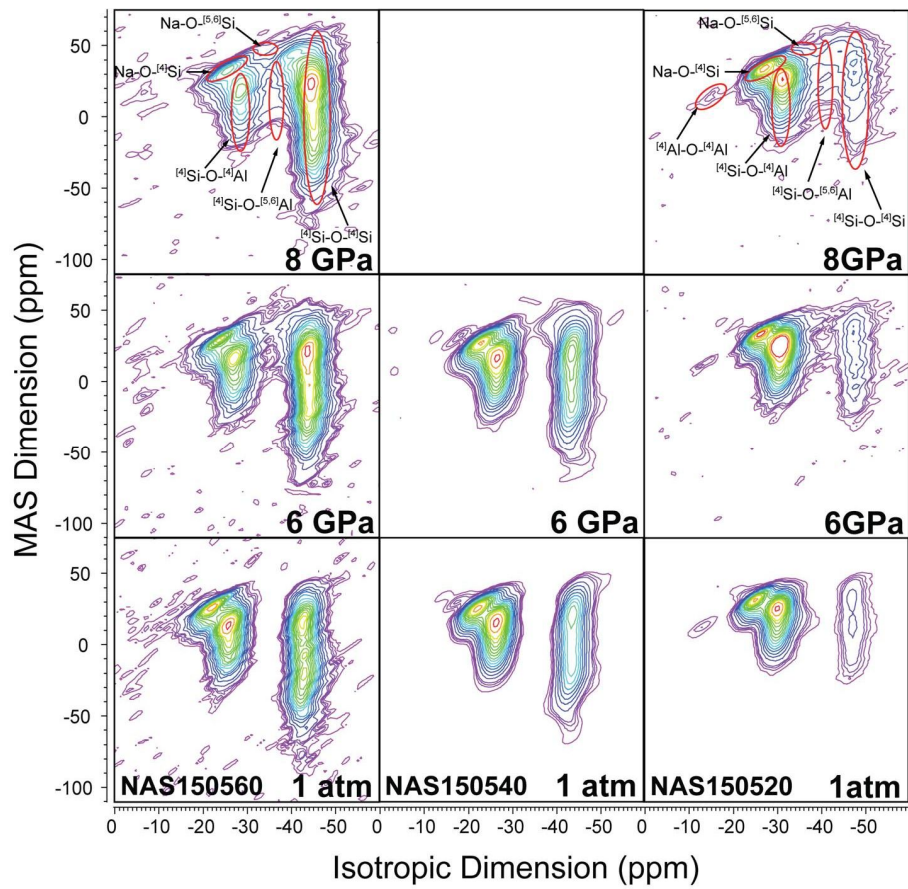


Figure 9. The ^{17}O 2D 3QMAS spectra of Na-aluminosilicate glasses with varying pressure (total 20 contour levels from 4 to 98%, added lines at 5 and 6.5%)

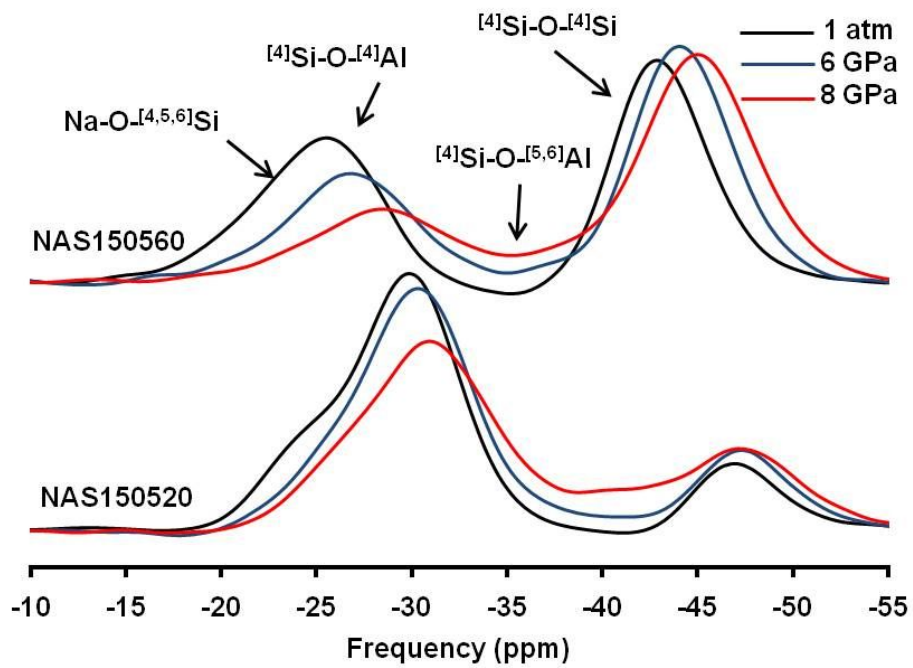


Figure 10. The isotropic projection of ^{17}O 2D 3QMAS spectra of Na-aluminosilicate glasses

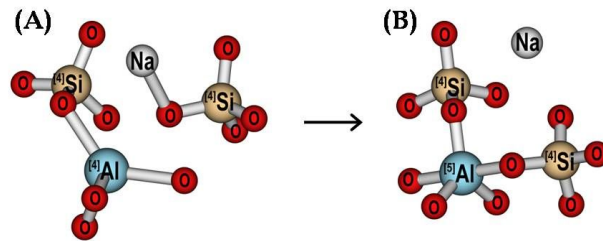


Figure 11. The schematic picture of atomic structure of polymerization process in Na-aluminosilicate glasses. (A) $^{[4]}\text{Si-O-}^{[4]}\text{Al} + \text{Na-O-}^{[4]}\text{Si}$. (B) $^{[4]}\text{Si-O-}^{[5]}\text{Al} + \text{Na}^*$

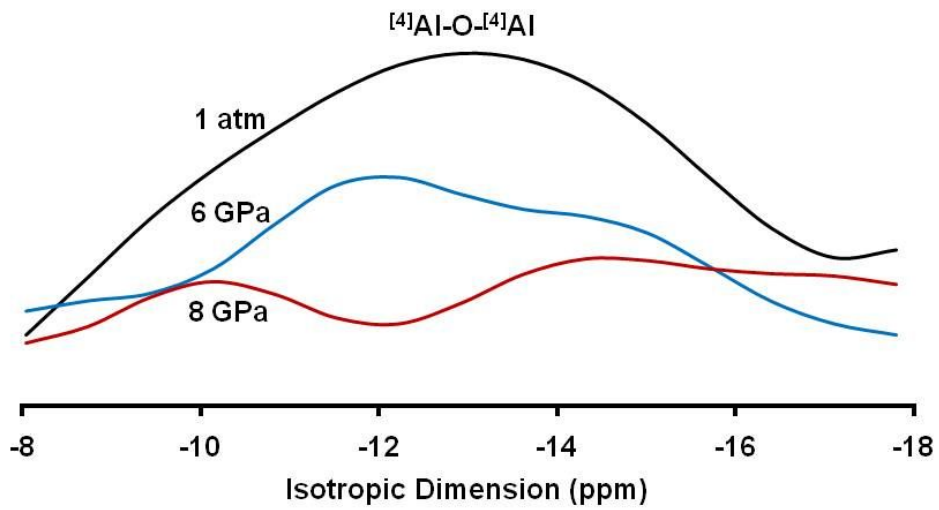


Figure 12. The proportion of $[^4\text{Al-O-}[^4\text{Al}]$ high energy cluster in NAS150520 glasses with varying pressure

Table 3. The proportion of $^{27}\text{Al-O-}^{27}\text{Al}$ in NAS150520

Pressure	Total Intensity	$^{27}\text{Al-O-}^{27}\text{Al}$	Proportion
1 atm	16091	136	0.846%
6 GPa	9481	40	0.421%
8 GPa	10058	41	0.408%

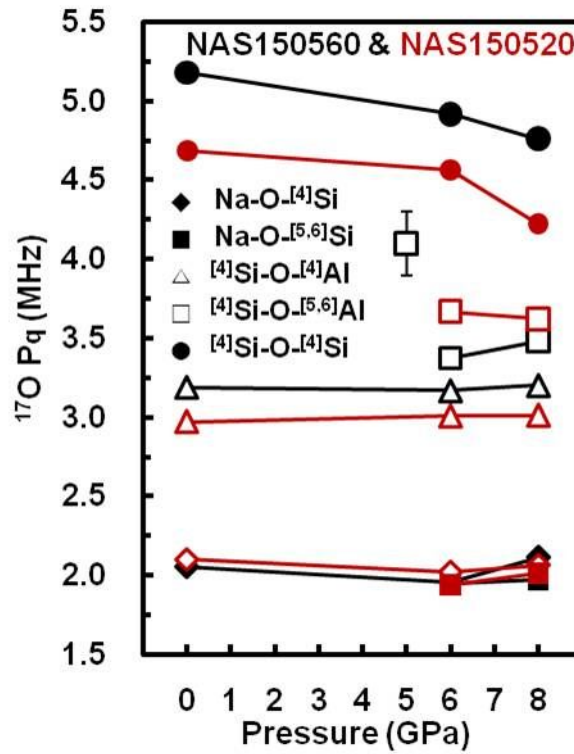


Figure 13. The quadrupolar coupling products (P_q) of ^{17}O in Na-aluminosilicate glasses with varying pressure (P_q values are estimated from its peak position except $^{4}\text{Si-O-}^{4}\text{Si}$ which is calculated from its center of gravity of peak.)

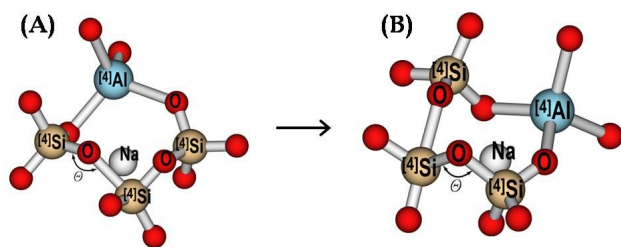


Figure 14. The schematic picture of atomic structure for decreasing $[4]\text{Si-O-[4]Si}$ bond angle

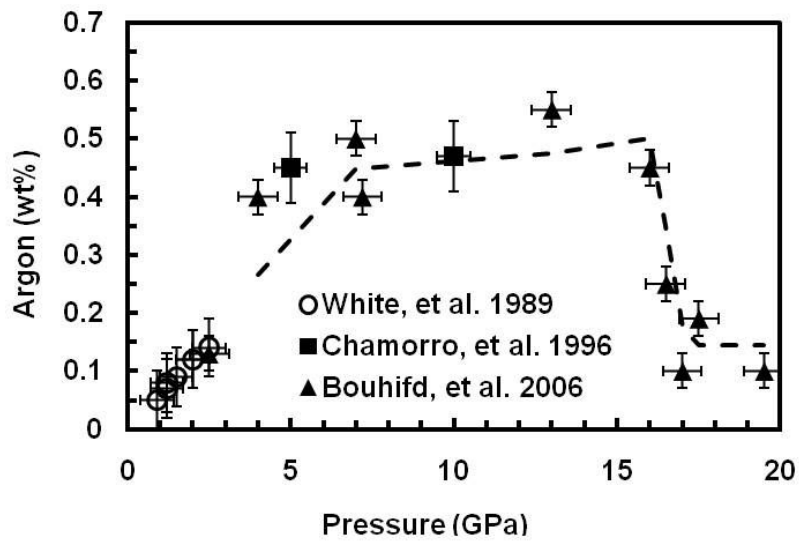


Figure 15. The pressure dependence of Ar gas solubility of Anorthite ($\text{CaAl}_2\text{Si}_2\text{O}_8$) glasses [15, 17, 18]

2. Theoretical Studies of the Local Electronic Environments of Oxygen in Mg-silicates at high pressure using ELNES (Energy-Loss Near-Edge Structure)

2.1. Introduction

Many experimentalists have been being suffered from the low possibilities and difficulties of experimental realization of high pressure and temperature condition relevant to Earth's deep inside, even though there were many recent advances of experimental apparatus and analyzing methods (i.e., diamond anvil cell, synchrotron x-ray experiments, etc.). The computational methods also called theoretical approaches, including first-principle calculations based on quantum theory, could be the solutions for overcoming the experimental difficulties to understand the material properties at extreme condition, because there are no limitations on reconstructing and controlling the surrounding environments of given system in interest [19-22]. And this theoretical approach could be used to explore the Earth's interior. Hence, we will investigate the local electronic environments of Mg-silicates with experimental and calculated results of non-resonant x-ray Raman scattering spectroscopy (XRS) in this section.

The Earth materials at high pressure, commonly silicate oxides, have not been well studied enough to understand the macroscopic

properties in amorphous and crystalline phases with high pressure in-situ XRS experiments, also in theoretical approaches, however there were many previous works done for exploring the crystalline semi-conductors and super-conducting materials. And the pressure-induced characteristic ELNES spectral features of crystalline and molten Earth materials are not well understood, too. Therefore, in this chapter, we will elucidate the pressure-induced oxygen K-edge ELNES spectral features of Mg-silicate glasses at high pressure obtained in previous work, comparing with the calculated ELNES spectra of crystalline Mg-silicates [16].

We had calculated the oxygen K-edge ELNES spectra of crystalline Mg-silicate and silicate polymorphs to use as the references of ELNES spectra of Mg-silicate glasses at high pressure: alpha-quartz, coesite, stishovite, pyroxene (ortho-enstatite), ilmenite, perovskite, and post-perovskite. And the calculated results of post-perovskite, of which the experiment is not realized due to its extremely high pressure stable field, could provide the reference of the future high pressure in-situ XRS experiments. The Mg-silicate, MgSiO_3 glasses and crystalline polymorphs, is one of the most abundant materials in Earth's mantle. The seismic explorations of Earth's interior already suggested the existence of Mg-silicate melts near the core-mantle boundary showing seismic heterogeneity. However, the atomistic origins of Mg-silicate melts and its macroscopic physical properties are still not understood well enough. Hence, we had worked on Mg-silicate glasses at high pressure with oxygen K-edge XRS spectra to investigate its local electronic structure. The

atomistic changes of Mg-silicate glasses at high pressure forming denser atomic configurations like oxygen tri-clusters could affect its thermodynamic and transport properties near the CMB. And this denser atomic configuration, also, affect the crystal-melt partitioning coefficient of lowermost mantle with reducing the permeable free volume of Mg-silicate melts.

2.2. Theoretical Backgrounds

Quantum mechanics based calculations are commonly called the ab-initio or first-principle methods. And this theoretical approach has lots of terms that should be considered in calculation, thus some of interacting terms are treated with approximation (or eliminated) for effective calculation. The conventionally used approximation methods are the DFT with pseudopotential approximation, DFT with augmented plane-wave set, and band structure formalism; from these methods, we used the DFT with augmented plane-wave set method. The common first-principle based methods represent the coefficient of electronic orbital wave-function with a matrix, and calculate the proper electron distribution (or electron configuration) using self-consistent field (SCF) method for the system in interest. We will summarize the well known approximation methods, pseudopotential approximation and APW based methods, with the flow of SCF calculation which are used in this work for calculating ELNES spectra of crystalline Mg-silicate and silicate polymorphs.

2.2.1. Principles of Non-Resonant X-ray Raman Scattering Spectroscopy

The non-resonant x-ray Raman scattering spectroscopy, also called as inelastic x-ray scattering spectroscopy, provides same information to conventional x-ray absorption spectroscopy (XAS). And this XAS measures

the x-ray absorption coefficient of incident photon (i.e., x-ray light source) including both XANES and EXAFS energy region. These two regions are distinguished from their detection energy from the absorption edge of target atom; the XANES, as its name, start ~ 5 eV from the absorption edge to ~ 50 eV, thus the absorption features of this region are induced from the multiple scattering of photoelectron excited at absorption site because of its low kinetic energy level, reflecting the chemical bonding structure and local electronic environments (i.e., sensitive in determining the average oxidation state and coordination environment of absorption site). Differently from the XANES, the wave length of backscattered photoelectron is shorter than inter-atomic distance in the EXAFS region (i.e., the higher energy region than that of XANES, from 50 eV beyond the ionization energy), thus the single scattering events become dominant and provide the local structure around absorbing site in materials and oscillation features showing the final state interference effect (i.e., The backscattered photoelectron waves interfere with the forward-propagating waves. And this interference causes the modulation of the measured absorption coefficient, causing the oscillation called the final state interference effect.).

The oxygen K-edge ELNES spectral features shows the oxygen proximity in Mg-silicate amorphous and crystalline system, and then this fact could be used in analyzing the experimental results of Mg-silicate glasses with calculated results of crystalline Mg-silicate [23-25]. We have been being tried to investigate the oxygen K-edge XRS spectral features

similar to XANES (X-ray Absorption Near-Edge Structure) region of XAS (X-ray Absorption Spectroscopy), which is also called as ELNES (Energy Loss Near-Edge Structure) spectrum, using first-principle calculations for crystalline Mg-silicate. This oxygen K-edge ELNES spectrum could provide the valuable information of atomic structure around the oxygen atom as XANES, sensitive in chemical bonding structure and local electronic environments with multiple scattering of incident photon [25]. And this multiple scattering of incident photon was used in previous theoretical approaches of ELNES spectrum, however this method lose its accuracy considering the high atomic number elements [26]. Hence, the other methodologies are used to simulate the ELNES spectral features; the density functional theory (DFT) with pseudopotential approximation, augmented plane-wave based methods, and band structure formalism, etc. [6, 27, 28]. This first-principle based theoretical approach of oxygen K-edge ELNES spectrum of MgSiO_3 and SiO_2 crystalline polymorphs would provide the advanced intuitions for analyzing the characteristic spectral features of experimental results. And we also expect that this full first-principle analysis of electronic structure of silicate oxides could shed light on the further insights of experimentally un-probed electronic origins of non-resonant x-ray Raman scattering spectral features of Earth materials at high pressure.

(i) The fundamental equations of x-ray absorption spectroscopy

The absorption coefficient (χ), which is correlated with the intensity changes of incident and transmitted x-ray, could be calculated from the dipole transition moments of electron induced by incident x-ray. The forward-propagating wave function from absorption site as a spherical wave propagates until reach neighboring atoms, and the backscattered wave induced due to this propagating wave. Then this backscattered wave interferes with forward-propagating atoms. This interference has, therefore, fine structure information near the absorption site of the system. We could investigate this fine structure using not only classical multiple scattering method but also quantum based calculation. The simple concept used in quantum based theory to calculate x-ray absorption fine structure is briefly explained. Also the fundamental EXAFS equation to give details of fine structure information is presented.

$$\mu(E) \propto |\langle f | \hat{H} | i \rangle|^2 \quad (2-1)$$

$$\hat{H} = \frac{1}{2m} \left(\vec{p} + \frac{e}{c} \vec{A} \right)^2 + V(\vec{r}) = \hat{H}_0 + \hat{H}_{int} \quad (2-2)$$

$$\hat{H}_{int} \propto \frac{e}{mc} \vec{A} \cdot \vec{p} \quad (2-3)$$

$$\hat{H}_0 = \frac{1}{2m} \vec{p}^2 + V(\vec{r}) \quad (2-4)$$

$$A_\mu = \sum_k \sum_{\alpha=1}^2 \epsilon_\mu^{(\alpha)} \left(a_{k,\alpha}(t) e^{i\vec{k} \cdot \vec{e}} + a_{k,\alpha}^\dagger(t) e^{i\vec{k} \cdot \vec{e}} \right) \quad (2-5)$$

$$\vec{B} = \nabla \times \vec{A} \quad (2-6)$$

$$|f\rangle = |f_0\rangle + |\Delta f\rangle \quad (2-7)$$

$$\mu(E) \propto \mu_0 [1 + \chi(E)] \quad (2-8)$$

$$\chi(E) \propto \langle \Delta f | \hat{H}_{int} | i \rangle \quad (2-9)$$

Here, μ indicates the transition dipole moment; A is vector potential or four vector used in classical electromagnetism or quantum field theory to formulate the Hamiltonian operator for the radiation field (i.e. products of polarization, creator and annihilating operators). The final state is separated into two parts, one is for the free electron final state and the other is for the effect of placing the atom near the absorption site (i.e. alteration due to neighboring atoms near the absorption site). This extra part of final state wave function illustrates the local fine structure around the absorption site. The details about this method are still being studied. On the other hand, the absorption coefficient could be easily calculated using multiple scattering methods considering thermal vibration of atoms and inelastic scattering effects.

$$\chi_i(\mathbf{k}) = \sum_j N_j S_i^2(\mathbf{k}) F_j(\mathbf{k}) e^{-2\delta_j^2 k^2} \cdot \exp\left\{-\frac{2r_j}{\lambda_j(\mathbf{k})}\right\} \cdot \frac{\sin(2kr_j + \phi_{ij}(\mathbf{k}))}{kr_j^2} \quad (2-10)$$

Here, the approximated spherical wave function is using a spherical Bessel function; the thermal vibration (δ_j) similar to the Debye-Waller factor (i.e., The Debye-Waller factor describes the reduction amplitude of scattered x-ray owing to a thermal vibration of atoms in condensed matter system.) is considered with Gaussian distribution; the phase shift (ϕ_{ij}) and amplitude changes (F_j) during scattering is, also,

considered; the two parameters, amplitude reduction factor (S_i) and decreasing of the signal due to inelastic mean free path (λ_j), are included.

(ii) The double diffraction scattering cross section (DDSCS)

Even the experimental XRS results provide the almost same information to XAS, the actual physical processes occurred in sample during XRS experiments are different from that of XAS. The other property, called double-diffraction scattering cross section (DDSCS), is used to describe the proper inelastic scattering process of absorption site. The DDSCS shows the excitation probability of the absorption site from initial (k_i) to final (k_f) state by absorbing kinetic energy from incident photon, and the definition of DDSCS, which is the number of scattered electrons per energy unit as a function of energy loss E , could be simplified with the dynamic form factor, $S(q,E)$.

$$\frac{\partial^2 \sigma}{\partial E \partial \Omega} = 4 \left(\frac{e_0}{q} \right)^4 m_e^2 \frac{k_f}{k_i} \cdot S(\vec{q}, E) \quad (2-11)$$

$$S(\vec{q}, E) = \sum_{kv, nlm} |\langle \vec{k}_v | e^{i \vec{q} \cdot \vec{r}} | nlm \rangle|^2 \delta(E + E_{nlm} - E_{kv}) \quad (2-12)$$

The differential electron current (σ), induced from excitation of photoelectron of absorption site, is positively correlated with the transition probability (\mathbf{W}) as follows.

$$d\sigma = \sum_{i,f} \frac{(2\pi)^3 m_e}{\hbar k_i} dW_{if} \quad (2-13)$$

$$dW_{if} = \frac{2\pi}{\hbar} |\langle f|V|i\rangle|^2 \cdot d\mathbf{v}_f \cdot \delta(\mathbf{E}_i - \mathbf{E}_f) \quad (2-14)$$

$$d\mathbf{v}_f = \frac{2m_e}{2\hbar} \mathbf{k}_f \cdot d\mathbf{E} d\Omega \quad (2-15)$$

Finally, the transition probability could be calculated from the dynamic form factor (i.e., including the crystal symmetry incident and scattered electron wave vector and transition energy difference information), and we could simulate the ELNES spectrum of absorption site in interest [29].

2.2.2. Principles of the First-Principle Calculation Methods

There are various approximation methods of first-principle calculation to calculate the inter-atomic interactions more effectively. The electron-electron interactions, major time consuming part in calculation, are approximated by treating electron distributions as density functional called DFT (density functional theory). And the minor complex part, the electron-ion (or electron-nuclei) interaction, could be simplified with pseudopotential method [6, 19, 20]. The latest and advanced approximation method for crystalline system does not approximate the electron-ion interaction using pseudopotential; this method uses the augmented plane-wave function as the basis set of electron wave function [28].

(i) Fundamentals of DFT

The Kohn-Sham energy functional approach

The many-body electron system could be represented by spatial distribution of electron gas with the exchange and correlation energy which describe the unique functional form of the given electronic system. The minimum of total energy functional provides the ground state of the system; and the electron density, which yields this energy configuration, is the exact ground state of electronic density (i.e., the singularity of the ground system). The simplified total energy functional of Kohn-Sham

approximation method, which describes the set of doubly occupied electron states (ψ_i), could be expressed with these equations. The minimum energy of this functional form provides the ground state energy of the electronic system with ions at position (\mathbf{R}_I). The total energy functional is represented with combination of various physical properties such as the Coulomb energy associated with interactions among the nuclei or ions at position (\mathbf{R}_I), the state total electron-ion potential (V_{ion}), the electron density (n), the static potential (V_{ee}) induced from the electron-electron interaction, and the exchange-correlation functional (E_{XC}).

$$E[\{\psi_i\}] = 2 \sum_i \int \psi_i \left(-\frac{\hbar^2}{2m} \right) \nabla^2 \psi_i d\tau + \int V_{ion}(\vec{r}) n(\vec{r}) d\tau + V_{ee} + E_{XC}[n(\vec{r})] + E_{ion}(\{\mathbb{R}_I\}) \quad (2-16)$$

$$n(\vec{r}) = 2 \sum_i |\psi_i(\vec{r})|^2 \quad (2-17)$$

$$V_{ee} = \frac{e^2}{2} \int \frac{n(\vec{r})n(\vec{r}')}{|\vec{r}-\vec{r}'|} d\tau d\tau' \quad (2-18)$$

BO and CP approximation methods

The Born-Oppenheimer (BO) method, which is an approximation method used in computational quantum chemistry to explore the energy and wave function of the molecule. In this approximation method, the wave function of a molecule is separated into two parts, its electronic term and nuclear term because the nuclear mass is heavier than electron about 1,000 times. Then the energy of electron is treated as not correlated with nuclear motion that means the electron moves in another frame fixed at nuclear. However, the another approximation method, Car-Parrinello (CP),

is natural density functional theory based approximation using local density approximation (LDA) and pseudo potential method. This CP method has higher accuracy than BO method which is the limiting case of CP method.

The exchange and correlation energy

The exchange energy is induced from the reduced Coulomb energy of the electron because of the anti-symmetric property of electron wave function (i.e., the electron has half-integer spin number known as fermion). And this effective pseudo energy makes spatial separation of electron and reduces the Coulomb energy. The origin of correlation energy is the difference between the many-body interaction and the energy of system could be calculated with the Hartree-Fock (HF) approximation method.

Pseudopotential approximation (electron-ion interaction)

In the core region, the wave functions of the electrons oscillate rapidly because of the tightly bound core orbital and this strong ionic potential could be replaced with pseudo potential function which is identical at outside the core region. Also the rapidly oscillated wave function is replaced with pseudo wave function that needs relatively small number of basis function than the real wave function because each wave and potential function is designated having no radial node inside the core region. Furthermore, these rapidly oscillated wave and potential functions

are correspond with orthogonality between the wave function of valence electron and core electron. Each discrete energy state of valence electron augments, increasing its number, near the core region because of the strong ionic potential of nuclei. Therefore, defining the adequate pseudo potential function decreases the enormous number of plane-wave basis state which is induced from region of rapidly oscillated function near the core.

(ii) Fundamentals of APW based methods

The APW, LAPW, and DFT

The theoretical approaching method used in this work is specialized for calculating electronic properties of the crystalline system which has long range periodicity. The plane wave (PW) is a common basis set for calculating the DFT equations for the electron wave functions in crystalline system. The PWs are, however, inefficient basis set for describing the rapidly oscillating wave functions near the core region of the atomic system. Therefore there have been being developed many approximation methods to avoid this inefficient natural basis set of electron wave function. The first one is pseudopotential approximation method which replaces the original potential function with simplified potential function. The other method is called augmented plane wave based methods used in this work [29-35].

Augmented plane-wave (APW) basis set

In the APW method, the wave functions in a crystal system are expressed in terms of spherical harmonics and radial functions around of each atom, and of plane waves between the atoms. In the LAPW method, the energy dependence of each radial wave function (used as basis function of wave function) in the atomic sphere region is linearized by taking a linear combination of energy value and its energy derivative which is computed at the same energy. The unit cell is partitioned into two regions, the first one (I) is the sphere centered on the all constituent atomic site position (r) with its radius (R), and then second region (II) is remaining interstitial region. The wave functions are expanded into plane waves (PWs), each of what is augmented by atomic solutions in the form of partial waves (i.e. the product of a radial function and spherical harmonics). The Kohn-Sham orbital (ψ_i) is expressed as a linear combination of APWs basis function (ϕ_k). The KS orbital is extended to non-linear eigenvalue problem by choosing inadequate value of initial energy of the system. In a consequence, the initial trial value of energy for SCF calculation should be selected from calculation results of solving the energy secular equation ($|H-ES|=0$).

$$\psi_k = \sum_n C_n \phi_{k_n} \quad (2-19)$$

$$\phi_K(r) = \begin{cases} \sum_L \alpha_L^{\alpha K} u_L^\alpha(r', \epsilon) Y_L(r'), & r' < R_\alpha \\ \Omega^{-\frac{1}{2}} \exp[i \cdot (k + K) \cdot r], & r \in I \end{cases} \quad (2-20)$$

Full potential + Linearized augmented plane-wave (LAPW) basis set

In this method, the spatial energy dependence of each radial wave function in the atomic sphere region is linearized with taking a linear combination not only the energy at fixed position but also its position derivative. The solutions of the KS equation are expanded according to the variational method which allows us to approximate the ground state energy of a system using trial variation function made from LAPW basis function without solving Schrödinger equation. The various properties of electronic system like crystal potential, charge density, and forces acting on the atoms could be calculated relatively efficiently than using APW method only, because the efficient optimization of structural parameters is possible by taking spatial energy dependence on each radial wave function.

$$\phi_K(\mathbf{r}) = \begin{cases} \sum_L [a_L^{\alpha K} u_L^\alpha(\mathbf{r}') + b_L^{\alpha K} \dot{u}_L^\alpha(\mathbf{r}')] Y_L(\hat{\mathbf{r}}'), & r' < R_\alpha \\ \Omega^{-\frac{1}{2}} \cdot \exp[i(\mathbf{k} + \mathbf{K}) \cdot \mathbf{r}], & r \in I \end{cases} \quad (2-21)$$

$$\frac{\langle \phi^* | \hat{H} | \phi \rangle}{\langle \phi^* | \phi \rangle} \geq E_1 \quad (2-22)$$

Augmented plane-wave + Local orbital (LAPW+lo) basis set

The theoretical method used in this work separates the energy state of electron into three types; core, semi-core, and valence state. In the core state, the charge is entirely confined inside the corresponding atomic sphere. And the energetically highest occupied state, valence state, always has a significant amount of charge outside the atomic sphere. The intermediate energy state, semi-core state, is high enough energy and in this regime charge is no longer completely confined inside the atomic

sphere but has few percents outside the atomic sphere. This semi-core state is not easy to describe using APW method or LAPW because of a definite spatial separation of atomic sphere region in wave function. Therefore, the concept of local orbital introduced to approximate the semi-core energy state more efficiently. The basis set of APW+lo method is analogous to that of original APW method. However the local orbital term is added with the continuity condition at the atomic sphere boundary and makes the faster convergence than LAPW method.

$$\phi_{lo}(\mathbf{r}) = \begin{cases} [a_L^{\alpha,lo} \mathbf{u}_l^\alpha(\mathbf{r}') + b_L^{\alpha,lo} \dot{\mathbf{u}}_l^\alpha(\mathbf{r}')] Y_L(\hat{\mathbf{r}}'), & r' < R_\alpha \\ \mathbf{0}, & \mathbf{r} \in I \end{cases} \quad (2-23)$$

2.3. Results and Discussions

2.3.1. Experiments and Calculations

Experiments

All of the experimental oxygen K-edge XRS results used here were obtained in previous work of 'X-ray Raman scattering of MgSiO₃ glass at high pressure' [16]. The details of sample synthesis methods and experimental conditions are summarized in that paper. They used Mg-silicate oxide materials in both amorphous and crystalline phases to explore the local electronic environment of MgSiO₃ glass at high pressure with in-situ experiments. And this oxygen K-edge ELNES spectra of MgSiO₃ glass at high pressure were compared with that of crystalline MgSiO₃ and SiO₂ polymorphs to distinguish characteristic spectral features of MgSiO₃ glass at high pressure. The used crystalline SiO₂ sample was alpha-quartz, and MgSiO₃ samples were pyroxene (ortho-enstatite), ilmenite, and perovskite.

Calculations

We had used the LAPW based program package called Wien2k to calculate the oxygen K-edge ELNES spectra of crystalline SiO₂ and MgSiO₃ polymorphs [36]. The selected crystalline SiO₂ polymorphs were alpha-quartz, coesite, stishovite; and MgSiO₃ polymorphs were pyroxene, ilmenite, perovskite, and post perovskite. The atomic structures of these crystals were referred from previous XRD experimental results listed in

Table 4. And the Figure 16 shows the atomic structures of calculated SiO₂ and MgSiO₃ crystals, the structure optimization for given structure did not perform in the whole calculation. The crystal structures are visualized and edited using Visualization for Electronic and STructural Analysis (VESTA) program [37]. The oxygen K-edge ELNES spectra and partial density of states (p-DOS) were calculated for those selected crystalline Earth materials.

The proper electronic configuration (i.e., optimized electronic orbital distribution) should be calculated as a preparatory step to calculate the oxygen p-DOS and oxygen K-edge ELNES spectra of crystalline SiO₂ and MgSiO₃ polymorphs. And the SCF calculation should be used in this process. The appropriate parameters for SCF cycle are chosen as follows. The Muffin-Tin radii (R_{MT}) for Mg, Si, and O determined by program were 1.79, 1.59, and 1.59 Å, whereas the real atomic radii of atoms are 1.6, 1.18, and 0.78 Å. The cut off energy of separation of core and valence state is chosen to -7.1 Ry for more accurate calculation, because the default value (-6.0 Ry) makes the p-orbital of silicon treated as core electron. And the Perdew-Burke-Ernzerhof 96 (i.e., PBE-96, one of the common generalized gradient approximation methods) is chosen as exchange-correlation approximation method. The RK_{MAX} , which limits the number of coefficient of electron wave function for atoms with R_{MT} , was set to 5.0. Conventionally, this value is set to 2.3~ for hydrogen atom, 5.0~ for s- and p- orbital elements, and 6.0~ for f-orbital elements (O - 1s² 2s² 2p⁴, Si - [Ne] 3s² 3p², Mg - [Ne] 3s²). The G_{MAX} value, which determines the magnitude of largest vector in Fourier expansion of charge density, is set to 12.0.

Conventional G_{MAX} value for GGA method is 14.0, however the relatively smaller value is sufficient to calculate proper electronic configuration in simple atomic system (i.e., merely s- and p-orbital in valence states). The number of k-point is set 30~50 with considering each cell size of SiO_2 and MgSiO_3 polymorph. The 100~1,000 k-points for 1 atom/cell is sufficient to calculate insulators such as silicate oxides, and the size of k-mesh generated from the number of k-point could be reduced with increasing the number of atoms in unit cell by a factor N (i.e., N atoms/cell). The convergence criteria of SCF calculation were total energy and charge fluctuation; energy as 0.0001 Ry and charge as 0.0001 e.

The oxygen K-edge ELNES spectra are calculated with relevant program module. Some parameters should be chosen to calculate proper spectra. The absorption edge of oxygen is set to 538.25 eV (i.e., the electron binding energy of 1s orbital) and energy grid is set to 0-35 eV. The detector collection semi-angle and microscope convergence semi-angle are 5.0 and 1.87 mrad as default values, and the dipole approximation mode is selected for a detector angle independent calculation. The edge offset of valence broadening is set above the end of energy grid and the Gaussian broadening factors of spectrometer are 0.0, 0.5, and 1.5. The Gaussian broadening factor, induced from an instrumental broadening, is selected to represent the most relevant ELNES spectrum to experimental results. After this ELNES calculations, the p-DOSs of oxygen were calculated to analyze the XRS spectral features more specifically. The XAS and XRS spectral features are induced from the relevant occupied orbitals; thus the

calculated p-DOS could reflect the characteristic XRS spectral features. The calculated density of states were total DOS, and p-DOS of s- and p-orbital including directional dependence of p-orbital for oxygen. The Gaussian broadening factors for p-DOS calculations were 0.0, 0.003, and 0.04. Furthermore, the electronic excitation of 1s-orbital in oxygen atom, called the core-hole effect, is considered for non-resonant x-ray Raman scattering and DOS calculation. Hence, the electronic configuration of target oxygen is modified in an appropriate way (i.e., the single core electron in 1s-orbital is removed and the additional electronic charge is added in valence shell.).

2.3.2. Results

Experiments (the oxygen K-edge XRS spectroscopy)

The oxygen K-edge XRS spectra were collected in APS and SPring-8 for alpha-quartz and MgSiO₃ crystalline polymorphs. All of the experimental results of selected crystals are listed in Figure 17 with relevant calculated oxygen K-edge ELNES spectra. The result of alpha-quartz shows the characteristic spectral features as following; the intense peak around 538 eV, small bump at ≈545 eV, and broad peak beyond ≈550 eV. The result of ilmenite shows the distinct spectral features from other MgSiO₃ polymorphs; the well separated two peak maxima are appeared in ≈535~545 eV regions with broad peak beyond ≈550 eV. The spectrum of pyroxene could not provide clear spectral features as that of ilmenite; the broad peak with small intensity fluctuation at ≈530~540 eV, small bump

near 547 eV, and broad peak beyond 550 eV. The spectrum of perovskite shows the intense and broad peak $\approx 535\sim 545$ eV with peak like small feature ≈ 547 eV, and broad peak beyond 550 eV. However, it is difficult to conclude that the small features ≈ 547 eV as peak because the signal-to-noise ratio of this spectrum is not good enough to distinguish such small features. The spectra of MgSiO_3 glasses with varying pressure from ambient pressure to ≈ 39 GPa show the significant peak shifting and little broadening.

Calculations

All of the calculated oxygen K-edge ELNES spectra and p-DOS are compared with the experimental XRS results. These two calculated results could predict the XRS experimental results with further insights for analyzing local electronic environments of sample. The chosen crystalline SiO_2 polymorphs are alpha-quartz, coesite, and stishovite; and the MgSiO_3 polymorphs are pyroxene, ilmenite, perovskite, and post-perovskite. The calculated results are summarized in this section.

Alpha-quartz and coesite. The calculated oxygen K-edge ELNES spectrum of alpha-quartz shows the consistent results with experimental results. The ELNES calculation reproduces the broad peak ≈ 540 eV and small bump ≈ 545 eV regions. The p-DOS of oxygen shows that the broad and intense peak of ELNES spectrum is mainly originated from p-orbital excitation of oxygen and the part of broad peak beyond 550 eV is arisen from d-orbital

of oxygen [Figure 18]. The alpha-quartz is constructed by tetrahedral SiO_4 units with corner-sharing oxygen, and this characteristic structure induces the spectral shape of calculated oxygen K-edge ELNES spectrum. The similar spectral features are arisen in coesite which is constructed by SiO_4 with corner-sharing oxygen having different arrangement [Figure 19].

Stishovite. Not only the coesite but also higher pressure stable phase stishovite is calculated as other SiO_2 polymorphs, and the calculated ELNES spectrum and p-DOS show the distinct spectral features because the stishovite is constructed with octahedral SiO_6 units with edge-sharing oxygen [Figure 20]. The two intense and broad peaks are observed at ≈ 537 and ≈ 542 eV regions with broad peak beyond 550 eV, and this calculated result shows good agreement with previous experimental and calculated results [24]. The calculated oxygen p-DOS of stishovite provides the detailed electronic origins of calculated ELNES spectrum; the each directional component of p-orbital (i.e., PX, PY, and PZ) reflects the lattice arrangements of SiO_6 unit. Thus, the p-DOS of stishovite shows different features from that of alpha-quartz and coesite, which have relatively randomly oriented frame units than stishovite. These distinct spectral features of stishovite might be originated from its edge-sharing oxygen configuration, indicating closer oxygen proximity to its second nearest neighboring oxygen [16, 24, 38]. And these calculated results of SiO_2 polymorphs would be helpful to elucidate the ELNES spectra of MgSiO_3 polymorphs.

Pyroxene. We calculated the oxygen K-edge ELNES spectra and p-DOS for crystalline MgSiO_3 polymorphs same as the case of SiO_2 polymorphs. The calculated pyroxene was ortho-enstatite, and this structure has distinct crystal site; epical site, and corner-sharing and not-connected oxygen at planar site. Hence, each of sites is calculated and averaged with its proportion to compare with experimental results, while the experimental result of pyroxene shows similar spectral features to alpha-quartz originated from its SiO_4 tetrahedral unit connected with corner-sharing oxygen. The intense peak of pyroxene is appeared at ≈ 540 eV with broader peak width than that of alpha-quartz [Figure 21], indicating the larger bond angle of Si-O-Si stemmed from the cation effect of Mg and its atomic configuration [16]. The result of each crystallographic site of pyroxene provides the distinct spectral features; the corner-sharing oxygen site shows the well known alpha-quartz like spectral features, and other components show distinct spectral features.

Ilmenite. The oxygen K-edge XRS spectrum of ilmenite shows peculiar spectral features differently from pyroxene, with two peak maxima $\approx 535\sim 545$ eV and broad peak beyond 550 eV. And the calculated ELNES spectrum of ilmenite shows consistent result with experimental result [Figure 22]. These two peak maxima in main peak at ≈ 540 eV might be originated from the edge-sharing oxygen of SiO_6 octahedral as stishovite. And the p-DOS of each directional component in p-orbital shows the distinct shape due to their horizontal alignment of octahedral sites.

Perovskite. The experimental result of perovskite could not provide clear spectral features as stishovite or ilmenite. The calculated oxygen K-edge ELNES spectrum of perovskite is similar to experimental results even the resolution of spectrum is not enough to distinguish detailed spectral features due to its low signal-to-noise ratio; the intense and broad peak appears at $\approx 535\sim 545$ eV and broad peak beyond 550 eV [Figure 23]. And the small peak like feature appears at ≈ 552 eV in experimental results (i.e., even it is difficult to conclude this feature is signal due to the low signal-to-noise ratio) in both experimental and calculated results. The results of p-DOS show that the oxygen K-edge ELNES spectrum of perovskite is also mainly come from the oxygen p-orbital excitation. These calculated results of perovskite do not show the distinct spectral features $\approx 535\sim 545$ eV like stishovite or ilmenite because all of the SiO_6 octahedral sites of perovskite are connected with corner-sharing oxygen.

Post-perovskite. The ELNES spectrum and p-DOS of the higher pressure stable phase than perovskite, post-perovskite, are calculated to distinguish the changes of spectral features during the Pv-pPv phase transition [Figure 24]. The well aligned octahedral SiO_6 units of post-perovskite are connected with both corner-sharing and edge-sharing oxygen, and each calculated result of distinct crystallographic site shows different spectral features each other. The absorption edge of oxygen in post-perovskite is shifted to higher energy than that of perovskite with a small peak width broadening.

2.3.3. Discussion

Nowadays, the non-resonant x-ray Raman scattering spectroscopy is one of the most effective structural probes for exploring the local electronic structure of both crystalline and amorphous materials at extremely high pressure and temperature, although there are still remaining problems to distinguish the system having similar spectral features with local electronic environments. However, this problem could be solved by collecting spectra with changing target elements, and using first-principle calculations to analyze the atomistic origins of spectral features. Hence, in this work, the oxygen K-edge ELNES spectra of crystalline SiO_2 and MgSiO_3 polymorphs were calculated using LAPW based method to analyze the oxygen K-edge XRS experimental results of MgSiO_3 glasses at high pressure. And the calculated results of crystalline system show the characteristic spectral feature for corner-sharing and edge-sharing oxygen, having different oxygen proximity to its second nearest neighboring oxygen.

In the SiO_2 polymorph system, the differences between corner-sharing oxygen of SiO_4 tetrahedral site and edge-sharing oxygen of SiO_6 octahedral site are clearly observed with broader absorption threshold expanded to higher energy region. However, the MgSiO_3 polymorphs show different results because of the network modifying cation in the system. The ilmenite, which has edge-sharing oxygen with octahedral sites, shows similar spectral features to that of stishovite with more overlapped

two main peaks. And the perovskite, which is constructed with corner-sharing oxygen of SiO_6 octahedral sites, shows different spectrum to ilmenite of which the connection way of oxygen is edge-sharing. The post-perovskite, higher pressure stable phase of perovskite, shows the distinct calculated ELNES spectrum to that of perovskite with increasing absorption edge and peak maximum because of rearrangement of SiO_6 units at high pressure. All of these experimental and related calculation results of oxygen K-edge ELNES spectra show that the connections of oxygen, corner-sharing and edge-sharing of frame units, is reflected in corresponding ELNES spectra.

The Figure 25 shows the oxygen K-edge XRS spectra of MgSiO_3 glasses with varying pressure from 1 atm to 39 GPa with significant pressure dependence of spectral features, and the calculated ELNES spectra of perovskite and post-perovskite are also listed showing shifted absorption edge and peak maximum to higher energy region about 5 eV showing similar trend of changing spectrum to that of MgSiO_3 glasses at high pressure [16]. The previous NMR experiments for MgSiO_3 glasses at high pressure show the increasing proportion of highly coordinated Si with increasing pressure [39]. The oxygen K-edge ELNES spectra, which reflect the local electronic bonding structure of oxygen, of perovskite and post-perovskite provide the similar trend and a magnitude of changes of spectral feature (≈ 5 eV) to that of MgSiO_3 glasses at high pressure, where the differences of spectral features between perovskite and post-perovskite are induced from closer oxygen proximity in post-perovskite with

rearrangement of SiO_6 octahedral units (i.e., particularly, a corner-sharing oxygen, $^{\text{[6]}\text{Si-O-}^{\text{[6]}\text{Si}}$, in perovskite leads to a oxygen K-edge features around 540 eV while a edge-sharing oxygen, $^{\text{[6]}\text{Si-O-2}^{\text{[6]}\text{Si}}$, in post-perovskite results in features around 545 eV.). Since, the edge-sharing oxygen of SiO_6 octahedral sites in MgSiO_3 post-perovskite has similar atomic configuration to that of oxygen tri-clusters (i.e., oxygen coordinated by three highly coordinated Si atoms) indicating the closer oxygen proximity to next nearest neighboring oxygen than that of corner-sharing oxygen, these current results could imply that the previous assignment of the ≈ 545 eV features as oxygen tri-clusters in Mg-silicate glass at high pressure about 20 GPa is likely to be correct. This structural change of MgSiO_3 glasses at high pressure, also, could affect to the changes of intermediate atomic configuration not only local electronic bonding structures [16].

3. Conclusion

The presented results of solid-state NMR experiments and first-principle calculations of silicates provide the local atomic structure and electronic environments around the target nucleus. The NMR experiments of Na-aluminosilicate glasses provide the effect of network modifying cation on structural changes of sample glasses synthesized at high pressure as a precursor of the silicate melts in Earth's interior above 400 km (~15 GPa). And the non-resonant x-ray Raman scattering experiments for oxygen K-edge of MgSiO₃ glasses at high pressure and relevant calculated ELNES spectra of MgSiO₃ crystalline polymorphs show the pressure effect on local electronic environments of oxygen in MgSiO₃ glasses at high pressure as a precursor of upper mantle above 1000 km (~40 GPa), and used for predicting the atomic configuration of MgSiO₃ melts at higher pressure near the core-mantle boundary condition. These local atomic structure and electronic environments could provide the advanced understanding of transport properties of silicate melts at high pressure and their essential roles on evolution of Earth's system. Because, the dynamic of fluid in Earth's interior, mantle convection, is one of the most important factors causing the evolution of stratified layers and heat transport of Earth's interior [40]. The changes of transport properties caused from the pressure-induced atomic structural changes and its compositional effects are as follows. The diverse evidences of strong correlation between the viscosity and atomic configuration have been being studied in many

previous works. They suggested that the pressure-induced structural changes cause a polymerization of silicate melts, increasing proportions of bridging oxygen and increasing viscosity of which is correlated with the activation barrier of atomic mobility [41, 42].

These presented results could provide the valuable information about not only transport properties but also chemical properties such as elements partitioning and inert gas solubility, and so on. The inert gas solubility which could be one of the structural probes of silicate melts at high pressure and is a primary key of solving the origins of atmosphere of terrestrial planet for exploring the processes of inert gas elements sequestration in Earth's interior with stratified layer during cooling of the magma ocean [14, 17, 43]. The recent experimental results show the anomalous Ar gas solubility versus pressure as Figure 15, incompatible with common sense of the gas solubility of liquid which should increase with increasing pressure because the inert gas elements near the surface boundary move to melts to equilibrate the chemical potential [14, 15, 17, 18]. This anomalous feature of Ar gas solubility at high pressure might be originated from atomic configuration of silicate melts distinguished from its chemical equilibration because the significant atomic structural changes of silicate melts occurred at high pressure change the permeable free volume of Ar gas molecule in silicate melts. And the rapid drop of Ar gas solubility would be caused from the breakdown of silicate melts structure with forming oxygen tri-cluster like configuration. Furthermore, this structural change of silicate melts also could affect to the elements

partitioning between melts and crystal in mantle similar to the case of inert gas solubility with varying the proportion of bridging oxygen [16, 44].

Table 4. The crystallographic information of SiO₂ and MgSiO₃ polymorphs

Crystal	Composition	Lattice Parameter						
		Space Group	a (Å)	b (Å)	c (Å)	α	β	γ
<i>a</i> -quartz ⁽¹⁾	SiO ₂	(152) P3121	4.921	4.921	5.404	90	90	120
Coesite ⁽²⁾	SiO ₂	(15) C2/c	7.136	12.369	7.174	90	120.34	90
Stishovite ⁽³⁾	SiO ₂	(136) P42/mnm	4.18	4.18	2.668	90	90	90
Ilmenite ⁽⁴⁾	MgSiO ₃	(148) R -3	4.728	4.728	13.559	90	90	120
Ortho-enstatite ⁽⁵⁾	MgSiO ₃	(61) Pbcn	18.225	8.813	5.18	90	90	90
Perovskite ⁽⁶⁾	MgSiO ₃	(62) Pbnm	4.775	4.929	8.897	90	90	90
Post-perovskite ⁽⁷⁾	MgSiO ₃	(63) Cmcm	2.456	8.042	6.093	90	90	90

(1) 2x2x1 super cell (36 atoms), Glinneman et al., Z Kristallogr, 1992 [45]

(2) 2x1x1 super cell (56 atoms), Levien et al., Am. Mineralogist, 1981 [46]

(3) 2x2x1 super cell (48 atoms), Ross et al., Am. Mineralogist, 1983 [47]

(4) 2x1x1 super cell (60 atoms), Horiuchi et al., Am. Mineralogist, 1987 [48]

(5) 1x1x1 single cell (80 atoms), Ohashi, Phys. Chem. Minerals, 1984 [49]

(6) 2x2x1 super cell (80 atoms), Horiuchi et al., Am. Mineralogist, 1987 [48]

(7) 1x1x1 single cell (80 atoms), Murakami et al., Science, Vol. 304, p. 855, 2004 [50]

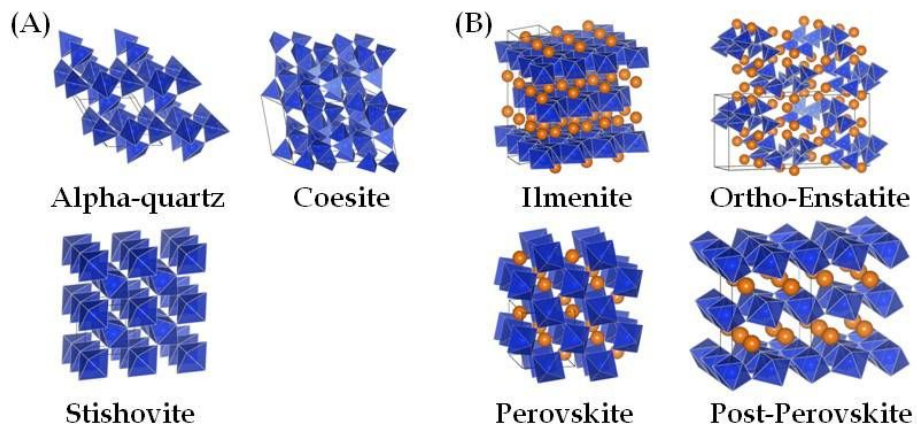


Figure 16. The crystal structures of SiO_2 and MgSiO_3 polymorphs. (A) the crystalline SiO_2 polymorphs; alpha-quartz, coesite, stishovite. (B) the crystalline MgSiO_3 polymorphs; ilmenite, ortho-enstatite (pyroxene), perovskite, post-perovskite

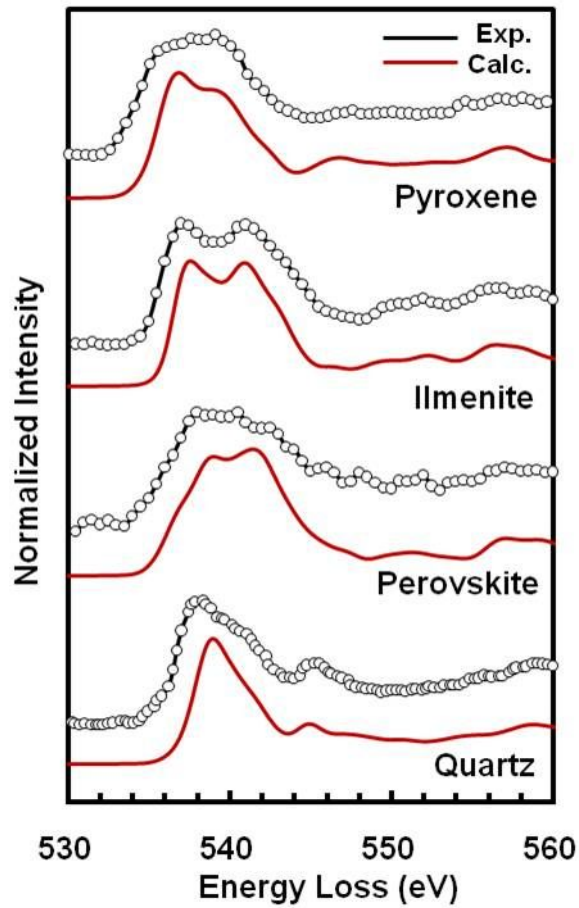


Figure 17. The oxygen K-edge experimental XRS and calculated ELNES spectra of alpha-quartz and crystalline MgSiO₃ polymorphs

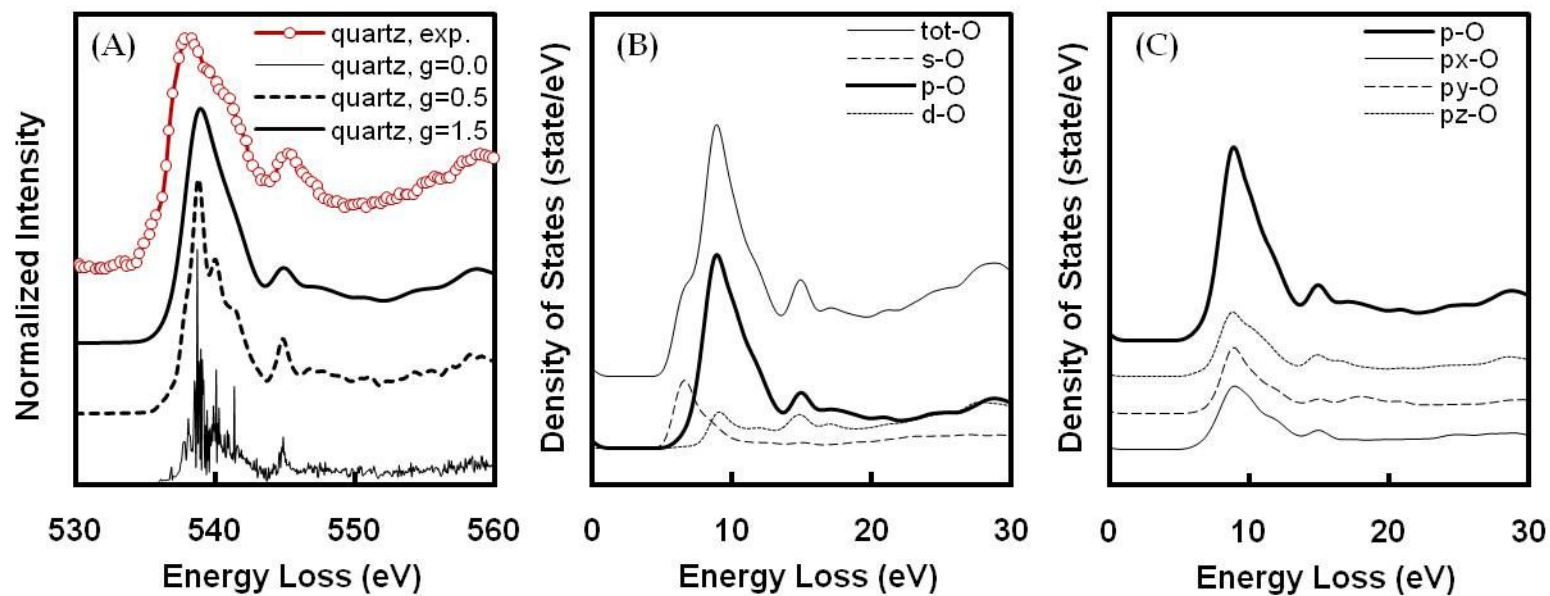


Figure 18. The calculated and experimental results of SiO₂ alpha-quartz. (A) the oxygen K-edge ELNES spectra. (B) the partial density of states (p-DOS) of oxygen. (C) the directional components in p-orbital of oxygen.

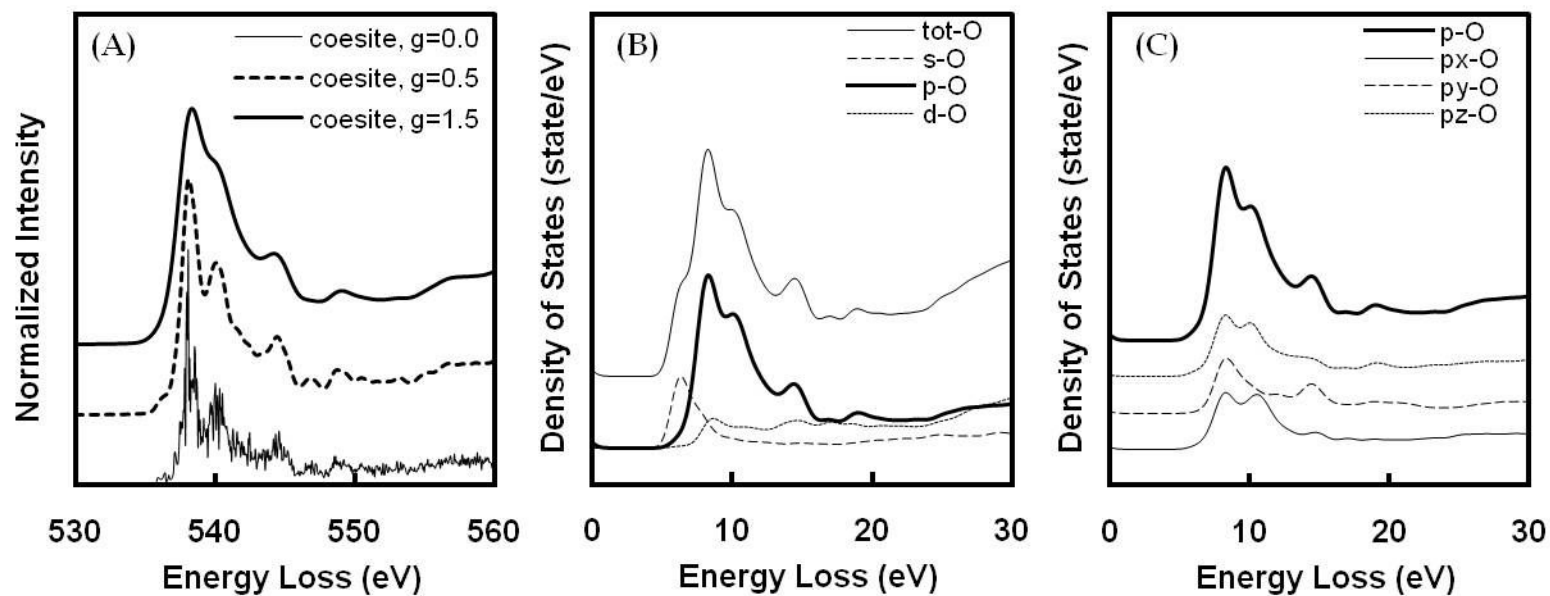


Figure 19. The calculated results of SiO₂ coesite. (A) the oxygen K-edge ELNES spectra. (B) the partial density of states of oxygen. (C) the directional components in p-orbital of oxygen.

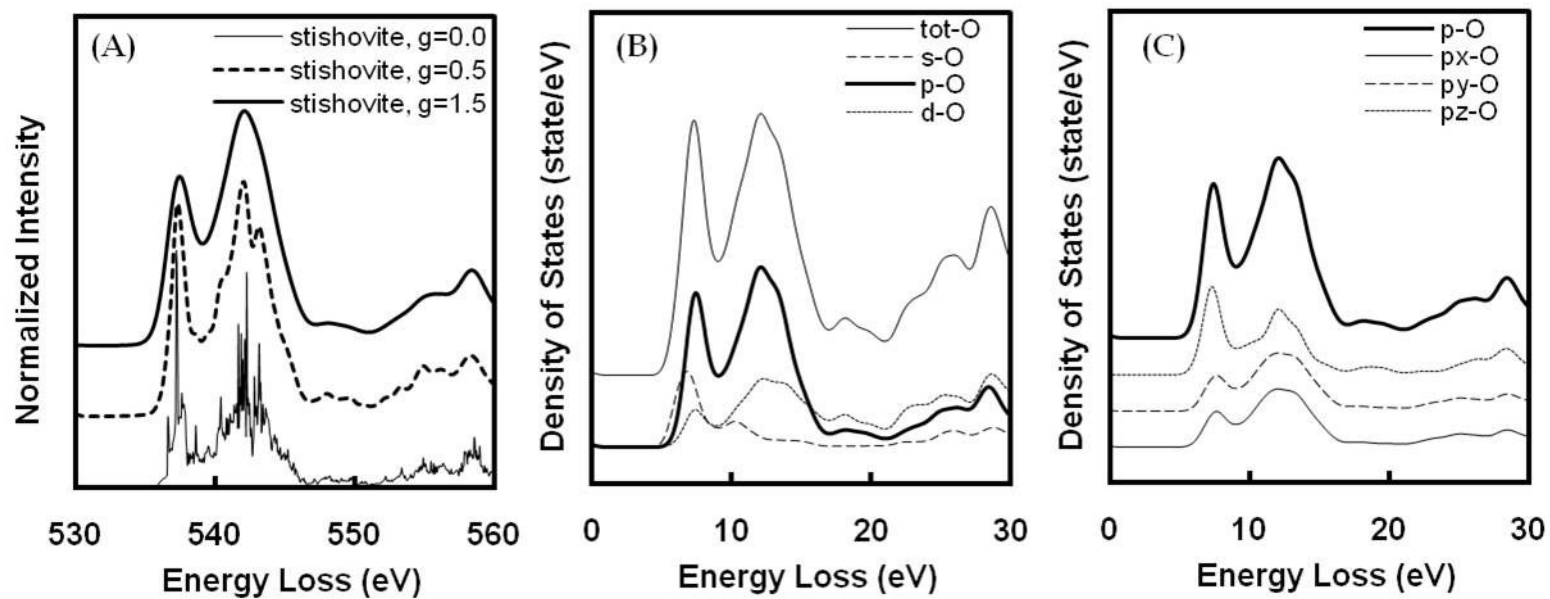


Figure 20. The calculated results of SiO₂ stishovite. (A) the oxygen K-edge ELNES spectra. (B) the partial density of states of oxygen. (C) the directional components in p-orbital of oxygen.

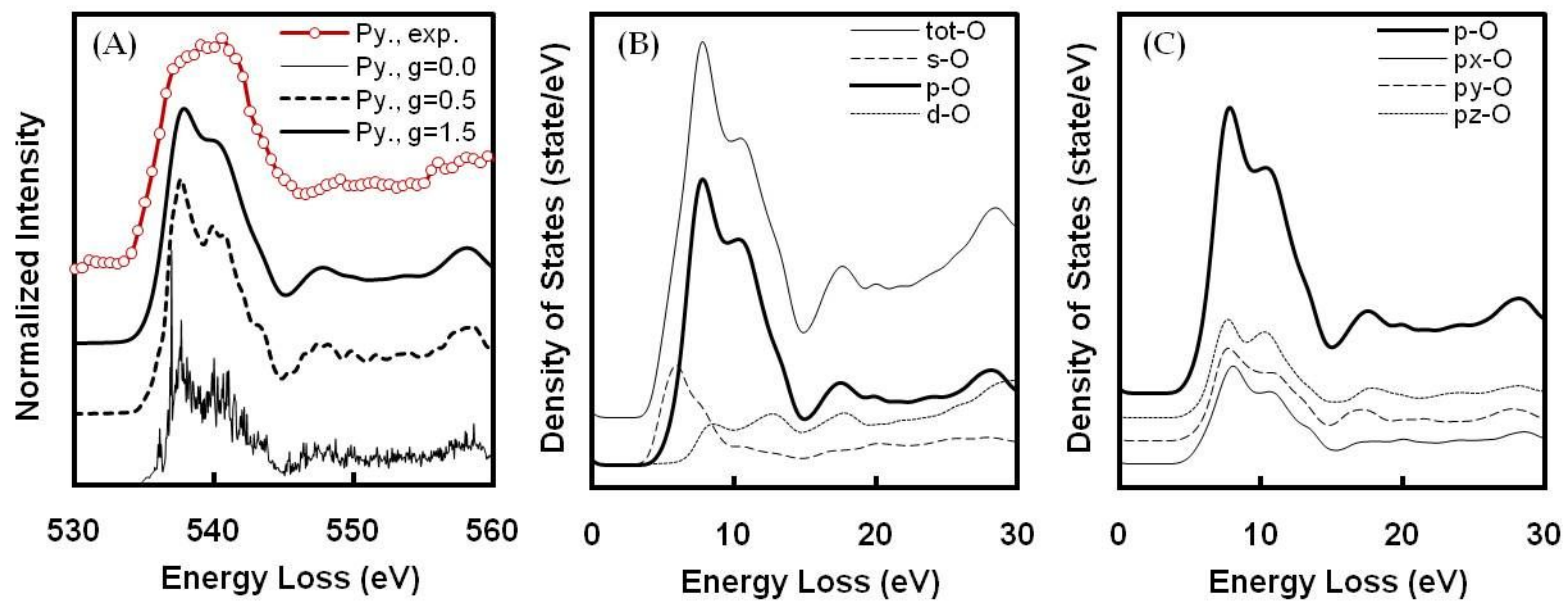


Figure 21. The calculated and experimental results of MgSiO₃ pyroxene (Py; ortho-enstatite). (A) the oxygen K-edge ELNES spectra. (B) the partial density of states of oxygen. (C) the directional components in p-orbital of oxygen.

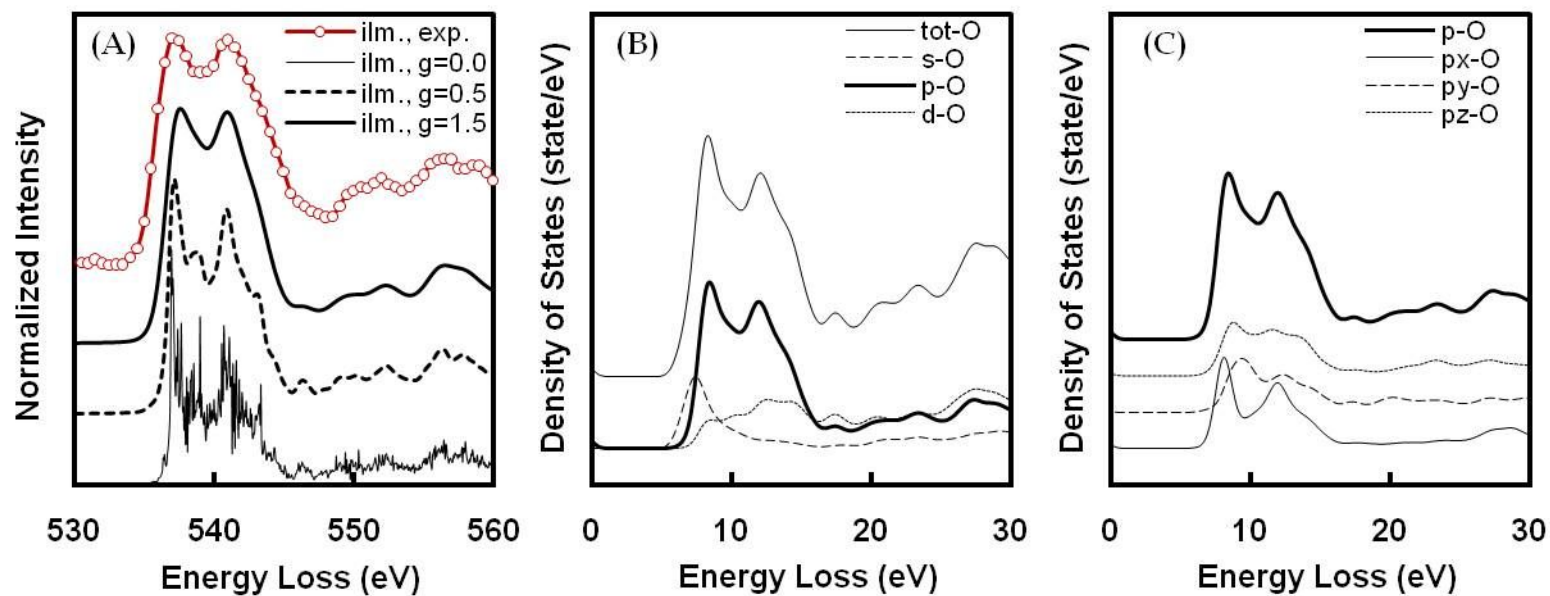


Figure 22. The calculated and experimental results of MgSiO₃ ilmenite (ilm). (A) the oxygen K-edge ELNES spectra. (B) the partial density of states of oxygen. (C) the directional components in p-orbital of oxygen.

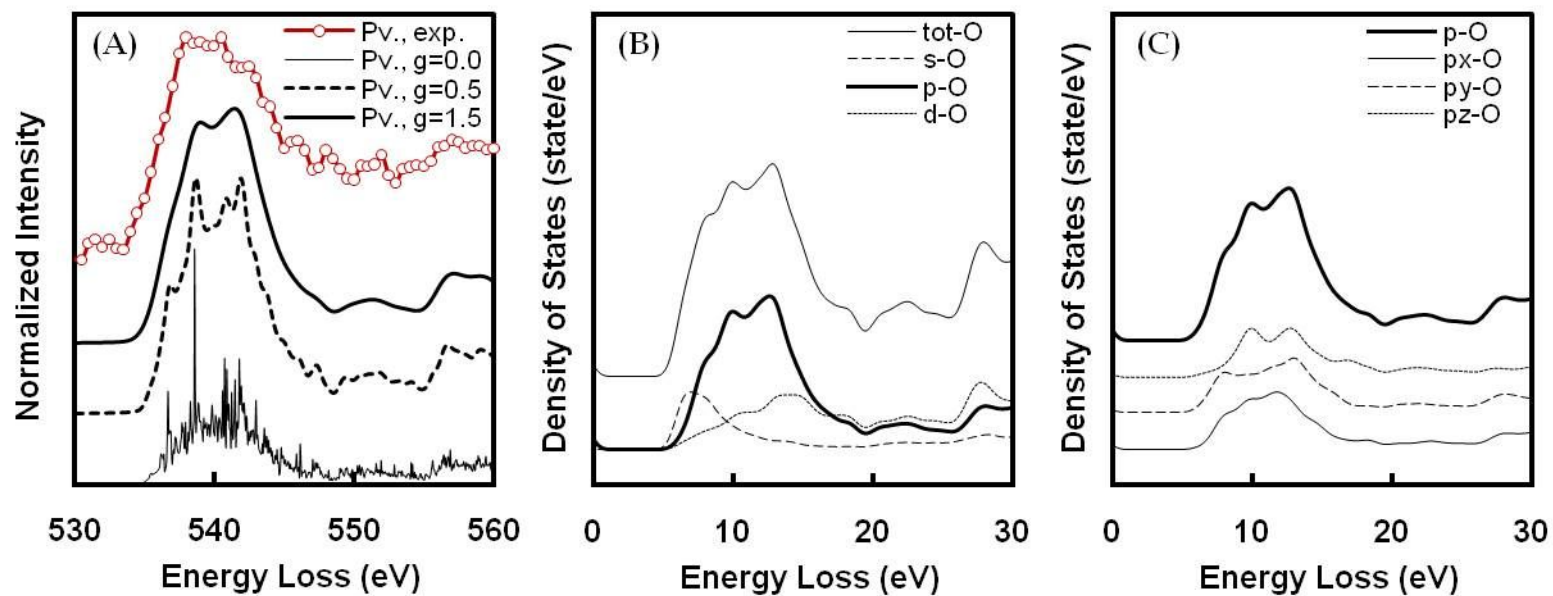


Figure 23. The calculated and experimental results of MgSiO₃ perovskite (Pv). (A) the oxygen K-edge ELNES spectra. (B) the partial density of states of oxygen. (C) the directional components of p-orbital of oxygen.

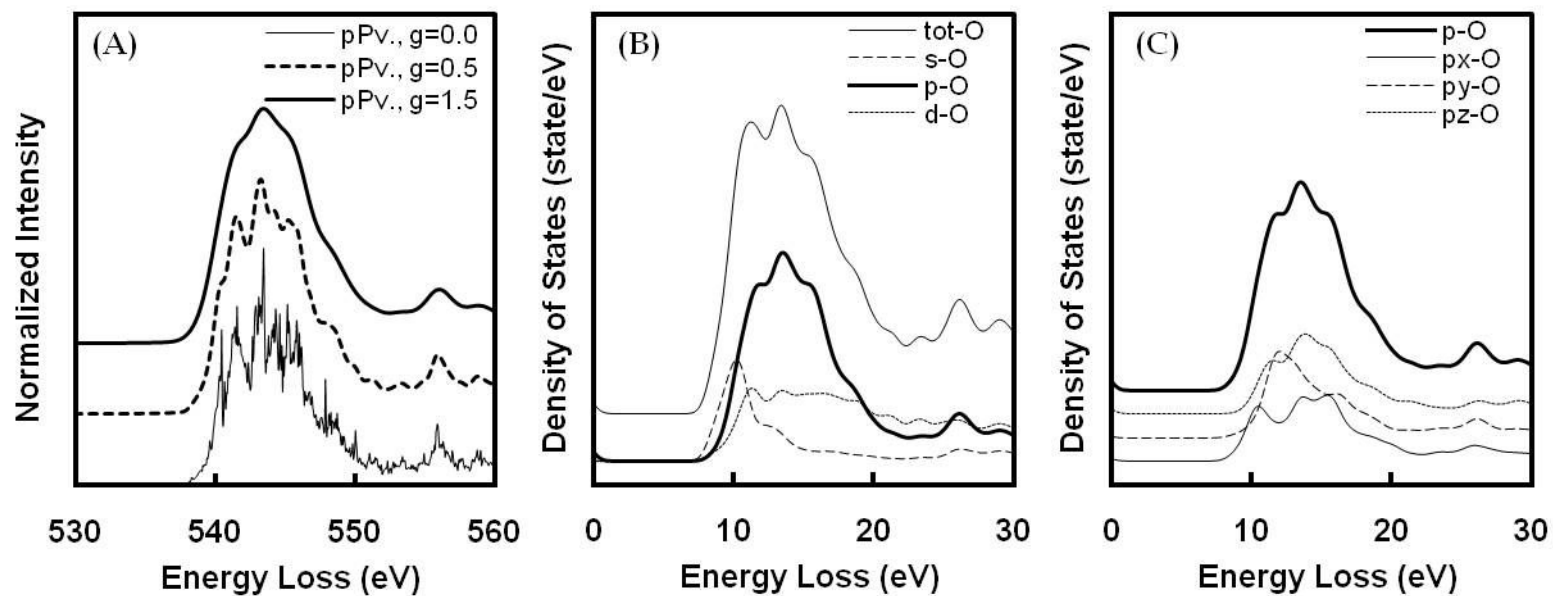


Figure 24. The calculated results of MgSiO₃ post-perovskite (pPv). (A) the oxygen K-edge ELNES spectra. (B) the partial density of states of oxygen. (C) the directional components in p-orbital of oxygen.

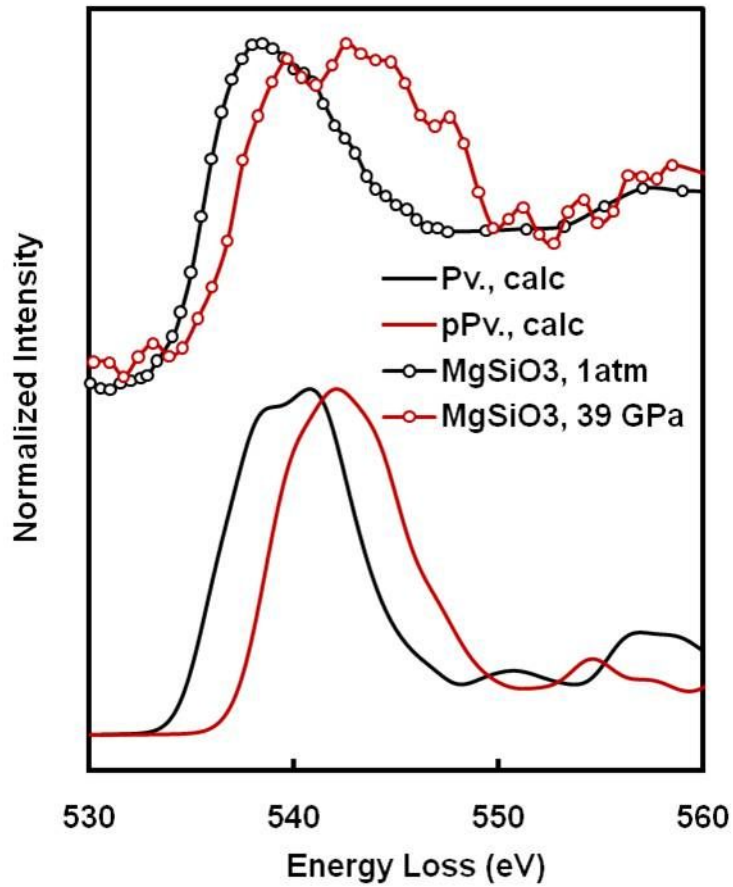


Figure 25. The oxygen K-edge XRS spectra of MgSiO₃ glasses at 1 atm and ≈39 GPa and calculated ELNES spectra of MgSiO₃ perovskite (Pv) and post-perovskite (pPv)

References

References from 1 to 18 are used in the first chapter, and from 19 to 50 for the second chapter.

1. Lee, S.K., et al., *Nature of polymerization and properties of silicate melts and glasses at high pressure*. *Geochimica et Cosmochimica Acta*, 2004. **68**(20): p. 4189-4200.
2. Lee, S.K., *Structure of silicate glasses and melts at high pressure: Quantum chemical calculations and solid-state NMR*. *Journal of Physical Chemistry B*, 2004. **108**(19): p. 5889-5900.
3. Hollas, J.M., *Modern Spectroscopy*. 4 ed. 2004: Wiley & Sons, Ltd.
4. Duer, M.J., *Introduction to Solid-State NMR Spectroscopy*. 2004: Blackwell.
5. Levitt, M.H., *Spin Dynamics: Basic of Nuclear Magnetic Resonance*. 2001: Wiley & Sons, Ltd.
6. Levine, I.N., *Quantum Chemistry*. 5 ed. 2006: Prentice Hall.
7. Griffiths, D.J., *Introduction to Quantum Mechanics*. 2 ed. 2005: Prentice Hall.
8. Mysen, B. and P. Richet, *Silicate Glasses and Melts*. *Developments in Geochemistry*. 2005: Elsevier. 35-124.
9. Gibbs, P. *Is glass liquid or solid?* 1997; Available from: <http://math.ucr.edu/home/baez/physics/General/Glass/glass.html>.

10. Lee, S.K. and J.F. Stebbins, *The structure of aluminosilicate glasses: High-resolution O-17 and Al-27 MAS and 3QMAS*. Journal of Physical Chemistry B, 2000. **104**(17): p. 4091-4100.
11. Stebbins, J.F., S.K. Lee, and J.V. Oglesby, *Al-O-Al oxygen sites in crystalline aluminates and aluminosilicate glasses: High-resolution oxygen-17 NMR results*. American Mineralogist, 1999. **84**(5-6): p. 983-986.
12. Charpentier, T., P. Kroll, and F. Mauri, *First-Principles Nuclear Magnetic Resonance Structural Analysis of Vitreous Silica*. Journal of Physical Chemistry C, 2009. **113**(18): p. 7917-7929.
13. Clark, T.M., et al., *Correlated structural distributions in silica glass*. Physical Review B, 2004. **70**(6): p. 8.
14. Bouhifd, M.A., A.P. Jephcoat, and S.P. Kelley, *Argon solubility drop in silicate melts at high pressures: A review of recent experiments*. Chemical Geology, 2008. **256**(3-4): p. 252-258.
15. Bouhifd, M.A. and A.P. Jephcoat, *Aluminium control of argon solubility in silicate melts under pressure*. Nature, 2006. **439**(7079): p. 961-964.
16. Lee, S.K., et al., *X-ray Raman scattering study of MgSiO₃ glass at high pressure: Implication for triclustered MgSiO₃ melt in Earth's mantle*. Proceedings of the National Academy of Sciences of the United States of America, 2008. **105**(23): p. 7925-7929.
17. Chamorro-Perez, E., et al., *Low argon solubility in silicate melts at high pressure*. Nature, 1998. **393**(6683): p. 352-355.
18. White, B.S., M. Brearley, and A. Montana, *Solubility of Argon in Silicate Liquids at High-Pressure*. American Mineralogist, 1989. **74**(5-6): p. 513-529.
19. Tse, J.S., *Ab Initio Molecular Dynamics With Density Functional Theory*. Annual Review of Physical Chemistry, 2002. **53**(1): p. 249-290.

20. Payne, M.C., et al., *Iterative minimization techniques for ab initio total-energy calculations: molecular dynamics and conjugate gradients*. *Reviews of Modern Physics*, 1992. **64**(4): p. 1045.
21. Oganov, A.R. and C.W. Glass, *Crystal structure prediction using ab initio evolutionary techniques: Principles and applications*. *The Journal of Chemical Physics*, 2006. **124**(24): p. 244704-15.
22. Cygan, R.T. and J.D. Kubicki, eds. *Molecular Modeling Theory: Applications in the Geoscience*. *Reviews in Mineralogy and Geochemistry*, ed. J.J. Rosso and P.H. Ribbe. Vol. 42. 2001, The Mineralogical Society of America. 1-30.
23. Neuville, D.R., et al., *The crystal and melt structure of spinel and alumina at high temperature: An in-situ XANES study at the Al and Mg K-edge*. *Geochimica Et Cosmochimica Acta*, 2009. **73**(11): p. 3410-3422.
24. Lin, J.F., et al., *Electronic bonding transition in compressed SiO₂ glass*. *Physical Review B*, 2007. **75**.
25. de Groot, F., *High resolution X-ray emission and X-ray absorption spectroscopy*. *Chemical Reviews*, 2001. **101**(6): p. 1779-1808.
26. Cabaret, D., et al., *Full multiple scattering calculations of the X-ray absorption near edge structure at the magnesium K-edge in pyroxene*. *American Mineralogist*, 1998. **83**(3-4): p. 300-304.
27. Kittel, C., *Introduction to solid state physics*. 8 ed. 2004: Wiley.
28. Ashcroft, N.W. and N.D. Mermin, *Solid State Physics*. 1976: Brooks/Cole.
29. Luitz, J., *Simulation of core level spectra using density functional theory*, in *Engineering Chemistry*. 2006, Technische Universität Wien.
30. Hebert, C., *Practical aspects of running the WIEN2k code for electron spectroscopy*. *Micron*, 2007. **38**(1): p. 12-28.

31. Singh, D.J. and L. Nordstrom, eds. *Planewaves, pseudopotentials, and the LAPW method*. 2nd ed. 2006, Springer.
32. Schwarz, K. and P. Blaha, *Solid state calculations using WIEN2k*. Computational Materials Science, 2003. **28**(2): p. 259-273.
33. Schwarz, K., *DFT calculations of solids with LAPW and WIEN2k*. Journal of Solid State Chemistry, 2003. **176**: p. 319-328.
34. Hebert, C., J. Luitz, and P. Schattschneider, *Improvement of energy loss near edge structure calculation using Wien2k*. Micron, 2003. **34**(3-5): p. 219-225.
35. Schwarz, K., P. Blaha, and G.K.H. Madsen, *Electronic structure calculations of solids using the WIEN2k package for material sciences*. Computer Physics Communications, 2002. **147**(1-2): p. PII S0010-4655(02)00206-0.
36. Blaha, P., et al. *WIEN2k, An augmented plane wave + local orbitals program for calculating crystal properties*. 2001; Available from: <http://www.wien2k.at>.
37. Momma, K. and F. Izumi, *VESTA: a three-dimensional visualization system for electronic and structural analysis*. Journal of Applied Crystallography, 2008. **41**: p. 653-658.
38. Fukui, H., et al., *X-ray Raman scattering for structural investigation of silica/silicate minerals*. Physics and Chemistry of Minerals, 2009. **36**(3): p. 171-181.
39. Gaudio, S.J., S. Sen, and C.E. Lesher, *Pressure-induced structural changes and densification of vitreous MgSiO₃*. Geochimica et Cosmochimica Acta, 2008. **72**(4): p. 1222-1230.
40. Hemley, R.J., ed. *Ultrahigh-pressure mineralogy: Physics and chemistry of the Earth's deep interior*. Reviews in mineralogy, ed. P.H. Ribbe. Vol. 37. 1998, Mineralogical society of America: Washington, DC.
41. Pijush and K. K., *Fluid Mechanics*. 3rd ed. 2004: Elsevier.

42. March, N.H. and M.P. Tosi, *Introduction to Liquid state physics*. 2004: World Scientific Publishing.
43. Pepin, R.O., *On The Origin and Early Evolution of Terrestrial Planet Atmospheres and Meteoritic Volatiles*. *Icarus*, 1991. **92**(1): p. 2-79.
44. Lee, S.K., et al., *Oxygen-17 nuclear magnetic resonance study of the structure of mixed cation calcium-sodium silicate glasses at high pressure: Implications for molecular link to element partitioning between silicate liquids and crystals*. *Journal of Physical Chemistry B*, 2008. **112**(37): p. 11756-11761.
45. Glinnrmann, et al., *Crystal structures of the low-temperature quartz-type phases of SiO₂ and GeO₂ at elevated pressure*. *Zeitschrift für Kristallographie*, 1992. **198**: p. 177-212.
46. Levien, L. and C.T. Prewitt, *High-Pressure Crystal-Structure and Compressibility of Coesite*. *American Mineralogist*, 1981. **66**(3-4): p. 324-333.
47. Ross, N.L., et al., *High-Pressure Crystal-Chemistry of Stishovite*. *American Mineralogist*, 1990. **75**(7-8): p. 739-747.
48. Horiuchi, H., E. Ito, and D.J. Weidner, *Perovskite-Type MgSiO₃ - Single-Crystal X-ray Diffraction Study*. *American Mineralogist*, 1987. **72**(3-4): p. 357-360.
49. Ohashi, Y., *Polysynthetically-Twinned Structures of Enstatite and Wollastonite*. *Physics and Chemistry of Minerals*, 1984. **10**(5): p. 217-229.
50. Murakami, M., et al., *Post-perovskite phase transition in MgSiO₃*. *Science*, 2004. **304**(5672): p. 855-858.

압력에 의한 규산염 비정질 또는 용융체의 원자 구조의 변화를 이해하는 것은 지구 내부의 결정-용융상의 경계부분에서 일어나는 원소의 분배현상 (crystal-melts elements partitioning), 화학적 분화현상 (chemical differentiation), 불활성 기체의 용해도 변화와 같은 현상들을 이해하는데 매우 중요하다. 하지만 비정질 물질의 원자 구조를 직접적으로 분석할 수 있는 알맞은 분석 방법의 부재로 인하여, 위와 같은 규산염 비정질 물질의 구조에 대한 연구는 비교적 최근까지 여러 가지 방면에서 부족한 상황이었다. 근래에 접어들어, 고해상도 고상 핵자기 공명 분광장치 (high-resolution solid-state nuclear magnetic resonance spectrometer; NMR), 비-공명 X-선 Raman 산란 (non-resonant x-ray Raman scattering) 실험, 양자화학계산 (quantum chemical calculations; first-principle calculations)의 발전에 힘입어 규산염 비정질 물질의 원자 구조를 직접적으로 상세하게 파악할 수 있게 되었다. 본 연구에서는 NMR 의 1D MAS 와 2D 3QMAS 실험을 이용하여 Na 이 첨가된 알루미늄-규산염 (Na-aluminosilicate) 비정질 물질의 시료들에 나타나는 압력에 의한 원자단위에서의 구조적 변화, 위상적 변화를 성분과 압력의 변화에 따른 체계적인 변화를 확인하였다. 그리고 양자화학계산을 통한 산소원자의 ELENES (oxygen K-edge ELNES; energy-loss near-edge structure) 스펙트럼을 얻어 압력의 변화에 따른 마그네슘-규산염 (Mg-silicate) 비정질 물질의 국부적인 전기적 환경 (local

electronic environments)의 변화를 확인하고 이를 관련된 이전 실험 결과와 비교 분석하였다.

첫 번째 장에서는, ^{27}Al 과 ^{17}O 의 1D MAS 와 2D 3QMAS 실험을 통하여 Na 이 첨가된 알루미늄-규산염 비정질 물질을, 그 성분 조성의 변화와 압력 조건의 변화 (1 기압 ~ 8 GPa)에 따라 분석하여 연결구조 교란 양이온 (network modifying cation)으로 작용하는 Na 이 압력에 의한 규산염 비정질 물질의 구조 변화에 미치는 영향을 조사하였다. 이러한 실험의 결과들은 연결구조 교란 양이온이 압력에 의한 규산염 비정질 물질의 구조 변화에 미치는 영향을 뚜렷하게 보여주며, 낮은 압력에서 상대적으로 중합도가 높은 규산염 비정질 물질이 고압의 상태에서 더 높은 중합도를 갖는 구조를 형성할 수 있는 가능성을 시사하고 있다.

두 번째 장에서는, FP-LAPW (full-potential linearized augmented plane wave) 방법론을 적용한 계산 프로그램을 이용하여 얻은 MgSiO_3 와 SiO_2 결정질 동질이상 물질들의 산소 K-edge ELNES 스펙트럼을 얻고, 이를 통하여 비정질 MgSiO_3 의 고압상태에서 전기적 연결구조 (electronic bonding structure)에 대한 정보를 얻을 수 있었다. 계산된 산소원자의 ELNES 스펙트럼은 고압상태의 동질이상인 perovskite 와 post-perovskite 에 대하여 특징적인 스펙트럼을 보여준다. MgSiO_3 perovskite 의 $^{16}\text{Si-O-}^{16}\text{Si}$ (i.e., corner-sharing oxygen)는 ≈ 540 eV 부근에서, MgSiO_3 post-perovskite 의 $^{16}\text{Si-O-}2^{16}\text{Si}$ (i.e., edge-sharing oxygen)은 ≈ 545 eV 부근에서 스펙트럼의 최대값을 보여주고 있다. 이러한 스펙트럼의

변화는 비정질 MgSiO_3 의 압력의 증가에 따른 스펙트럼의 변화와 유사한 양상을 보여준다. MgSiO_3 post-perovskite 의 edge-sharing 산소와 산소 tri-clusters (i.e., 고배위수의 Si 원자 3 개가 연결된 산소원자)와 유사한 원자 구조 (atomic configuration)을 갖고 있는 것으로 유추하여, 현재까지의 결과가 이전 연구에서 고압상태의 비정질 Mg-규산염 물질에서 나타난 ≈ 545 eV 가 산소 tri-clusters 에서 기원했다는 제안은 옳은 것으로 생각된다. 위와 같은 실험 및 계산 결과들은 압력에 의한 비정질 규산염 물질들의 원자 구조의 변화와 연결구조 교란 양이온이 이러한 현상에 미치는 영향들을 설명해주고 있다. 이를 통하여 지구 내부의 압력의 증가에 따른 규산염 용융체의 원자 구조의 변화를 고려함으로써 이전 연구들로부터 얻어진 단편적인 지식들에 대한 더욱 상세하고 체계적인 이해를 도모하며, 전 지구적인 시스템의 진화를 이해하는데 있어서도 중요한 정보들을 제공할 수 있을 것으로 기대된다.

주요어: 비정질 Na-알루미노 규산염, 고압, 연결구조 교란 양이온, 고상 핵자기공명 분광장치, 산소원자 K-edge

학번: 2008-20409

감사의 글

NMR 이라는 실험 장비와 비탄선 X-선 산란 실험이나 관련된 양자화학계산들은 대학원에 입학하기 전에는 매우 생소하고 동떨어진 주제들이었습니다. 그렇기 때문에, 처음 연구를 시작하며 실험과 계산을 배우는 과정에서 많은 실수와 어려움이 있었습니다. 하지만 지도 교수님이신 이성근 교수님의 많은 지도와 관련 학과의 여러 교수님들의 뛰어난 강의를 통하여 다양한 경험과 지식을 쌓을 수 있었고, 덕분에 미력하나마 이 글을 완성할 수 있었습니다. 먼저, 바쁘신 와중에도 졸작의 심사에 시간을 할애하여 주신 이용일 교수님과 이준기 교수님께 감사의 인사를 올립니다. 그리고 NMR 실험에 이용된 고압 시료의 합성에 도움을 주신 동경대학교 지진연구소의 三部賢治 (Mibe Kenji) 교수님께도 감사 드립니다.

같은 연구실에서 학회 때를 비롯하여 여러 가지 부족한 점을 도와주셨던 이범한 선배님께도 감사 드립니다. 대학원 생활을 하는 도중에 여러 가지 어려움이 많았지만 김현나 선배님의 조언과 도움이 있어 여러 가지를 극복할 수 있었습니다. 그리고 같이 대학원에 입학하여 어느덧 2 년이라는 시간을 함께 보내고 여러 가지 일들에 신경을 써준 박선영 양에게도 감사의 말을 드립니다. 지난 학기에 대학원에 입학하여 연구실의 일원으로 합류하여 연구실 생활에 많은 도움을 주고 있는 김효임, 김은정 후배님들께도 감사 드립니다. 다른

연구실에 있지만, 여러 가지 상담을 해주고 도움을 주신 한영철 선배님께도 감사의 말씀을 드립니다.

대학원에 입학한 이후로는 많이 소홀해진 것 같지만, 6 년이라는 시간 동안 얼굴을 보며 술잔을 기울였던 재석이, 성재, 지금은 군복무중인 승윤이, 큰형님, 길 건너 동네에 살면서 수시로 술친구가 되어준 희근이 항상 내 불평불만을 들어줘서 고맙다는 말을 전하고 싶습니다. 말상대가 되어주고 여러 가지 컴퓨터 관련 문제를 던져주어 스트레스를 푸는데 도움을 줬던 지원누나에게도 작은 감사를 전합니다. 그리고 후배이지만 후배 같지 않고 잘 어울려 줬던 세진이와 방원이에게 감사의 말을 전합니다. 그리고 일일이 열거할 수는 없지만, 여러 도움을 주고 받았던, 대학 동기 친구들에게 모두 감사의 말을 전하고 싶습니다.

마지막으로 항상 저를 생각해주시고, 지금까지 물심양면으로 지원을 해주신 부모님께 가장 깊은 감사의 말씀을 올립니다.



저작자표시-비영리-변경금지 2.0 대한민국

이용자는 아래의 조건을 따르는 경우에 한하여 자유롭게

- 이 저작물을 복제, 배포, 전송, 전시, 공연 및 방송할 수 있습니다.

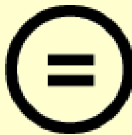
다음과 같은 조건을 따라야 합니다:



저작자표시. 귀하는 원저작자를 표시하여야 합니다.



비영리. 귀하는 이 저작물을 영리 목적으로 이용할 수 없습니다.



변경금지. 귀하는 이 저작물을 개작, 변형 또는 가공할 수 없습니다.

- 귀하는, 이 저작물의 재이용이나 배포의 경우, 이 저작물에 적용된 이용허락조건을 명확하게 나타내어야 합니다.
- 저작권자로부터 별도의 허가를 받으면 이러한 조건들은 적용되지 않습니다.

저작권법에 따른 이용자의 권리는 위의 내용에 의하여 영향을 받지 않습니다.

이것은 [이용허락규약\(Legal Code\)](#)을 이해하기 쉽게 요약한 것입니다.

[Disclaimer](#)

Thesis submitted in partial fulfillment
for the M. Sc. Degree requirement

Pressure-Induced Structural Changes in Sodium-
Aluminosilicate Glasses and Crystalline Magnesium-
Silicates using High-Resolution Solid-State NMR and
Quantum Chemical Calculations: Implications for Atomic
Structure of Melts in Earth's interior

2 차원 고상 핵자기공명 분광장치와 양자화학 계산을
이용한, 압력에 의한 비정질 Na-알루미노 규산염과
결정질 Mg-규산염 광물의 원자 구조변화: 지구 내부의
규산염 용융체의 고압 구조에 대한 고찰

Yi Yoo Soo

The Faculty of Graduate Studies
Seoul National University
School of Earth and Environmental Science

February 2010

Pressure-Induced Structural Changes in Sodium-
Aluminosilicate Glasses and Crystalline Magnesium-
Silicates using High-Resolution Solid-State NMR and
Quantum Chemical Calculations: Implications for Atomic
Structure of Melts in Earth's interior

2 차원 고상 핵자기공명 분광장치와 양자화학 계산을
이용한, 압력에 의한 비정질 Na-알루미노 규산염과
결정질 Mg-규산염 광물의 원자 구조변화: 지구 내부의
규산염 용융체의 고압 구조에 대한 고찰

지도교수 이성근

이 논문을 석사학위 논문으로 제출함

2010 년 2 월

서울대학교 대학원

지구환경과학부

이유수 (李儒秀)

이유수의 이학석사 학위논문을 인준함

2010 년 2 월

위 원 장 이 용 일 (인)

부위원장 이 준 기 (인)

위 원 이 성 근 (인)

Abstract

Despite the significant importance and implications for geochemical processes in Earth's interior including chemical differentiation, the pressure-induced changes in atomic configurations of silicate glasses and melts and their densification mechanisms at high pressure have not been well understood due to the lack of suitable experimental techniques and theoretical methods. The recent progresses and advances in high-resolution solid-state NMR, synchrotron X-ray Raman scattering, and first-principle calculations allow us to investigate the previously unknown details of the pressure-induced structural changes in silicate glasses and melts at high pressure. In this study, we explored the effect of Na content on the pressure-induced structural and topological changes in the aluminosilicate glasses using 2-dimensional triple-quantum (3Q) magic-angle spinning (MAS) NMR (in Chapter 1). We also explore the pressure-induced changes in local electronic bonding structures of diverse crystalline Mg-silicate polymorphs using first-principle calculations to have better insight into the experimental X-ray Raman scattering spectra for silicate glasses and the nature of bonding transitions in oxides at high pressure in general (in Chapter 2).

In chapter 1, we present the ^{27}Al and ^{17}O MAS and 2D 3QMAS NMR spectra for peralkaline, partially depolymerized Na-aluminosilicate glasses with varying chemical composition and pressure from 1 atm to 8 GPa. The

current results show that the higher degree of polymerization of silicate melts at ambient pressure could facilitate a further polymerization of silicate melts at high pressure at the expense of non-bridging oxygen. The degree of polymerization in Na-aluminosilicate glasses, therefore, increases with increasing pressure but decreases with network modifying Na content, while the nature of polymerization in silicate melts at high pressure affects their macroscopic properties of silicate melts at high pressure.

In chapter 2, we present the results of theoretical calculations of oxygen K-edge features for MgSiO_3 and SiO_2 crystalline polymorphs based on full-potential linearized augmented plane wave (LAPW) methods. The calculated oxygen K-edge electron excitation spectra for various crystalline Mg-silicates (e.g., x-ray absorption spectroscopy, electron energy loss spectroscopy, and x-ray Raman scattering spectroscopy) show that diverse oxygen configurations in these high pressure polymorphs have characteristic oxygen K-edge features. Particularly, a corner-sharing oxygen (${}^{[6]}\text{Si-O-}{}^{[6]}\text{Si}$) in MgSiO_3 perovskite leads to a oxygen K-edge features around 540 eV while a edge-sharing oxygen (${}^{[6]}\text{Si-O-}2{}^{[6]}\text{Si}$) in MgSiO_3 post-perovskite results in features around 545 eV. This trend and a magnitude of changes (≈ 5 eV) are similar to what has been reported for pressure-induced changes in oxygen K-edge features in MgSiO_3 glasses. As the edge-sharing oxygen in MgSiO_3 post-perovskite has similar atomic configuration with that of oxygen tri-clusters (i.e., oxygen coordinated by three highly coordinated Si atoms), the current results imply that the previous assignment of the ≈ 545 eV feature as oxygen tri-cluster in Mg-silicate glass

at high pressure about 20 GPa is likely to be correct. The experimental and theoretical results and methods in the current study will provide improved understanding of the atomistic origins of diverse macroscopic properties and geophysical and geochemical properties in Earth's interior.

Key Words: Na-aluminosilicate glass, high pressure, network modifying cation, NMR, Mg-silicates, oxygen K-edge

Student Number: 2008-20409

Table of Contents

Introduction	1
1. The Effect of Network Modifying Cation on Pressure-Induced Structural Changes in Na-aluminosilicate glasses and melts: high-resolution solid-state NMR study	4
1.1. Introduction	4
1.2. Theoretical Backgrounds	5
1.2.1. Introduction to NMR Spectroscopy	5
1.2.2. Principles of NMR Spectroscopy	7
1.2.3. Natures of Glasses and Melts	14
1.3. Results and Discussions	16
1.3.1. Experiments	16
1.3.2. Results	18
1.3.3. Discussions	23
2. Theoretical Studies of the Local Electronic Environments of Oxygen in Mg-silicates at high pressure using ELNES (Energy-Loss Near-Edge Structure)	44
2.1. Introduction	44
2.2. Theoretical Backgrounds	47
2.2.1. Principles of Non-Resonant X-ray Raman Scattering Spectroscopy	47
2.2.2. Principles of the First-Principle Calculation Methods	54
2.3. Results and Discussions	61
2.3.1. Experiments and Calculations	61
2.3.2. Results	64
2.3.3. Discussion	69
3. Conclusion	72
References	86
국문 요약	91
감사의 글	94

List of Figures and Tables

Figure 1. The ^{27}Al 1D MAS spectra of Na-aluminosilicate glasses with varying pressure	27
Figure 2. The ^{27}Al 2D 3QMAS spectra of Na-aluminosilicate glasses with varying pressure (total 20 contour lines are drawn from 4 to 98%).....	28
Figure 3. The proportion of each $^{\text{IV}}\text{Al}$ in Na-aluminosilicate glasses with varying pressure	29
Figure 4. The average coordination number of Na-aluminosilicate glasses at 6 GPa.....	30
Figure 5. The overlapped ^{27}Al 2D 3QMAS spectra of Na-aluminosilicate glasses at ambient pressure.....	31
Figure 6. The isotropic projection of ^{27}Al 2D 3QMAS spectra of Na-aluminosilicate glasses at ambient pressure	32
Figure 7. The quadrupolar coupling products (P_q) of ^{27}Al in Na-aluminosilicate glasses with varying pressure	34
Figure 8. The ^{17}O 1D MAS spectra of Na-aluminosilicate glasses with varying pressure	35
Figure 9. The ^{17}O 2D 3QMAS spectra of Na-aluminosilicate glasses with varying pressure (total 20 contour levels from 4 to 98%, added lines at 5 and 6.5%)	36
Figure 10. The isotropic projection of ^{17}O 2D 3QMAS spectra of Na-aluminosilicate glasses.....	37
Figure 11. The schematic picture of atomic structure of polymerization process in Na-aluminosilicate glasses. (A) $^{\text{IV}}\text{Si-O-}^{\text{IV}}\text{Al} + \text{Na-O-}^{\text{IV}}\text{Si}$. (B) $^{\text{IV}}\text{Si-O-}^{\text{V}}\text{Al} + \text{Na}^*$	38
Figure 12. The proportion of $^{\text{IV}}\text{Al-O-}^{\text{IV}}\text{Al}$ high energy cluster in NAS150520 glasses with varying pressure.....	39
Figure 13. The quadrupolar coupling products (P_q) of ^{17}O in Na-aluminosilicate glasses with varying pressure (P_q values are estimated from its peak position except $^{\text{IV}}\text{Si-O-}^{\text{IV}}\text{Si}$ which is calculated from its center of gravity of peak.).....	41

Figure 14. The schematic picture of atomic structure for decreasing $^{44}\text{Si-O-}^{44}\text{Si}$ bond angle	42
Figure 15. The pressure dependence of Ar gas solubility of Anorthite ($\text{CaAl}_2\text{Si}_2\text{O}_8$) glasses [15, 17, 18]	43
Figure 16. The crystal structures of SiO_2 and MgSiO_3 polymorphs. (A) the crystalline SiO_2 polymorphs; alpha-quartz, coesite, stishovite. (B) the crystalline MgSiO_3 polymorphs; ilmenite, ortho-enstatite (pyroxene), perovskite, post-perovskite	76
Figure 17. The oxygen K-edge experimental XRS and calculated ELNES spectra of alpha-quartz and crystalline MgSiO_3 polymorphs	77
Figure 18. The calculated and experimental results of SiO_2 alpha-quartz. (A) the oxygen K-edge ELNES spectra. (B) the partial density of states (p-DOS) of oxygen. (C) the directional components in p-orbital of oxygen.....	78
Figure 19. The calculated results of SiO_2 coesite. (A) the oxygen K-edge ELNES spectra. (B) the partial density of states of oxygen. (C) the directional components in p-orbital of oxygen.....	79
Figure 20. The calculated results of SiO_2 stishovite. (A) the oxygen K-edge ELNES spectra. (B) the partial density of states of oxygen. (C) the directional components in p-orbital of oxygen.....	80
Figure 21. The calculated and experimental results of MgSiO_3 pyroxene (Py; ortho-enstatite). (A) the oxygen K-edge ELNES spectra. (B) the partial density of states of oxygen. (C) the directional components in p-orbital of oxygen.....	81
Figure 22. The calculated and experimental results of MgSiO_3 ilmenite (ilm). (A) the oxygen K-edge ELNES spectra. (B) the partial density of states of oxygen. (C) the directional components in p-orbital of oxygen.....	82
Figure 23. The calculated and experimental results of MgSiO_3 perovskite (Pv). (A) the oxygen K-edge ELNES spectra. (B) the partial density of states of oxygen. (C) the directional components of p-orbital of oxygen.....	83
Figure 24. The calculated results of MgSiO_3 post-perovskite (pPv). (A) the oxygen K-edge ELNES spectra. (B) the partial density of states of oxygen. (C) the directional components in p-orbital of oxygen.	84

Figure 25. The oxygen K-edge XRS spectra of MgSiO_3 glasses at 1 atm and ≈ 39 GPa and calculated ELNES spectra of MgSiO_3 perovskite (Pv) and post-perovskite (pPv)..... 85

Table 1. The composition of prepared sample..... 26

Table 2. The isotropic chemical shift of ^{27}Al in Na-aluminosilicate glasses. 33

Table 3. The proportion of $^{[4]}\text{Al}$ -O- $^{[4]}\text{Al}$ in NAS150520..... 40

Table 4. The crystallographic information of SiO_2 and MgSiO_3 polymorphs 75

Introduction

Aluminosilicate glasses and melts are one of the most common components of magmatic melts in Earth's interior, thus affect to the geophysically and geochemically important properties such like densification of magmatic melts, seismological anomalies in core-mantle boundary, and elements partitioning between silicate melts and crystals, etc. There exist many fundamental questions of aluminosilicate melts at Earth's deep inside; how does the local structure of silicate melts changes at high pressure, how this distorted local atomic structure affects to their macroscopic and thermodynamic properties, and also global geological processes. In spite of these importances of exploring the properties of aluminosilicate melts and glasses, the pressure-induced structural changes and their compositional effect on local atomic structure have not been fully understood, even though there have been enormous advances in both optical spectroscopic techniques for exploring the atomic structure of amorphous materials and experimental probes to reconstruct the extreme condition relevant to Earth's interior.

Recent advances in spectroscopic techniques especially for solid-state NMR with developments of experimental techniques, which could realize a relatively high pressure condition relevant to Earth's interior, allow us to explore the atomic structure of aluminosilicate glasses synthesized at high pressure. The structure of aluminosilicate glasses

synthesized at high pressure have been studied particularly about their ordering behavior of framework cation, however the fundamental effect of network modifying cation on structural changes with increasing pressure has not been understood clearly including the densification mechanism of multi-component melts in Earth's interior. The quantum chemical calculations provide the complementary insight about the valuable properties of silicate glasses and amorphous structure at extreme condition relevant to Earth's deep inside, where it is very difficult and laborious doing in-situ experiments the materials of Earth's deep inside. The theoretical approaches of exploring Earth materials are relatively easy to access the extreme pressure-temperature condition than the experimental apparatus, since the improvement of computation techniques provides the accurate results comparing with corresponding experimental results.

In this paper, we worked about mainly two topics of exploring Earth materials. In the first chapter, we present our recent NMR results which show the effect of network modifying cation on pressure-induced structural changes of Na-aluminosilicate glasses including its implications to the properties of magmatic melts at Earth's interior. In the second chapter, we present the theoretical studies of oxygen K-edge excitation spectra of crystalline Mg-silicate polymorphs to investigate their electronic bonding structure, and apply to understanding the not well-known electronic bonding structure of amorphous MgSiO_3 at high pressure. From the applications of these new and advanced techniques, high resolution solid-state NMR and first-principle calculations which have being

developed recently, we could note that these experimental and theoretical approaches to Earth materials at high pressure could shed light on the numerous new and significant geophysical and geochemical applications including the atomic structure of amorphous silicate oxides at high pressure-temperatures conditions. This text is organized in 3 chapters. The first chapter shows the results and discussions of ^{27}Al and ^{17}O solid-state NMR spectroscopic experiments with briefly summarized principles of NMR spectroscopy. The second chapter shows the calculated oxygen K-edge energy-loss near-edge structure (EELS) spectra for crystalline SiO_2 and MgSiO_3 polymorphs with relevant x-ray Raman scattering spectroscopic experimental results to understand the electronic bonding structure of MgSiO_3 glass at high pressure. The third chapter shows the conclusions of this work with implications on geophysical and geophysical properties in Earth's interior.

1. The Effect of Network Modifying Cation on Pressure-Induced Structural Changes in Na-aluminosilicate glasses and melts: high-resolution solid-state NMR study

1.1. Introduction

Despite the significant importance in understanding the nature of chemical differentiation and crystal-melt partitioning of elements in Earth's interior, the pressure-induced structural changes of aluminosilicate glasses and their densification mechanisms at high pressure have not been fully understood due to the lack of suitable experimental probes. The nuclear magnetic resonance (NMR) spectroscopy, which has been used to characterize organic molecules in liquid phase, is recently advanced in high-resolution solid-state NMR spectroscopy allowing us to explore the unknown atomic structural characteristics of silicate glasses and melts. The solid-state NMR spectroscopy, thus, has made the major contributions in elucidating the atomic structure of glasses and melts. Most of the previous works of verifying structural properties of silicate glasses and melts have focused on the pressure and temperature effects on the structure of amorphous Earth materials to understand the anomalous dynamic properties of glasses and melts [1, 2]. The systematic effects of composition (i.e., the role of network modifying cation, also called network modifier) in polymerization process of melts at high pressure, therefore, remains to be

explored because of the difficulties of designing appropriate sample system; and the results are expected to provide valuable information for exploring the magmatic melts in Earth's interior more systematically.

In this study, we explore the effect of Na content on the pressure-induced structural changes in the aluminosilicate glasses using 2D 3QMAS and 1D MAS NMR experiments. The ^{27}Al and ^{17}O MAS and 2D 3QMAS NMR spectra of highly polymerized glasses (i.e., silica rich) and relatively depolymerized glasses (i.e., Na rich) quenched from melts at 1 atm, 6 GPa, and 8 GPa were prepared, details of samples are summarized in experiments section. The results from these experiments suggest the possibility of that the network modifying cation could affect the polymerization of aluminosilicate melts at high pressure, and account for densification mechanism of geophysically important magmatic melts, providing enhanced prospects for crystal-melts partitioning, and chemical differentiation of magmas in Earth's interior.

1.2. Theoretical Backgrounds

1.2.1. Introduction to NMR Spectroscopy

The NMR spectroscopy allows us to explore the element specific atomic structure different from other conventional optical spectroscopic methods. The specific transition energy of each target nucleus induced

from external magnetic field, called the Zeeman Effect, is caused from the nuclear spin number which is one of the intrinsic properties of nuclei. Then, this separated energy level is used to probe the atomic structure by comparing the nuclei specific transition energy with that of standard sample (i.e., commonly used with external reference in solid-state NMR). In spite of the various possibilities of this element specific spectroscopic technique for exploring the amorphous system, there are still remaining problems to verify the condensed phase system comparing with liquid sample because of the relatively short relaxation time of condensed sample than that of liquid sample showing broad spectrum where the delta-function like spectrum in frequency domain (i.e., has high resolution enough to reconstruct atomic structure of organic materials in liquid phase such as protein) is appeared in liquid sample. Not only the shorter relaxation time but also the various quantum mechanical perturbations such as quadrupolar coupling effect affect to the NMR spectrum of solid-state sample. Several methods have been developed to improve the resolution of NMR spectrum with decreasing the perturbation effects for exploring the atomic structure of solid-state sample; DAS (dynamic angle spinning), MAS (magic angle spinning), and MQMAS (multiple-quantum transition MAS) [3-5].

The experimental results of NMR spectroscopy provide the atomic structural disorder of silicate glasses such as chemical short-range order distribution (i.e., especially the oxygen linkages in this work; Si-O-Si, Si-O-Al, etc.) and topological disorder which shows the state of order that stems

from the bond angle and bond length distribution of the system. From this information obtained from solid-state NMR spectroscopy, we could investigate structure of amorphous materials including silicate oxide glasses and melts.

1.2.2. Principles of NMR Spectroscopy

The briefly summarized methodologies of NMR spectroscopy are referred from following materials [3-7].

(i) The Zeeman Effect

The nuclear magnetic effect, of which the magnetic field induces the separated energy level of nuclear spin, is used in NMR spectrometer, and this effect is called as the Zeeman Effect. This separated energy levels make the characteristic spectral feature of nucleus (i.e., induced from different spin-relaxation time) providing the NMR spectroscopic information, 1-dimensional single and 2-dimensional triple quantum magic-angle spinning (1D MAS and 2D 3QMAS) spectrum. And the energy gap of this discrete energy level increases with increasing external magnetic field strength with relatively decreasing various perturbation effects (i.e., chemical anisotropy, quadrupolar interaction, etc.).

The total Hamiltonian (H) of nucleus, which is induced by an external magnetic field (B), is affected by the various perturbation effects

(H') comes from the magnetic dipole moment (μ). The spin (S) and angular (L) momentum are coupled (J) with considering the relativistic effect (g-factor) on the nucleus. The appropriate gyromagnetic ratio '2' on the total spin momentum should be considered due to the relativistic effects.

$$\hat{H} = \hat{H}_0 + \hat{H}', \quad \hat{H}' = -\vec{\mu} \cdot \vec{B} \quad (1-1)$$

$$\vec{\mu} = -\mu_B g \vec{J}, \quad \vec{J} = \vec{L} + 2 \cdot \vec{S} \quad (1-2)$$

(ii) Fundamental properties of spin and NMR signal

The external magnetic field induces not only the splitting of energy level but also the Larmor precession which is exerted by the torque between magnetic dipole moment of nuclear spin and external magnetic field (i.e., This description is a macroscopic view, the atomic origins of the Larmor precession comes from the general solution of time-dependent of Schrödinger equation solving spin-orbital function, the expectation S_x and S_y component oscillate with corresponding Larmor frequency with respect to z-axis external magnetic field.). The Larmor frequency (ω_0) provides an information of the frequency domain (ppm = frequency shift/ ω_0) in NMR spectrum. The FID (free induction decay) signal of NMR experiment is acquired with spin polarization induced from stimulating RF field of NMR spectrometer. This spin polarization provides the two intrinsic properties of the spin system called the spin-lattice relaxation (T_1) and transverse relaxation (T_2), and then the NMR spectrometer measures this relaxation signal radiated from the spin precession. This detected FID signal is transformed into frequency domain with the Fourier transformation

providing the chemical shift information which is originated from the magnetic shielding by local electronic environment.

(iii) Differences between the solid and liquid-state NMR spectroscopy

The NMR spectroscopy, especially the liquid-state NMR spectroscopy, has been being used in bio-science to investigate the multi-atomic molecular structure like protein with its high atomic structure resolving abilities in liquid phase sample; because the peak shape is similar to delta-function in the liquid-state NMR spectrum due to the decreasing of quantum mechanical perturbations including quadrupolar coupling effect which takes most part of the perturbation effects in solid-state NMR system. The isotropic liquids have a few percents of quadrupolar effect even the anisotropic liquids (i.e., the dipole-dipole coupling, quadrupolar coupling effect, etc.). These quantum mechanical perturbation effects make the peak shape broader than that of solid-state system, henceforth the spectrum is harder to resolve in frequency domain.

**(iv) The methods for reducing quantum mechanical perturbations
Magic-angle spinning (MAS) method**

The conventional NMR techniques of liquid-state NMR spectroscopy could not be used in exploring the atomic structure of solid phase materials. However, the recent advances in NMR techniques of solid-state NMR spectroscopy allow us to resolve the atomic structure of solid-state materials using NMR spectroscopy. There are many theoretical and

mechanical methods which could improve the resolution of peak with reducing or deselecting the perturbation effects induced from neighboring nucleus. One of the most used mechanical techniques is called MAS of which the sample rotor is spun in specific angle (i.e., magic angle; $3\cos^2\theta - 1 = 0$) to improve the peak resolution with removing the first order perturbation effect which comes from the chemical anisotropy of sample (H_{CS}) and makes the chemical shift anisotropy (δ_{CSA}).

$$H_{CS} \propto [\gamma B_0 + \{\delta_{iso} + \frac{1}{2} \delta_{CSA}(3 \cos^2 \theta - 1)\}] \quad (1-3)$$

Quadrupolar effect

The internal Hamiltonian of the nucleus has various perturbation terms, mainly first and second order perturbation effects; the first order perturbation effect is induced from the chemical shift anisotropy, dipolar coupling interactions, etc.; the second order perturbation effect is quadrupolar interaction. The second order quadrupolar interaction remains even though the chemical shift anisotropy is almost removed by MAS method; and this remaining quadrupolar interaction could be reduced in two ways. The first one is the stronger external magnetic field; the high magnetic field increases the Zeeman Effect and relatively reduces the perturbation effects. The other method averages the perturbation effects using mechanical probe called dynamic angle spinning (DAS); rotor is rotated in two specific angles, 37.38° and 79.19° and the corresponding equations are presented at below with tensor notation (i.e., the

conventionally expressed equations are could be found at related references).

$$\omega_Q^{(1)} = \frac{e^2 q Q}{4I(2I+1)} \{3m^2 - I(I+1)\} W_{20}^Q \quad (1-4)$$

$$\omega_Q^{(2)} = - \left(\frac{e^2 q Q}{4I(2I-1)} \right)^2 \frac{2}{\omega_0} m \cdot [\{I(I+1) - 3m^2\} V_{00}^Q + \{8I(I+1) - 12m^2 - 3\} V_{20}^Q + \{18I(I+1) - 34m^2 - 5\}] V_{40}^Q \quad (1-5)$$

$$V_{k0}^Q = \sum_n D_{n0}^k(\alpha, \beta, \gamma) A_{kn} \quad (1-6)$$

The multiple-quantum magic-angle spinning (MQMAS) method

The multiple-quantum transition (i.e., odd number excitation; 1, 3, 5 ...) is not affected by the second order quadrupolar interaction, this MQ transition could not be observed directly, differently from single-quantum transition. The quantum transition is treated as simple quantum coherence; however these two concepts are different because of the number of spins in the system. The spins, which are explored with NMR spectroscopy, have to be provided with thermal sensitivity using the concept of the ensemble average. This MQ transition evolves by the RF pulse and transferred into SQ transition with their corresponding quantum coherences. The MQ transition could be observed indirectly with varying evolving time (t_1) as time variable used in SQ excitation relaxation time (t_2). The first order quadrupolar interaction could be effectively removed with implementing multiple-quantum transition pulse sequence without changing MAS probe. The second order quadrupolar interaction could be, then, removed with allowing the spins to evolve in two time variables (i.e., MQ evolving time

and SQ relaxation time). The isotropic spectrum, of which the quadrupolar effects are removed, could be obtained in evolution time domain (t_1) with MQ pulse sequence.

(v) The calculation of NMR parameters

The various NMR parameters presented in this article could be calculated using these equations as below. These equations are referred from previous work. The chemical shift as peak maximum position in isotropic dimension (δ_{3QMAS}) and the center of gravity of the same peak in MAS dimension (δ_{MAS}) are correlated with this equation where the second order quadrupolar coupling product (δ_{iso}^{2Q}) is represented the quadrupolar coupling product (P_q). Furthermore, this quadrupolar coupling product is related with the quadrupolar coupling constant (C_q) which expressed with the atomic symmetry parameter (η) of target nuclear. And these equations are expressed with some parameters suchlike the quadrupolar moment (eQ), the principle component of the electric field gradient (eq), and the Larmor frequency (ω_0) of target nuclide.

$$\delta_{3QMAS} = -17/31 \delta_{iso}^{CS} + 10/31 \delta_{iso}^{2Q}, \quad \delta_{MAS} = \delta_{iso}^{CS} + \delta_{iso}^{2Q} \quad (1-6)$$

$$\delta_{iso}^{2Q} = -6000 \cdot \frac{P_q^2}{\omega_0^2} \left(\text{if spin} - \frac{5}{2} \right) \quad (1-7)$$

$$P_q = C_q \left(1 + \eta^2/3 \right)^{\frac{1}{2}} \quad (1-8)$$

$$C_q = \frac{e^2 q Q}{h} \quad (1-9)$$

$$\delta_{iso}^{CS} = -\frac{31}{27}\delta_{3QMAS} + \frac{10}{27}\delta_{MAS} = \dots = -\frac{31}{17}\delta_{3QMAS} + \frac{10}{17}\left[-6000 \cdot \frac{1}{\omega_0^2} \cdot e_{2qQh1+\eta23}\right] \quad (1-10)$$

$$\delta_{iso}^{2Q} = \frac{12}{27}\delta_{MAS} - \frac{31}{27}\delta_{3QMAS} \quad (1-11)$$

$$P_q = \sqrt{-\frac{\omega_0^2}{6000}(\delta_{MAS} - \delta_{iso}^{CS})} \quad (1-12)$$

1.2.3. Natures of Glasses and Melts

We had explored the quenched silicate glasses at high pressure, and many other previous studies also had worked with quenched glasses to elucidate the various properties of materials in liquid or molten phases. The quenched silicate glasses, however, does not have same physical and structural properties compared to silicate melts. The differences between silicate melts and quenched glasses have been being debated for a long time; however that have not been being clearly distinguished till now. The quenched silicate glasses are made from silicate melts by rapidly cooling the molten materials to prevent the formation of opaque crystals; therefore the quenched glasses are also called as super-cooled liquids[8, 9].

The quenched silicate glasses are commonly treated as an amorphous solid not liquids or melts because of their similar mechanical properties to solids with extremely high viscosity, which means that the flows of quenched glasses could not be observed in experimental research time scale. This high rigidity of quenched glasses is originated from the trapped translational and rotational degree of freedom in phase space indicating the reduced atomic mobility. On the other hand, sometimes the quenched glasses are classified into liquids because of their thermodynamic characteristics. The first-order thermodynamic variables such as volume, enthalpy, and entropy are continuously changed during the glass transition, whereas the second-order thermodynamic variables like thermal expansion coefficient and heat capacity are discontinuously changed during the glass

transition. These thermodynamic characteristics indicate the distinct phase transition of quenched glasses from common phase transition between solids and liquids. The quenched glasses are stable under glass transition temperature; however that could be transformed into more relaxed structure (i.e., similar to crystalline phase) because of their relatively lower activation energy of phase transition, showing the possibility of that the quenched glasses are local-table phase at relevant condition with lower activation barrier or meta-stable phase. Although the various thermodynamic properties of quenched glasses are changed from melts during the glass transition, we expect that the atomic configuration of melts is still remained in quenched glasses because the atomic configurations are trapped in their coordination during the rapid quenching of molten materials, and then, the structural information of quenched glasses allow us explore the atomic structural and macroscopic properties of silicate melts.

1.3. Results and Discussions

1.3.1. Experiments

Sample preparations

Two different types of aluminosilicate glasses were prepared; NAS150560, NAS150540 and NAS150520 were synthesized from the mixture of Na_2CO_3 , Al_2O_3 , and 40% ^{17}O enriched SiO_2 . 0.2 wt% of cobalt oxide (i.e., Cobalt (II) Oxide: CoO) was added for reducing the spin-lattice relaxation time. The details of synthesized samples are summarized in Table 1. The glass starting materials were synthesized at 1 atm by fusing the sample mixture for 1 hrs at 1473~1773 K in a Ar gas environment tube furnace, and were loaded into a multi-anvil press apparatus with a 10/5 and 18/11 (octahedron edge length/truncated edge lengths of the anvils) assembly. The samples were fused at 1923~2173 K for 20 minutes and quenched to glasses at a pressure range of 6 and 8 GPa; the initial quench rate was estimated to be larger than 50 °C. The sample has different SiO_2 molar fraction for each composition; hence their NBO/T (i.e., the number of non-bridging oxygen per tetrahedral cation, and reflects the extent of polymerization of silicate melts varying from 0, fully polymerized to 4, fully depolymerized) values are, also, different. Highly Na contained NAS150520 has 0.67, implying more depolymerized phase; and NAS150560 has 0.29 due to the higher SiO_2 molar fraction. All the samples are explored at 1 atm condition with NMR spectrometer; ex-situ experiments. The high

pressure NAS150540 samples are synthesized by Prof. Mibe at Tokyo University, Japan for 6 and 8 GP using multi-anvil press.

NMR spectroscopy

NMR spectra of ^{27}Al and ^{17}O were collected on a Varian Solid-State NMR 400 MHz spectrometer (9.4 T) where the Larmor frequency of each ^{27}Al and ^{17}O is 104.23 and 54.23 MHz. The Varian MAS 3.2 mm double resonance probe was used with ZrO_2 rotor, which was spun at 15 kHz for magic-angle spinning experiments. For each nuclide, ^{27}Al and ^{17}O , the almost same pulse sequence (experimental condition) was used to explore the system. In the 1D MAS experiments, relaxation delay was set to 1 s with 0.3 μs RF (i.e., radio frequency) pulse length; and then this pulse enhances 15 degree tip angle for the central transition in solid materials. After that, 2D 3QMAS spectra were collected with fast amplitude modulation shifted echo pulse which is represented with two hard pulses, duration were 3 μs and 0.6 μs , and one soft pulse, duration was 1 s.

1.3.2. Results

The ^{27}Al NMR results

The ^{27}Al 1D MAS and 2D 3QMAS spectra show the oxygen coordination number of each Al site indicating the changes of local atomic structure near the Al nucleus with increasing pressure and the topological disorder of the system.

The Figure 1 and Figure 2 are ^{27}Al 1D MAS and 2D 3QMAS spectra of Na-aluminosilicate glasses, showing that the proportions of highly coordinated Al (i.e., $^{[5,6]}\text{Al}$) increase with increasing pressure. The existence of $^{[5]}\text{Al}$, which does not exist in crystalline aluminosilicate polymorphs and indicates the evidence of amorphous nature of samples synthesized at high pressure [10].

The Figure 3 shows that the proportions of pressure-induced highly coordinated Al with increasing pressure, and those highly coordinated Al sites have relatively smaller proportions in NAS150520 (i.e., highly Na contained aluminosilicate glass). The Figure 4 shows this feature more clearly; the average coordination number of Al of NAS glasses at 6 GPa, which is obtained from product of proportion and coordination number of each coordinated Al site, decreases with increasing the content of Na in the system. The proportion of each coordinated Al site was scaled with their quadrupolar efficiency because the nucleus with different magnetic shielding has different quadrupolar excitation efficiency.

Furthermore, we could observe the changes in shape of peak and its region for ambient pressure samples in Figure 5 showing distorted off-Gaussian peak, even though the conventional isotropic projection should have Gaussian-like peak for each observed component [4]. This result could be presented more clearly in isotropic projection as Figure 6, and this distortion and broadening of spectrum is obviously more progressed in NAS150520 than that of NAS150560. This distortion appeared in NAS150520 may be caused from the local inhomogeneity around the Al sites implying the increases of configurational disorder, which is induced from the Na⁺ ion in the system. And the peak position shifting is, also, observed in NAS150520 due to the relatively long range interaction of Na cation field which reduces the magnetic shielding of Al nucleus (i.e., increasing the isotropic chemical shift of Al site).

The various NMR parameters calculated from 2D 3QMAS spectra provide more detailed structural changes with increasing pressure [10]. The isotropic chemical shift of each Al site is listed in Table 2, and this value of larger in NAS150520 than that of NAS150560 about 4~5 ppm implying the reduced magnetic shielding of Al by strong cation field of Na. Ant those isotropic chemical shift values increase with increasing pressure suggesting the decreasing inter-atomic distance between Na and Al. The quadrupolar coupling product (P_q) in Figure 7, which reflects the local distortion of electric field gradient (EFG; positive correlation with P_q) affecting to the

magnetic shielding of Al site, of each Al site increases with increasing pressure, and this could indicate the positive correlation between pressure-induced structural changes and distortion of EFG with changes of atomic arrangements around Al sites. The drops of P_q of Al in NAS150520 indicate the possibility of that the addition of network modifying cation (Na) would enhance the depolymerization of melts at high pressure, because the decreasing of P_q represents the increased bond angle and bond length of Al sites with increasing their symmetry, which means that the network modifying cation had the capability of reducing the pressure effect on polymerization of silicate melts.

The ^{17}O NMR results

Differently from ^{27}Al NMR data, the NMR spectra of ^{17}O provide the short-range chemical order of Na-aluminosilicate glasses such as oxygen linkage connected with cation (i.e., Si-O-Si, Al-O-Si, and Na-O-Si, etc.). The Figure 8 shows the ^{17}O 1D MAS spectra of Na-aluminosilicate with varying pressure, however this result could not be resolved to identify each oxygen linkages in sample. Even the pressure effects on the system could not be distinguished in 1D MAS spectrum, the compositional differences by Na contents are verified in -50~0 ppm region indicating the proportional difference of bridging oxygen (BO) and non-bridging oxygen (NBO). The Figure 9 is the collection of ^{17}O 2D MAS spectra for Na-aluminosilicate glasses providing more resolved spectral features of the oxygen linkages than that of 1D MAS data. The decreasing proportion of

NBO and increasing proportion of ${}^4\text{Si-O-}^{[5,6]}\text{Al}$ with increasing pressure presenting the expense of NBO for forming pressure-induced highly coordinated Al sites. And the Figure 10, the total isotropic projection of ${}^{17}\text{O}$ 2D 3QMAS spectra of Na-aluminosilicate glasses manifest the increasing proportion of ${}^4\text{Si-O-}^{[5,6]}\text{Al}$ with increasing pressure more dramatically than conventional ${}^{17}\text{O}$ 2D spectra. This polymerization process of oxygen linkage at high pressure could be illustrated as Figure 11; ${}^4\text{Si-O-}^{[4]}\text{Al} + \text{Na-O-}^{[4]}\text{Si} = {}^4\text{Si-O-}^{[5]}\text{Al} + \text{Na}^*$. Not only the pressure effect on NAS glasses but also the compositional differences of samples are more clearly shown in ${}^{17}\text{O}$ 2D 3QMAS spectra; the highly Na contained NAS150520 has more NBO (i.e., $\text{Na-O-}^{[4]}\text{Si}$), and the proportion of ${}^4\text{Si-O-}^{[4]}\text{Si}$ is relatively smaller than that of NAS150560. The Figure 12 and Table 3 show the proportion of relatively high energy cluster of NAS150520, ${}^4\text{Al-O-}^{[4]}\text{Al}$, which decreases apparently with increasing pressure implying that the chemical disorder may decrease with increasing pressure and correlated with forming ${}^4\text{Si-O-}^{[5,6]}\text{Al}$ linkages at high pressure [11].

The Figure 13 provides the quadrupolar coupling products (P_q) of ${}^{17}\text{O}$ in Na-aluminosilicate glasses with varying pressure. The P_q of ${}^4\text{Si-O-}^{[4]}\text{Si}$ decreases with increasing pressure in both samples implying the possibility of decreasing bond angle of this oxygen linkage in amorphous network system at high pressure as Figure 14. The previous NMR experiments and first-principle calculation results provide the negative correlation between asymmetry parameter of oxygen and bond angle in Si-O-Si linkage while the asymmetry parameter is negatively correlated with

P_q implying the P_q implying the positive correlation between Si-O-Si bond angle and P_q in amorphous network system (i.e., vitreous silica) [12, 13]. This result (i.e., decreasing P_q of Si-O-Si linkage with increasing pressure) could suggest the formation of more confined closed-ring like atomic clusters which could be one of the densification mechanisms of silicate melts at high pressure; and this intermediate order structural change of NAS glasses could contribute to the inert gas solubility in Earth's interior [14, 15]. The P_q value of $^{[4]}\text{Si-O-}^{[4]}\text{Al}$ show a small positive correlation with pressure implying the pressure-induced inter atomic length contraction and pressure-induced densification, and the $^{[4]}\text{Si-O-}^{[5,6]}\text{Al}$ linkage has relatively larger P_q values than that of $^{[4]}\text{Si-O-}^{[4]}\text{Al}$ since the atomic structure around the highly coordinated Al would be more distorted than that of $^{[4]}\text{Al}$ site. The definite correlation between P_q of Na connected oxygen linkage (i.e., Na-O- $^{[4]}\text{Si}$) and pressure is not observed in this result. Although the pressure effects observed in ^{17}O NMR results are shown in the calculated P_q values, the compositional effect on pressure-induced structural changes or chemical disorder could not be clearly observed. This result may provide the effect of Na ion on the pressure-induced densification in NAS glasses at high pressure with enhancing the depolymerization.

1.3.3. Discussions

In this work, we explore the Na-aluminosilicate glasses synthesized at high pressure varying chemical composition to elucidate the effect of network modifying cation on pressure-induced structural changes of silicate melts using ^{27}Al and ^{17}O 1D MAS and 2D 3QMAS NMR experiments. These NMR results of NAS glasses show the polymerization occurred with increasing pressure, while the network modifying cation (i.e., Na in this case) enhances the depolymerization of silicate glasses with its strong cation field. Hence, it means that the highly polymerized silicate melts at ambient pressure can facilitate the further polymerization of high pressure with expense of non-bridging oxygen. Relatively more depolymerized silicate glass, NAS150520, might have smaller topological entropy at high pressure than that of NAS150560 because the ^{27}Al and ^{17}O 2D 3QMAS spectra and estimated quadrupolar coupling product of Al provide the lower degree of polymerization of highly Na contained glass. There exists the strong correlation between the pressure-induced structural changes of silicate glasses and their local electronic environment such as electronic field gradient around the target nuclei (i.e., the Al and O); and the strong cation field of network modifying cation also affects to the local electronic environments. The calculated P_q values of Al and O provide that the local electronic environment could be affected by not only pressure-induced structural changes but also strong cation field of Na as indicated by the changing P_q values of Al. These results demonstrate that the

network modifying cation such as Na^+ could enhance the depolymerization of aluminosilicate glasses at high pressure with its strong cation field, and also imply that the higher degree of polymerization of aluminosilicate glasses at ambient pressure can facilitate the further polymerization of glasses at high pressure at the expense of NBO (non-bridging oxygen), which is one of the substantial densification mechanisms of silicate melts at high pressure.

These atomic structural investigations of Na-aluminosilicate glasses quenched at high pressure could suggest the valuable information about the geophysical and geochemical properties in Earth's deep interior [1, 14, 15]. Our experimental results acquired from solid-state NMR provide the valuable information of atomic configurations in amorphous network system of silicate glasses, and this obtained atomic structural information causes the macroscopic properties of Earth materials with showing their local atomic structure and electronic environments. In the next two paragraphs, the applications of geophysical and geochemical properties in Earth's interior will be discussed with their atomistic origins. We explored the very simple compositional sample whereas the real magmatic melts are multi-component silicate melts at high pressure and temperature affected by the various network modifying cations like Mg, Na, and Ca, etc..

In this study, we explored the relatively lower pressure region (~ 8 GPa) where the pressure dependence of Ar solubility has linear-like positive correlation. The ^{27}Al and ^{17}O NMR experimental results provide

various evidences of structural changes of silicate glasses in this lower pressure region. The existence of highly coordinated Al and increasing P_q of Al with increasing pressure indicate the pressure-induced polymerization and distortion of local atomic structure around Al, and the decreasing P_q of $^{[4]}\text{Si-O-}^{[4]}\text{Si}$ with increasing pressure suggest a decreasing Si-O-Si bond angle in silicate amorphous network. And these local atomic structural changes of silicate melts could suggest the circumstances of pressure effects on inert gas solubility with affecting to intermediate atomic structure of silicate melts such as forming confined closed-ring like clusters with expanse of non-bridging oxygen at high pressure. The further polymerization may occur at higher pressure region which show the dramatic breakdown of the amorphous network connections to denser atomic structure including oxygen tri-clusters in silicate melts structure [16]. And these polymerizations, as the main densification mechanism of silicate melts at high pressure, should be combined with equilibration of partial pressure of inert gas molecules to see the atomistic origins of anomalous features of pressure dependence of Ar gas solubility in silicate melts represented in Figure 15.

Table 1. The composition of prepared sample

Sample	Composition	NBO/T
NAS150520	$\text{Na}_2\text{O}:\text{Al}_2\text{O}_3:\text{SiO}_2 = 15:5:20$	0.67
NAS150540	$\text{Na}_2\text{O}:\text{Al}_2\text{O}_3:\text{SiO}_2 = 15:5:40$	0.40
NAS150560	$\text{Na}_2\text{O}:\text{Al}_2\text{O}_3:\text{SiO}_2 = 15:5:60$	0.29

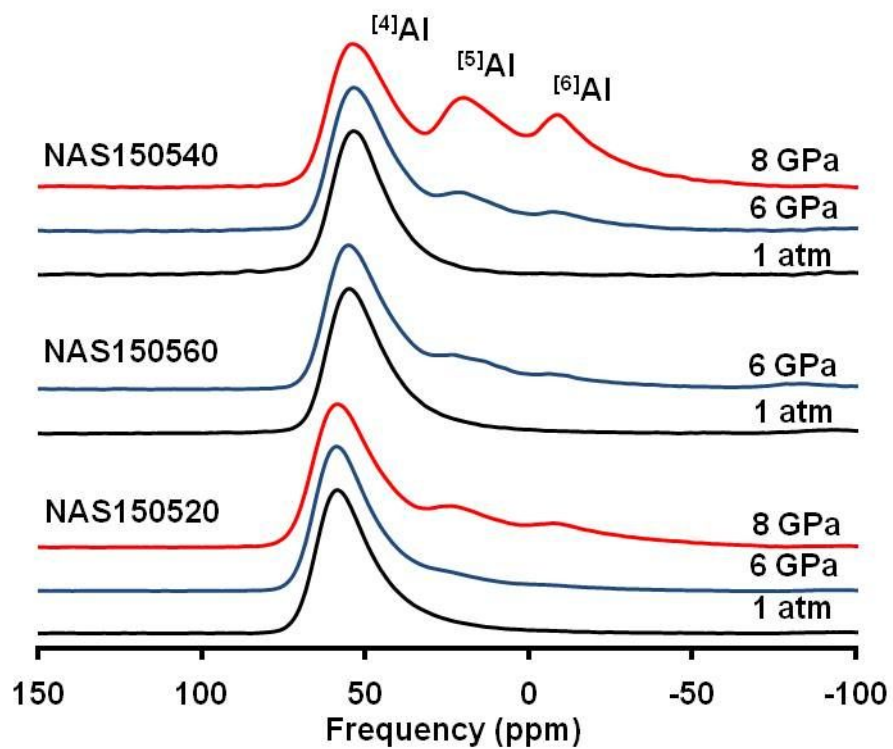


Figure 1. The ^{27}Al 1D MAS spectra of Na-aluminosilicate glasses with varying pressure

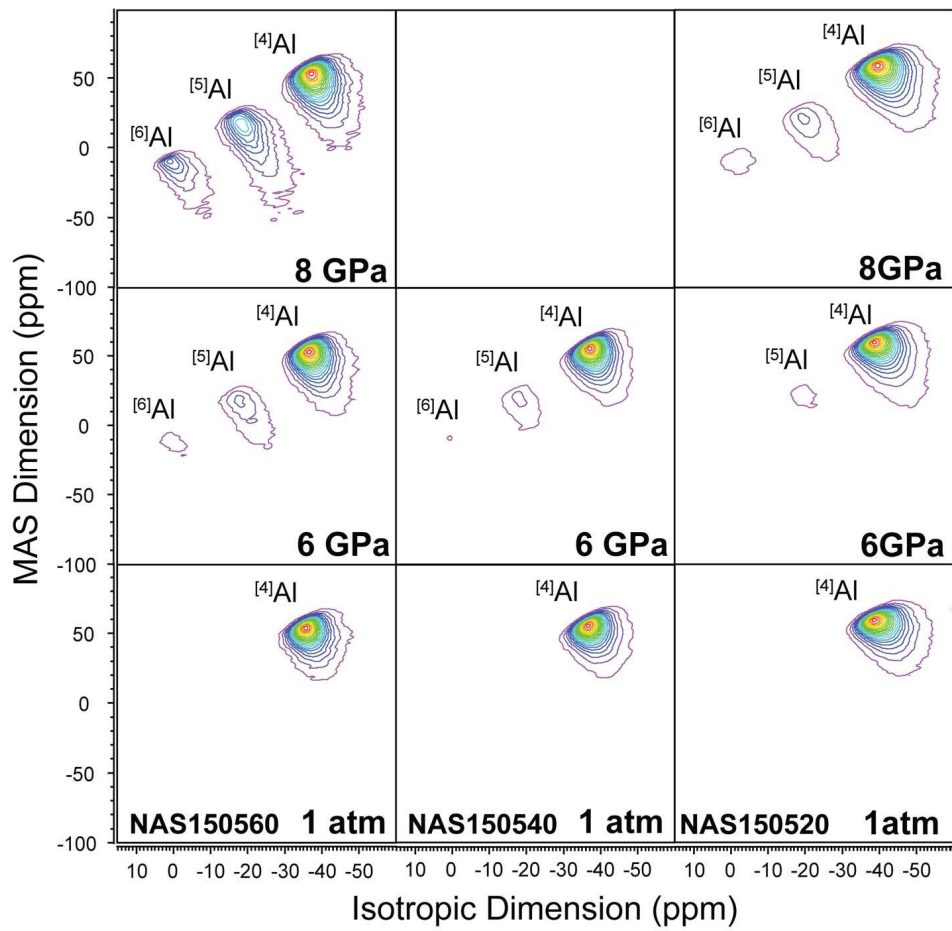


Figure 2. The ^{27}Al 2D 3QMAS spectra of Na-aluminosilicate glasses with varying pressure (total 20 contour lines are drawn from 4 to 98%)

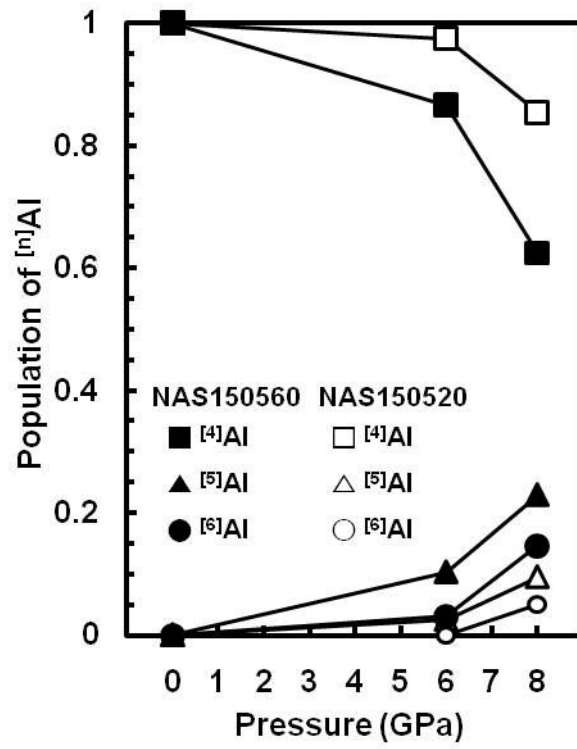


Figure 3. The proportion of each $[n]Al$ in Na-aluminosilicate glasses with varying pressure

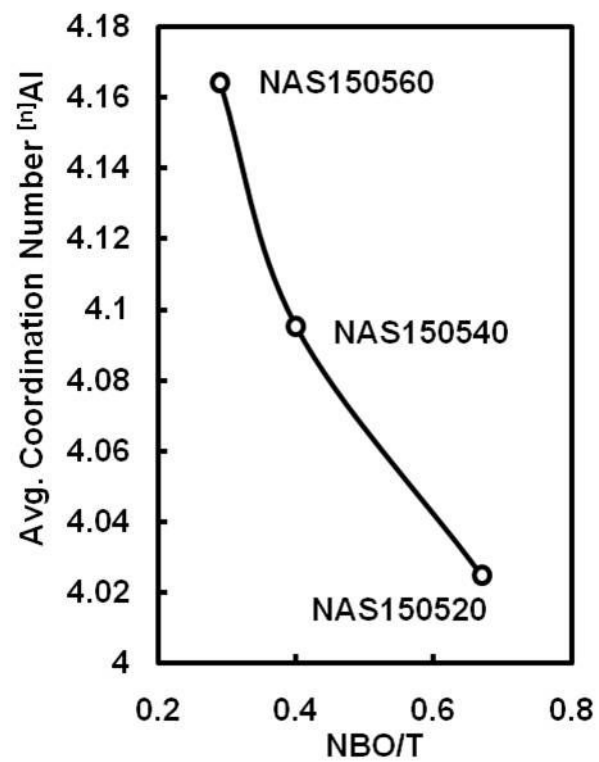


Figure 4. The average coordination number of Na-aluminosilicate glasses at 6 GPa

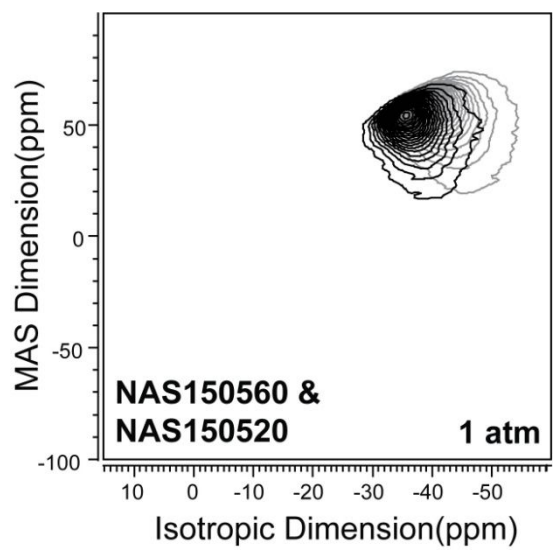


Figure 5. The overlapped ^{27}Al 2D 3QMAS spectra of Na-aluminosilicate glasses at ambient pressure

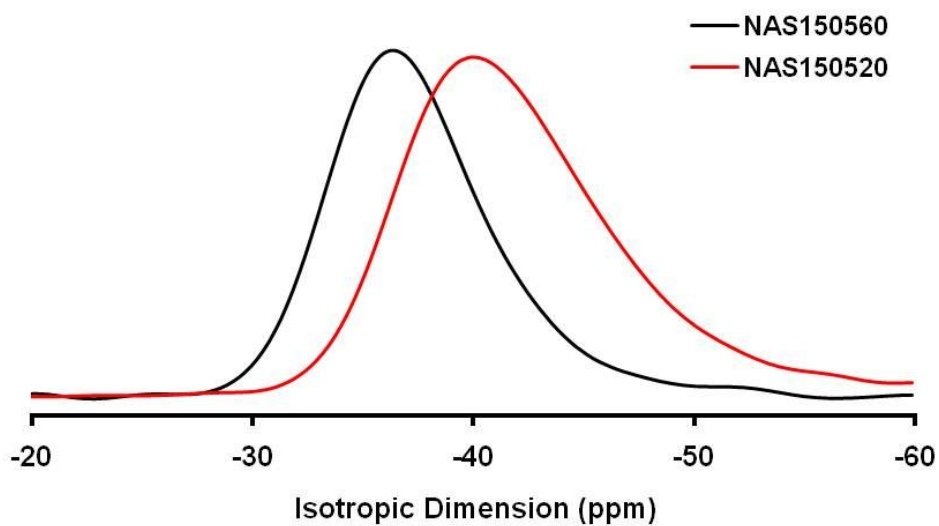


Figure 6. The isotropic projection of ^{27}Al 2D 3QMAS spectra of Na-aluminosilicate glasses at ambient pressure

Table 2. The isotropic chemical shift of ^{27}Al in Na-aluminosilicate glasses

		NAS150560			NAS150520		
Pressure		$^{\text{[4]Al}}$	$^{\text{[5]Al}}$	$^{\text{[6]Al}}$	$^{\text{[4]Al}}$	$^{\text{[5]Al}}$	$^{\text{[6]Al}}$
δ_{iso} (ppm)	1 atm	60.4±0.2			66.3±0.4		
	6 GPa	61.3±0.2	26.7±0.8	-2.2±6.7	66.6±0.2	30.8±4	
	8 GPa	62.0±0.1	27.3±0.4	-2.9±0.9	67.1±0.3	30.2±1	1.5±0.1

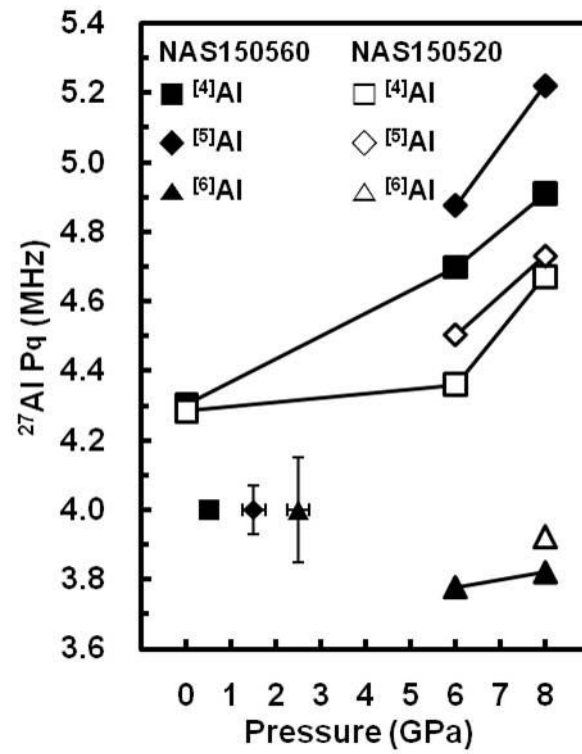


Figure 7. The quadrupolar coupling products (P_q) of ^{27}Al in Na-aluminosilicate glasses with varying pressure

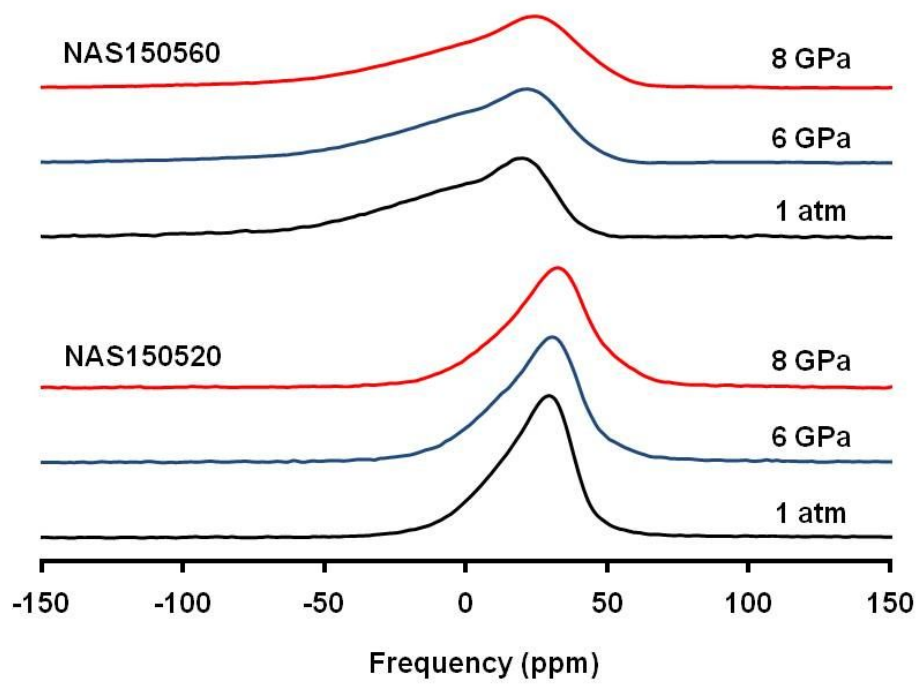


Figure 8. The ^{17}O 1D MAS spectra of Na-aluminosilicate glasses with varying pressure

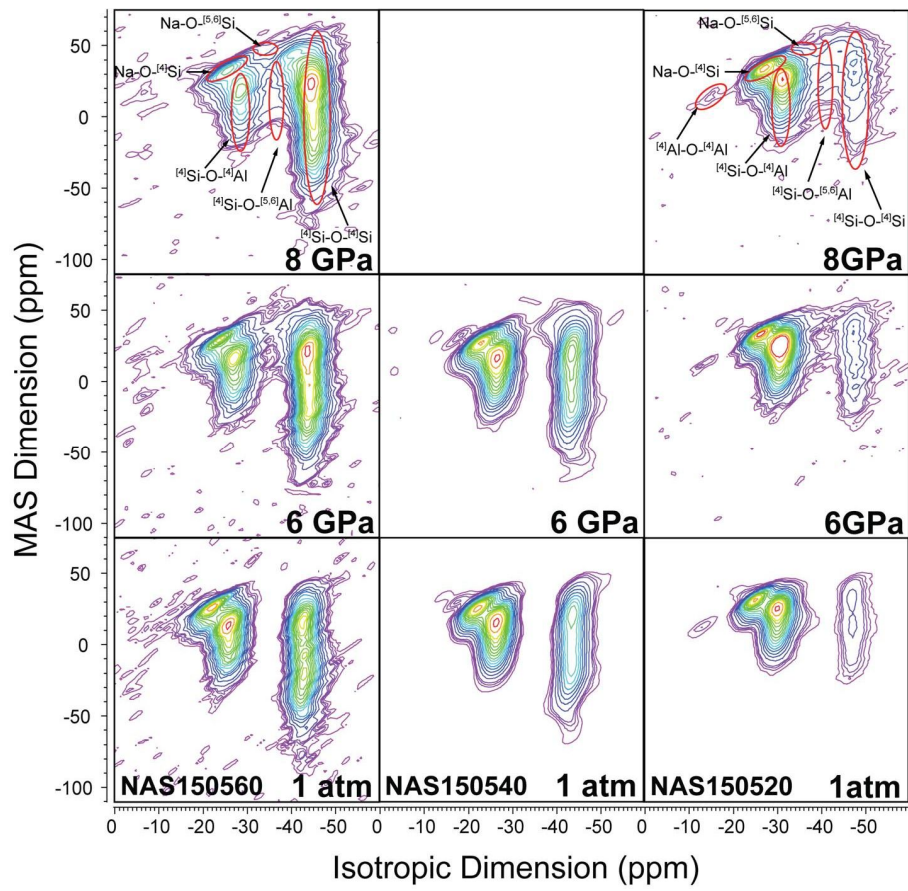


Figure 9. The ^{17}O 2D 3QMAS spectra of Na-aluminosilicate glasses with varying pressure (total 20 contour levels from 4 to 98%, added lines at 5 and 6.5%)

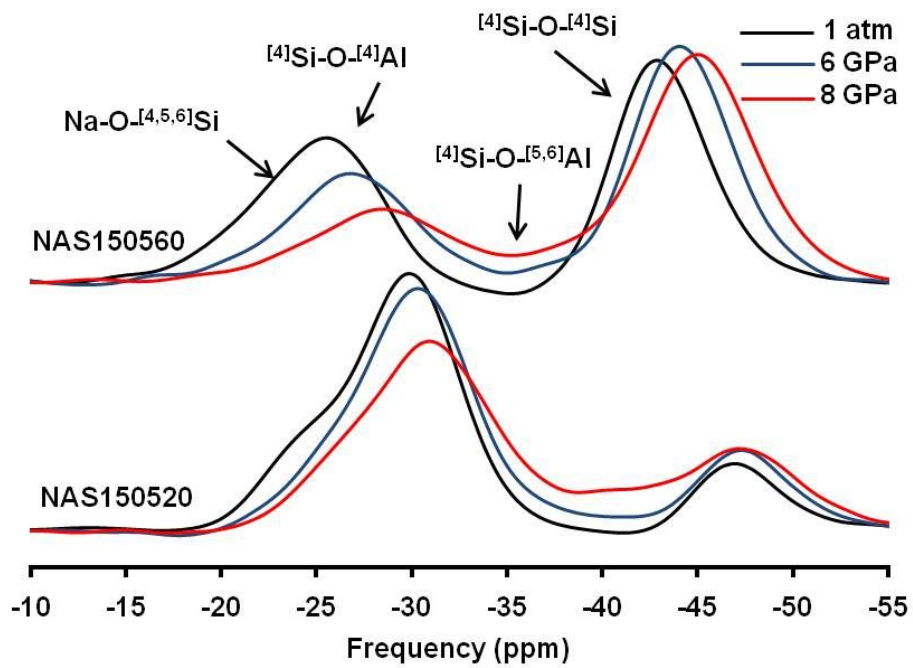


Figure 10. The isotropic projection of ^{17}O 2D 3QMAS spectra of Na-aluminosilicate glasses

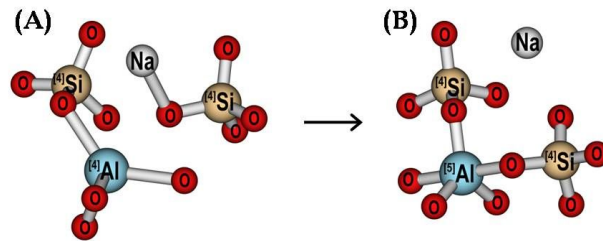


Figure 11. The schematic picture of atomic structure of polymerization process in Na-aluminosilicate glasses. (A) ${}^{[4]}\text{Si-O-}{}^{[4]}\text{Al} + \text{Na-O-}{}^{[4]}\text{Si}$. (B) ${}^{[4]}\text{Si-O-}{}^{[5]}\text{Al} + \text{Na}^*$

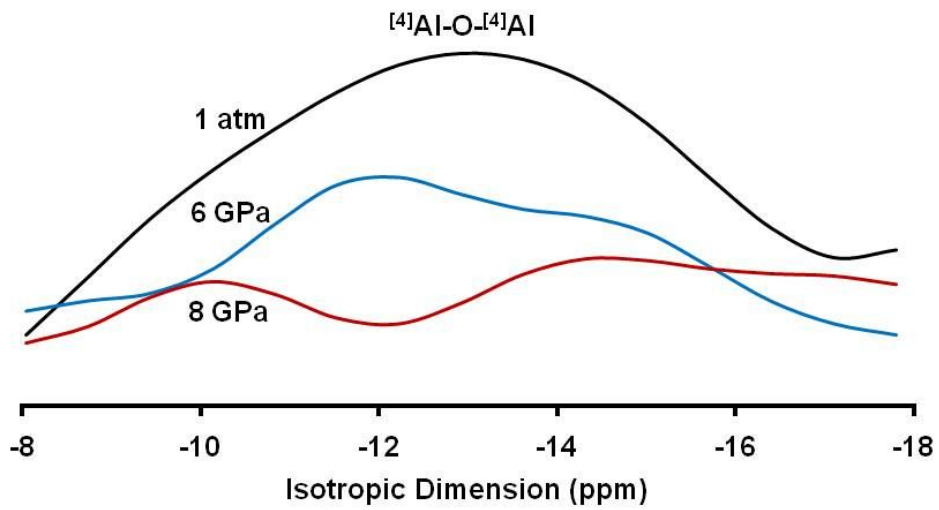


Figure 12. The proportion of $[^4\text{Al-O-}^4\text{Al}]$ high energy cluster in NAS150520 glasses with varying pressure

Table 3. The proportion of $^{27}\text{Al-O-}^{27}\text{Al}$ in NAS150520

Pressure	Total Intensity	$^{27}\text{Al-O-}^{27}\text{Al}$	Proportion
1 atm	16091	136	0.846%
6 GPa	9481	40	0.421%
8 GPa	10058	41	0.408%

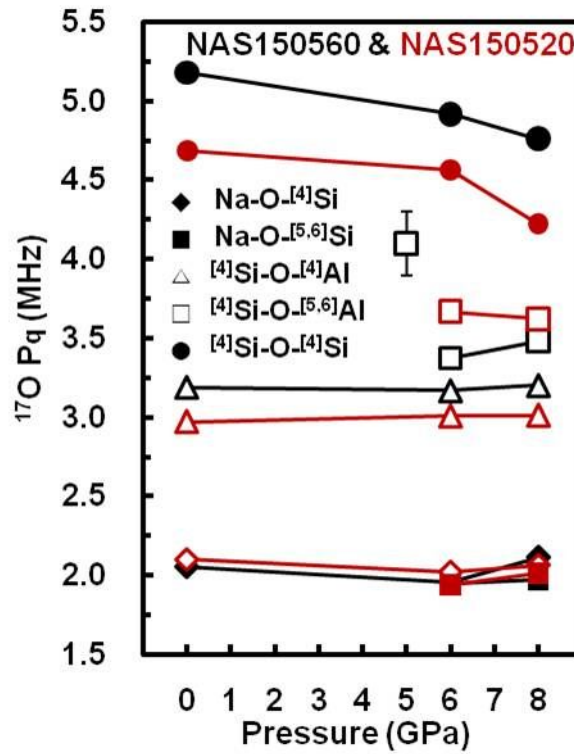


Figure 13. The quadrupolar coupling products (P_q) of ^{17}O in Na-aluminosilicate glasses with varying pressure (P_q values are estimated from its peak position except $^{4}\text{Si-O-}^{4}\text{Si}$ which is calculated from its center of gravity of peak.)

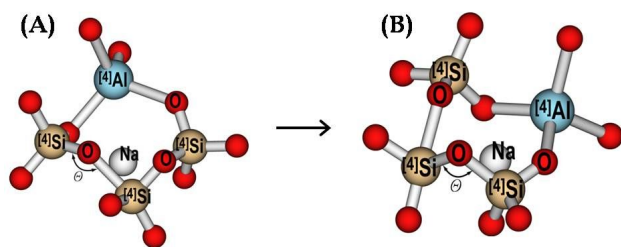


Figure 14. The schematic picture of atomic structure for decreasing $[4]\text{Si-O-[4]Si}$ bond angle

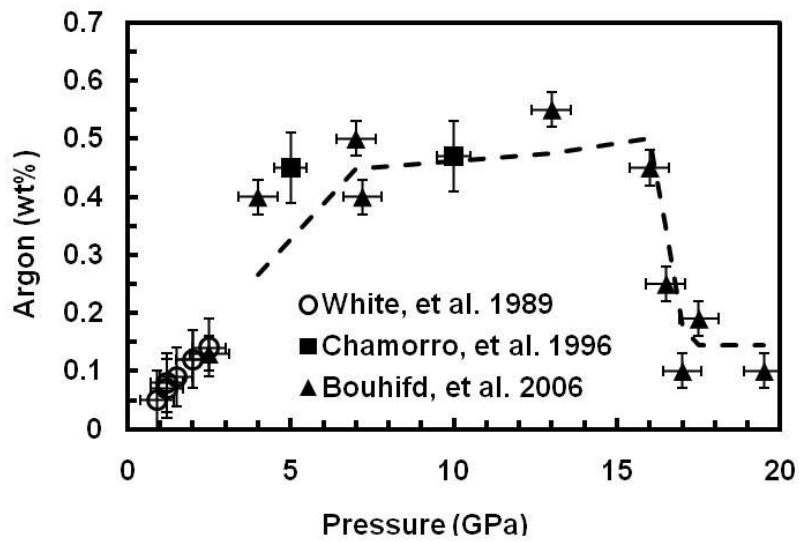


Figure 15. The pressure dependence of Ar gas solubility of Anorthite ($\text{CaAl}_2\text{Si}_2\text{O}_8$) glasses [15, 17, 18]

2. Theoretical Studies of the Local Electronic Environments of Oxygen in Mg-silicates at high pressure using ELNES (Energy-Loss Near-Edge Structure)

2.1. Introduction

Many experimentalists have been being suffered from the low possibilities and difficulties of experimental realization of high pressure and temperature condition relevant to Earth's deep inside, even though there were many recent advances of experimental apparatus and analyzing methods (i.e., diamond anvil cell, synchrotron x-ray experiments, etc.). The computational methods also called theoretical approaches, including first-principle calculations based on quantum theory, could be the solutions for overcoming the experimental difficulties to understand the material properties at extreme condition, because there are no limitations on reconstructing and controlling the surrounding environments of given system in interest [19-22]. And this theoretical approach could be used to explore the Earth's interior. Hence, we will investigate the local electronic environments of Mg-silicates with experimental and calculated results of non-resonant x-ray Raman scattering spectroscopy (XRS) in this section.

The Earth materials at high pressure, commonly silicate oxides, have not been well studied enough to understand the macroscopic

properties in amorphous and crystalline phases with high pressure in-situ XRS experiments, also in theoretical approaches, however there were many previous works done for exploring the crystalline semi-conductors and super-conducting materials. And the pressure-induced characteristic ELNES spectral features of crystalline and molten Earth materials are not well understood, too. Therefore, in this chapter, we will elucidate the pressure-induced oxygen K-edge ELNES spectral features of Mg-silicate glasses at high pressure obtained in previous work, comparing with the calculated ELNES spectra of crystalline Mg-silicates [16].

We had calculated the oxygen K-edge ELNES spectra of crystalline Mg-silicate and silicate polymorphs to use as the references of ELNES spectra of Mg-silicate glasses at high pressure: alpha-quartz, coesite, stishovite, pyroxene (ortho-enstatite), ilmenite, perovskite, and post-perovskite. And the calculated results of post-perovskite, of which the experiment is not realized due to its extremely high pressure stable field, could provide the reference of the future high pressure in-situ XRS experiments. The Mg-silicate, MgSiO_3 glasses and crystalline polymorphs, is one of the most abundant materials in Earth's mantle. The seismic explorations of Earth's interior already suggested the existence of Mg-silicate melts near the core-mantle boundary showing seismic heterogeneity. However, the atomistic origins of Mg-silicate melts and its macroscopic physical properties are still not understood well enough. Hence, we had worked on Mg-silicate glasses at high pressure with oxygen K-edge XRS spectra to investigate its local electronic structure. The

atomistic changes of Mg-silicate glasses at high pressure forming denser atomic configurations like oxygen tri-clusters could affect its thermodynamic and transport properties near the CMB. And this denser atomic configuration, also, affect the crystal-melt partitioning coefficient of lowermost mantle with reducing the permeable free volume of Mg-silicate melts.

2.2. Theoretical Backgrounds

Quantum mechanics based calculations are commonly called the ab-initio or first-principle methods. And this theoretical approach has lots of terms that should be considered in calculation, thus some of interacting terms are treated with approximation (or eliminated) for effective calculation. The conventionally used approximation methods are the DFT with pseudopotential approximation, DFT with augmented plane-wave set, and band structure formalism; from these methods, we used the DFT with augmented plane-wave set method. The common first-principle based methods represent the coefficient of electronic orbital wave-function with a matrix, and calculate the proper electron distribution (or electron configuration) using self-consistent field (SCF) method for the system in interest. We will summarize the well known approximation methods, pseudopotential approximation and APW based methods, with the flow of SCF calculation which are used in this work for calculating ELNES spectra of crystalline Mg-silicate and silicate polymorphs.

2.2.1. Principles of Non-Resonant X-ray Raman Scattering Spectroscopy

The non-resonant x-ray Raman scattering spectroscopy, also called as inelastic x-ray scattering spectroscopy, provides same information to conventional x-ray absorption spectroscopy (XAS). And this XAS measures

the x-ray absorption coefficient of incident photon (i.e., x-ray light source) including both XANES and EXAFS energy region. These two regions are distinguished from their detection energy from the absorption edge of target atom; the XANES, as its name, start ~ 5 eV from the absorption edge to ~ 50 eV, thus the absorption features of this region are induced from the multiple scattering of photoelectron excited at absorption site because of its low kinetic energy level, reflecting the chemical bonding structure and local electronic environments (i.e., sensitive in determining the average oxidation state and coordination environment of absorption site). Differently from the XANES, the wave length of backscattered photoelectron is shorter than inter-atomic distance in the EXAFS region (i.e., the higher energy region than that of XANES, from 50 eV beyond the ionization energy), thus the single scattering events become dominant and provide the local structure around absorbing site in materials and oscillation features showing the final state interference effect (i.e., The backscattered photoelectron waves interfere with the forward-propagating waves. And this interference causes the modulation of the measured absorption coefficient, causing the oscillation called the final state interference effect.).

The oxygen K-edge ELNES spectral features shows the oxygen proximity in Mg-silicate amorphous and crystalline system, and then this fact could be used in analyzing the experimental results of Mg-silicate glasses with calculated results of crystalline Mg-silicate [23-25]. We have been being tried to investigate the oxygen K-edge XRS spectral features

similar to XANES (X-ray Absorption Near-Edge Structure) region of XAS (X-ray Absorption Spectroscopy), which is also called as ELNES (Energy Loss Near-Edge Structure) spectrum, using first-principle calculations for crystalline Mg-silicate. This oxygen K-edge ELNES spectrum could provide the valuable information of atomic structure around the oxygen atom as XANES, sensitive in chemical bonding structure and local electronic environments with multiple scattering of incident photon [25]. And this multiple scattering of incident photon was used in previous theoretical approaches of ELNES spectrum, however this method lose its accuracy considering the high atomic number elements [26]. Hence, the other methodologies are used to simulate the ELNES spectral features; the density functional theory (DFT) with pseudopotential approximation, augmented plane-wave based methods, and band structure formalism, etc. [6, 27, 28]. This first-principle based theoretical approach of oxygen K-edge ELNES spectrum of MgSiO_3 and SiO_2 crystalline polymorphs would provide the advanced intuitions for analyzing the characteristic spectral features of experimental results. And we also expect that this full first-principle analysis of electronic structure of silicate oxides could shed light on the further insights of experimentally un-probed electronic origins of non-resonant x-ray Raman scattering spectral features of Earth materials at high pressure.

(i) The fundamental equations of x-ray absorption spectroscopy

The absorption coefficient (χ), which is correlated with the intensity changes of incident and transmitted x-ray, could be calculated from the dipole transition moments of electron induced by incident x-ray. The forward-propagating wave function from absorption site as a spherical wave propagates until reach neighboring atoms, and the backscattered wave induced due to this propagating wave. Then this backscattered wave interferes with forward-propagating atoms. This interference has, therefore, fine structure information near the absorption site of the system. We could investigate this fine structure using not only classical multiple scattering method but also quantum based calculation. The simple concept used in quantum based theory to calculate x-ray absorption fine structure is briefly explained. Also the fundamental EXAFS equation to give details of fine structure information is presented.

$$\mu(E) \propto |\langle f | \hat{H} | i \rangle|^2 \quad (2-1)$$

$$\hat{H} = \frac{1}{2m} \left(\vec{p} + \frac{e}{c} \vec{A} \right)^2 + V(\vec{r}) = \hat{H}_0 + \hat{H}_{int} \quad (2-2)$$

$$\hat{H}_{int} \propto \frac{e}{mc} \vec{A} \cdot \vec{p} \quad (2-3)$$

$$\hat{H}_0 = \frac{1}{2m} \vec{p}^2 + V(\vec{r}) \quad (2-4)$$

$$A_\mu = \sum_k \sum_{\alpha=1}^2 \epsilon_\mu^{(\alpha)} \left(a_{k,\alpha}(t) e^{i\vec{k} \cdot \vec{e}} + a_{k,\alpha}^\dagger(t) e^{i\vec{k} \cdot \vec{e}} \right) \quad (2-5)$$

$$\vec{B} = \nabla \times \vec{A} \quad (2-6)$$

$$|f\rangle = |f_0\rangle + |\Delta f\rangle \quad (2-7)$$

$$\mu(E) \propto \mu_0 [1 + \chi(E)] \quad (2-8)$$

$$\chi(E) \propto \langle \Delta f | \hat{H}_{int} | i \rangle \quad (2-9)$$

Here, μ indicates the transition dipole moment; A is vector potential or four vector used in classical electromagnetism or quantum field theory to formulate the Hamiltonian operator for the radiation field (i.e. products of polarization, creator and annihilating operators). The final state is separated into two parts, one is for the free electron final state and the other is for the effect of placing the atom near the absorption site (i.e. alteration due to neighboring atoms near the absorption site). This extra part of final state wave function illustrates the local fine structure around the absorption site. The details about this method are still being studied. On the other hand, the absorption coefficient could be easily calculated using multiple scattering methods considering thermal vibration of atoms and inelastic scattering effects.

$$\chi_i(\mathbf{k}) = \sum_j N_j S_i^2(\mathbf{k}) F_j(\mathbf{k}) e^{-2\delta_j^2 k^2} \cdot \exp\left\{-\frac{2r_j}{\lambda_j(\mathbf{k})}\right\} \cdot \frac{\sin(2\mathbf{k}r_j + \phi_{ij}(\mathbf{k}))}{kr_j^2} \quad (2-10)$$

Here, the approximated spherical wave function is using a spherical Bessel function; the thermal vibration (δ_j) similar to the Debye-Waller factor (i.e., The Debye-Waller factor describes the reduction amplitude of scattered x-ray owing to a thermal vibration of atoms in condensed matter system.) is considered with Gaussian distribution; the phase shift (ϕ_{ij}) and amplitude changes (F_j) during scattering is, also,

considered; the two parameters, amplitude reduction factor (S_i) and decreasing of the signal due to inelastic mean free path (λ_j), are included.

(ii) The double diffraction scattering cross section (DDSCS)

Even the experimental XRS results provide the almost same information to XAS, the actual physical processes occurred in sample during XRS experiments are different from that of XAS. The other property, called double-diffraction scattering cross section (DDSCS), is used to describe the proper inelastic scattering process of absorption site. The DDSCS shows the excitation probability of the absorption site from initial (k_i) to final (k_f) state by absorbing kinetic energy from incident photon, and the definition of DDSCS, which is the number of scattered electrons per energy unit as a function of energy loss E , could be simplified with the dynamic form factor, $S(q, E)$.

$$\frac{\partial^2 \sigma}{\partial E \partial \Omega} = 4 \left(\frac{e_0}{q} \right)^4 m_e^2 \frac{k_f}{k_i} \cdot S(\vec{q}, E) \quad (2-11)$$

$$S(\vec{q}, E) = \sum_{kv, nlm} |\langle \vec{k}_v | e^{i \vec{q} \cdot \vec{r}} | nlm \rangle|^2 \delta(E + E_{nlm} - E_{kv}) \quad (2-12)$$

The differential electron current (σ), induced from excitation of photoelectron of absorption site, is positively correlated with the transition probability (\mathbf{W}) as follows.

$$d\sigma = \sum_{i,f} \frac{(2\pi)^3 m_e}{\hbar k_i} dW_{if} \quad (2-13)$$

$$dW_{if} = \frac{2\pi}{\hbar} |\langle f|V|i\rangle|^2 \cdot d\mathbf{v}_f \cdot \delta(\mathbf{E}_i - \mathbf{E}_f) \quad (2-14)$$

$$d\mathbf{v}_f = \frac{2m_e}{2\hbar} \mathbf{k}_f \cdot d\mathbf{E} d\Omega \quad (2-15)$$

Finally, the transition probability could be calculated from the dynamic form factor (i.e., including the crystal symmetry incident and scattered electron wave vector and transition energy difference information), and we could simulate the ELNES spectrum of absorption site in interest [29].

2.2.2. Principles of the First-Principle Calculation Methods

There are various approximation methods of first-principle calculation to calculate the inter-atomic interactions more effectively. The electron-electron interactions, major time consuming part in calculation, are approximated by treating electron distributions as density functional called DFT (density functional theory). And the minor complex part, the electron-ion (or electron-nuclei) interaction, could be simplified with pseudopotential method [6, 19, 20]. The latest and advanced approximation method for crystalline system does not approximate the electron-ion interaction using pseudopotential; this method uses the augmented plane-wave function as the basis set of electron wave function [28].

(i) Fundamentals of DFT

The Kohn-Sham energy functional approach

The many-body electron system could be represented by spatial distribution of electron gas with the exchange and correlation energy which describe the unique functional form of the given electronic system. The minimum of total energy functional provides the ground state of the system; and the electron density, which yields this energy configuration, is the exact ground state of electronic density (i.e., the singularity of the ground system). The simplified total energy functional of Kohn-Sham

approximation method, which describes the set of doubly occupied electron states (ψ_i), could be expressed with these equations. The minimum energy of this functional form provides the ground state energy of the electronic system with ions at position (\mathbf{R}_I). The total energy functional is represented with combination of various physical properties such as the Coulomb energy associated with interactions among the nuclei or ions at position (\mathbf{R}_I), the state total electron-ion potential (V_{ion}), the electron density (n), the static potential (V_{ee}) induced from the electron-electron interaction, and the exchange-correlation functional (E_{XC}).

$$E[\{\psi_i\}] = 2 \sum_i \int \psi_i \left(-\frac{\hbar^2}{2m} \right) \nabla^2 \psi_i d\tau + \int V_{ion}(\vec{r}) n(\vec{r}) d\tau + V_{ee} + E_{XC}[n(\vec{r})] + E_{ion}(\{\mathbb{R}_I\}) \quad (2-16)$$

$$n(\vec{r}) = 2 \sum_i |\psi_i(\vec{r})|^2 \quad (2-17)$$

$$V_{ee} = \frac{e^2}{2} \int \frac{n(\vec{r})n(\vec{r}')}{|\vec{r}-\vec{r}'|} d\tau d\tau' \quad (2-18)$$

BO and CP approximation methods

The Born-Oppenheimer (BO) method, which is an approximation method used in computational quantum chemistry to explore the energy and wave function of the molecule. In this approximation method, the wave function of a molecule is separated into two parts, its electronic term and nuclear term because the nuclear mass is heavier than electron about 1,000 times. Then the energy of electron is treated as not correlated with nuclear motion that means the electron moves in another frame fixed at nuclear. However, the another approximation method, Car-Parrinello (CP),

is natural density functional theory based approximation using local density approximation (LDA) and pseudo potential method. This CP method has higher accuracy than BO method which is the limiting case of CP method.

The exchange and correlation energy

The exchange energy is induced from the reduced Coulomb energy of the electron because of the anti-symmetric property of electron wave function (i.e., the electron has half-integer spin number known as fermion). And this effective pseudo energy makes spatial separation of electron and reduces the Coulomb energy. The origin of correlation energy is the difference between the many-body interaction and the energy of system could be calculated with the Hartree-Fock (HF) approximation method.

Pseudopotential approximation (electron-ion interaction)

In the core region, the wave functions of the electrons oscillate rapidly because of the tightly bound core orbital and this strong ionic potential could be replaced with pseudo potential function which is identical at outside the core region. Also the rapidly oscillated wave function is replaced with pseudo wave function that needs relatively small number of basis function than the real wave function because each wave and potential function is designated having no radial node inside the core region. Furthermore, these rapidly oscillated wave and potential functions

are correspond with orthogonality between the wave function of valence electron and core electron. Each discrete energy state of valence electron augments, increasing its number, near the core region because of the strong ionic potential of nuclei. Therefore, defining the adequate pseudo potential function decreases the enormous number of plane-wave basis state which is induced from region of rapidly oscillated function near the core.

(ii) Fundamentals of APW based methods

The APW, LAPW, and DFT

The theoretical approaching method used in this work is specialized for calculating electronic properties of the crystalline system which has long range periodicity. The plane wave (PW) is a common basis set for calculating the DFT equations for the electron wave functions in crystalline system. The PWs are, however, inefficient basis set for describing the rapidly oscillating wave functions near the core region of the atomic system. Therefore there have been being developed many approximation methods to avoid this inefficient natural basis set of electron wave function. The first one is pseudopotential approximation method which replaces the original potential function with simplified potential function. The other method is called augmented plane wave based methods used in this work [29-35].

Augmented plane-wave (APW) basis set

In the APW method, the wave functions in a crystal system are expressed in terms of spherical harmonics and radial functions around of each atom, and of plane waves between the atoms. In the LAPW method, the energy dependence of each radial wave function (used as basis function of wave function) in the atomic sphere region is linearized by taking a linear combination of energy value and its energy derivative which is computed at the same energy. The unit cell is partitioned into two regions, the first one (I) is the sphere centered on the all constituent atomic site position (r) with its radius (R), and then second region (II) is remaining interstitial region. The wave functions are expanded into plane waves (PWs), each of what is augmented by atomic solutions in the form of partial waves (i.e. the product of a radial function and spherical harmonics). The Kohn-Sham orbital (ψ_i) is expressed as a linear combination of APWs basis function (ϕ_k). The KS orbital is extended to non-linear eigenvalue problem by choosing inadequate value of initial energy of the system. In a consequence, the initial trial value of energy for SCF calculation should be selected from calculation results of solving the energy secular equation ($|H-ES|=0$).

$$\psi_k = \sum_n C_n \phi_{k_n} \quad (2-19)$$

$$\phi_K(r) = \begin{cases} \sum_L \alpha_L^{\alpha K} u_L^\alpha(r', \epsilon) Y_L(r'), & r' < R_\alpha \\ \Omega^{-\frac{1}{2}} \exp[i \cdot (k + K) \cdot r], & r \in I \end{cases} \quad (2-20)$$

Full potential + Linearized augmented plane-wave (LAPW) basis set

In this method, the spatial energy dependence of each radial wave function in the atomic sphere region is linearized with taking a linear combination not only the energy at fixed position but also its position derivative. The solutions of the KS equation are expanded according to the variational method which allows us to approximate the ground state energy of a system using trial variation function made from LAPW basis function without solving Schrödinger equation. The various properties of electronic system like crystal potential, charge density, and forces acting on the atoms could be calculated relatively efficiently than using APW method only, because the efficient optimization of structural parameters is possible by taking spatial energy dependence on each radial wave function.

$$\phi_K(\mathbf{r}) = \begin{cases} \sum_L [a_L^{\alpha K} u_L^\alpha(\mathbf{r}') + b_L^{\alpha K} \dot{u}_L^\alpha(\mathbf{r}')] Y_L(\hat{\mathbf{r}}'), & r' < R_\alpha \\ \Omega^{-\frac{1}{2}} \cdot \exp[i(\mathbf{k} + \mathbf{K}) \cdot \mathbf{r}], & r \in I \end{cases} \quad (2-21)$$

$$\frac{\langle \phi^* | \hat{H} | \phi \rangle}{\langle \phi^* | \phi \rangle} \geq E_1 \quad (2-22)$$

Augmented plane-wave + Local orbital (LAPW+lo) basis set

The theoretical method used in this work separates the energy state of electron into three types; core, semi-core, and valence state. In the core state, the charge is entirely confined inside the corresponding atomic sphere. And the energetically highest occupied state, valence state, always has a significant amount of charge outside the atomic sphere. The intermediate energy state, semi-core state, is high enough energy and in this regime charge is no longer completely confined inside the atomic

sphere but has few percents outside the atomic sphere. This semi-core state is not easy to describe using APW method or LAPW because of a definite spatial separation of atomic sphere region in wave function. Therefore, the concept of local orbital introduced to approximate the semi-core energy state more efficiently. The basis set of APW+lo method is analogous to that of original APW method. However the local orbital term is added with the continuity condition at the atomic sphere boundary and makes the faster convergence than LAPW method.

$$\phi_{lo}(\mathbf{r}) = \begin{cases} [a_L^{\alpha,lo} \mathbf{u}_l^\alpha(\mathbf{r}') + b_L^{\alpha,lo} \dot{\mathbf{u}}_l^\alpha(\mathbf{r}')] Y_L(\hat{\mathbf{r}}'), & r' < R_\alpha \\ \mathbf{0}, & \mathbf{r} \in I \end{cases} \quad (2-23)$$

2.3. Results and Discussions

2.3.1. Experiments and Calculations

Experiments

All of the experimental oxygen K-edge XRS results used here were obtained in previous work of 'X-ray Raman scattering of MgSiO₃ glass at high pressure' [16]. The details of sample synthesis methods and experimental conditions are summarized in that paper. They used Mg-silicate oxide materials in both amorphous and crystalline phases to explore the local electronic environment of MgSiO₃ glass at high pressure with in-situ experiments. And this oxygen K-edge ELNES spectra of MgSiO₃ glass at high pressure were compared with that of crystalline MgSiO₃ and SiO₂ polymorphs to distinguish characteristic spectral features of MgSiO₃ glass at high pressure. The used crystalline SiO₂ sample was alpha-quartz, and MgSiO₃ samples were pyroxene (ortho-enstatite), ilmenite, and perovskite.

Calculations

We had used the LAPW based program package called Wien2k to calculate the oxygen K-edge ELNES spectra of crystalline SiO₂ and MgSiO₃ polymorphs [36]. The selected crystalline SiO₂ polymorphs were alpha-quartz, coesite, stishovite; and MgSiO₃ polymorphs were pyroxene, ilmenite, perovskite, and post perovskite. The atomic structures of these crystals were referred from previous XRD experimental results listed in

Table 4. And the Figure 16 shows the atomic structures of calculated SiO₂ and MgSiO₃ crystals, the structure optimization for given structure did not perform in the whole calculation. The crystal structures are visualized and edited using Visualization for Electronic and STructural Analysis (VESTA) program [37]. The oxygen K-edge ELNES spectra and partial density of states (p-DOS) were calculated for those selected crystalline Earth materials.

The proper electronic configuration (i.e., optimized electronic orbital distribution) should be calculated as a preparatory step to calculate the oxygen p-DOS and oxygen K-edge ELNES spectra of crystalline SiO₂ and MgSiO₃ polymorphs. And the SCF calculation should be used in this process. The appropriate parameters for SCF cycle are chosen as follows. The Muffin-Tin radii (R_{MT}) for Mg, Si, and O determined by program were 1.79, 1.59, and 1.59 Å, whereas the real atomic radii of atoms are 1.6, 1.18, and 0.78 Å. The cut off energy of separation of core and valence state is chosen to -7.1 Ry for more accurate calculation, because the default value (-6.0 Ry) makes the p-orbital of silicon treated as core electron. And the Perdew-Burke-Ernzerhof 96 (i.e., PBE-96, one of the common generalized gradient approximation methods) is chosen as exchange-correlation approximation method. The RK_{MAX} , which limits the number of coefficient of electron wave function for atoms with R_{MT} , was set to 5.0. Conventionally, this value is set to 2.3~ for hydrogen atom, 5.0~ for s- and p- orbital elements, and 6.0~ for f-orbital elements (O - 1s² 2s² 2p⁴, Si - [Ne] 3s² 3p², Mg - [Ne] 3s²). The G_{MAX} value, which determines the magnitude of largest vector in Fourier expansion of charge density, is set to 12.0.

Conventional G_{MAX} value for GGA method is 14.0, however the relatively smaller value is sufficient to calculate proper electronic configuration in simple atomic system (i.e., merely s- and p-orbital in valence states). The number of k-point is set 30~50 with considering each cell size of SiO_2 and MgSiO_3 polymorph. The 100~1,000 k-points for 1 atom/cell is sufficient to calculate insulators such as silicate oxides, and the size of k-mesh generated from the number of k-point could be reduced with increasing the number of atoms in unit cell by a factor N (i.e., N atoms/cell). The convergence criteria of SCF calculation were total energy and charge fluctuation; energy as 0.0001 Ry and charge as 0.0001 e.

The oxygen K-edge ELNES spectra are calculated with relevant program module. Some parameters should be chosen to calculate proper spectra. The absorption edge of oxygen is set to 538.25 eV (i.e., the electron binding energy of 1s orbital) and energy grid is set to 0-35 eV. The detector collection semi-angle and microscope convergence semi-angle are 5.0 and 1.87 mrad as default values, and the dipole approximation mode is selected for a detector angle independent calculation. The edge offset of valence broadening is set above the end of energy grid and the Gaussian broadening factors of spectrometer are 0.0, 0.5, and 1.5. The Gaussian broadening factor, induced from an instrumental broadening, is selected to represent the most relevant ELNES spectrum to experimental results. After this ELNES calculations, the p-DOSs of oxygen were calculated to analyze the XRS spectral features more specifically. The XAS and XRS spectral features are induced from the relevant occupied orbitals; thus the

calculated p-DOS could reflect the characteristic XRS spectral features. The calculated density of states were total DOS, and p-DOS of s- and p-orbital including directional dependence of p-orbital for oxygen. The Gaussian broadening factors for p-DOS calculations were 0.0, 0.003, and 0.04. Furthermore, the electronic excitation of 1s-orbital in oxygen atom, called the core-hole effect, is considered for non-resonant x-ray Raman scattering and DOS calculation. Hence, the electronic configuration of target oxygen is modified in an appropriate way (i.e., the single core electron in 1s-orbital is removed and the additional electronic charge is added in valence shell.).

2.3.2. Results

Experiments (the oxygen K-edge XRS spectroscopy)

The oxygen K-edge XRS spectra were collected in APS and SPring-8 for alpha-quartz and MgSiO₃ crystalline polymorphs. All of the experimental results of selected crystals are listed in Figure 17 with relevant calculated oxygen K-edge ELNES spectra. The result of alpha-quartz shows the characteristic spectral features as following; the intense peak around 538 eV, small bump at ≈545 eV, and broad peak beyond ≈550 eV. The result of ilmenite shows the distinct spectral features from other MgSiO₃ polymorphs; the well separated two peak maxima are appeared in ≈535~545 eV regions with broad peak beyond ≈550 eV. The spectrum of pyroxene could not provide clear spectral features as that of ilmenite; the broad peak with small intensity fluctuation at ≈530~540 eV, small bump

near 547 eV, and broad peak beyond 550 eV. The spectrum of perovskite shows the intense and broad peak $\approx 535\sim 545$ eV with peak like small feature ≈ 547 eV, and broad peak beyond 550 eV. However, it is difficult to conclude that the small features ≈ 547 eV as peak because the signal-to-noise ratio of this spectrum is not good enough to distinguish such small features. The spectra of MgSiO_3 glasses with varying pressure from ambient pressure to ≈ 39 GPa show the significant peak shifting and little broadening.

Calculations

All of the calculated oxygen K-edge ELNES spectra and p-DOS are compared with the experimental XRS results. These two calculated results could predict the XRS experimental results with further insights for analyzing local electronic environments of sample. The chosen crystalline SiO_2 polymorphs are alpha-quartz, coesite, and stishovite; and the MgSiO_3 polymorphs are pyroxene, ilmenite, perovskite, and post-perovskite. The calculated results are summarized in this section.

Alpha-quartz and coesite. The calculated oxygen K-edge ELNES spectrum of alpha-quartz shows the consistent results with experimental results. The ELNES calculation reproduces the broad peak ≈ 540 eV and small bump ≈ 545 eV regions. The p-DOS of oxygen shows that the broad and intense peak of ELNES spectrum is mainly originated from p-orbital excitation of oxygen and the part of broad peak beyond 550 eV is arisen from d-orbital

of oxygen [Figure 18]. The alpha-quartz is constructed by tetrahedral SiO_4 units with corner-sharing oxygen, and this characteristic structure induces the spectral shape of calculated oxygen K-edge ELNES spectrum. The similar spectral features are arisen in coesite which is constructed by SiO_4 with corner-sharing oxygen having different arrangement [Figure 19].

Stishovite. Not only the coesite but also higher pressure stable phase stishovite is calculated as other SiO_2 polymorphs, and the calculated ELNES spectrum and p-DOS show the distinct spectral features because the stishovite is constructed with octahedral SiO_6 units with edge-sharing oxygen [Figure 20]. The two intense and broad peaks are observed at ≈ 537 and ≈ 542 eV regions with broad peak beyond 550 eV, and this calculated result shows good agreement with previous experimental and calculated results [24]. The calculated oxygen p-DOS of stishovite provides the detailed electronic origins of calculated ELNES spectrum; the each directional component of p-orbital (i.e., PX, PY, and PZ) reflects the lattice arrangements of SiO_6 unit. Thus, the p-DOS of stishovite shows different features from that of alpha-quartz and coesite, which have relatively randomly oriented frame units than stishovite. These distinct spectral features of stishovite might be originated from its edge-sharing oxygen configuration, indicating closer oxygen proximity to its second nearest neighboring oxygen [16, 24, 38]. And these calculated results of SiO_2 polymorphs would be helpful to elucidate the ELNES spectra of MgSiO_3 polymorphs.

Pyroxene. We calculated the oxygen K-edge ELNES spectra and p-DOS for crystalline MgSiO_3 polymorphs same as the case of SiO_2 polymorphs. The calculated pyroxene was ortho-enstatite, and this structure has distinct crystal site; epical site, and corner-sharing and not-connected oxygen at planar site. Hence, each of sites is calculated and averaged with its proportion to compare with experimental results, while the experimental result of pyroxene shows similar spectral features to alpha-quartz originated from its SiO_4 tetrahedral unit connected with corner-sharing oxygen. The intense peak of pyroxene is appeared at ≈ 540 eV with broader peak width than that of alpha-quartz [Figure 21], indicating the larger bond angle of Si-O-Si stemmed from the cation effect of Mg and its atomic configuration [16]. The result of each crystallographic site of pyroxene provides the distinct spectral features; the corner-sharing oxygen site shows the well known alpha-quartz like spectral features, and other components show distinct spectral features.

Ilmenite. The oxygen K-edge XRS spectrum of ilmenite shows peculiar spectral features differently from pyroxene, with two peak maxima $\approx 535\sim 545$ eV and broad peak beyond 550 eV. And the calculated ELNES spectrum of ilmenite shows consistent result with experimental result [Figure 22]. These two peak maxima in main peak at ≈ 540 eV might be originated from the edge-sharing oxygen of SiO_6 octahedral as stishovite. And the p-DOS of each directional component in p-orbital shows the distinct shape due to their horizontal alignment of octahedral sites.

Perovskite. The experimental result of perovskite could not provide clear spectral features as stishovite or ilmenite. The calculated oxygen K-edge ELNES spectrum of perovskite is similar to experimental results even the resolution of spectrum is not enough to distinguish detailed spectral features due to its low signal-to-noise ratio; the intense and broad peak appears at $\approx 535\sim 545$ eV and broad peak beyond 550 eV [Figure 23]. And the small peak like feature appears at ≈ 552 eV in experimental results (i.e., even it is difficult to conclude this feature is signal due to the low signal-to-noise ratio) in both experimental and calculated results. The results of p-DOS show that the oxygen K-edge ELNES spectrum of perovskite is also mainly come from the oxygen p-orbital excitation. These calculated results of perovskite do not show the distinct spectral features $\approx 535\sim 545$ eV like stishovite or ilmenite because all of the SiO_6 octahedral sites of perovskite are connected with corner-sharing oxygen.

Post-perovskite. The ELNES spectrum and p-DOS of the higher pressure stable phase than perovskite, post-perovskite, are calculated to distinguish the changes of spectral features during the Pv-pPv phase transition [Figure 24]. The well aligned octahedral SiO_6 units of post-perovskite are connected with both corner-sharing and edge-sharing oxygen, and each calculated result of distinct crystallographic site shows different spectral features each other. The absorption edge of oxygen in post-perovskite is shifted to higher energy than that of perovskite with a small peak width broadening.

2.3.3. Discussion

Nowadays, the non-resonant x-ray Raman scattering spectroscopy is one of the most effective structural probes for exploring the local electronic structure of both crystalline and amorphous materials at extremely high pressure and temperature, although there are still remaining problems to distinguish the system having similar spectral features with local electronic environments. However, this problem could be solved by collecting spectra with changing target elements, and using first-principle calculations to analyze the atomistic origins of spectral features. Hence, in this work, the oxygen K-edge ELNES spectra of crystalline SiO_2 and MgSiO_3 polymorphs were calculated using LAPW based method to analyze the oxygen K-edge XRS experimental results of MgSiO_3 glasses at high pressure. And the calculated results of crystalline system show the characteristic spectral feature for corner-sharing and edge-sharing oxygen, having different oxygen proximity to its second nearest neighboring oxygen.

In the SiO_2 polymorph system, the differences between corner-sharing oxygen of SiO_4 tetrahedral site and edge-sharing oxygen of SiO_6 octahedral site are clearly observed with broader absorption threshold expanded to higher energy region. However, the MgSiO_3 polymorphs show different results because of the network modifying cation in the system. The ilmenite, which has edge-sharing oxygen with octahedral sites, shows similar spectral features to that of stishovite with more overlapped

two main peaks. And the perovskite, which is constructed with corner-sharing oxygen of SiO_6 octahedral sites, shows different spectrum to ilmenite of which the connection way of oxygen is edge-sharing. The post-perovskite, higher pressure stable phase of perovskite, shows the distinct calculated ELNES spectrum to that of perovskite with increasing absorption edge and peak maximum because of rearrangement of SiO_6 units at high pressure. All of these experimental and related calculation results of oxygen K-edge ELNES spectra show that the connections of oxygen, corner-sharing and edge-sharing of frame units, is reflected in corresponding ELNES spectra.

The Figure 25 shows the oxygen K-edge XRS spectra of MgSiO_3 glasses with varying pressure from 1 atm to 39 GPa with significant pressure dependence of spectral features, and the calculated ELNES spectra of perovskite and post-perovskite are also listed showing shifted absorption edge and peak maximum to higher energy region about 5 eV showing similar trend of changing spectrum to that of MgSiO_3 glasses at high pressure [16]. The previous NMR experiments for MgSiO_3 glasses at high pressure show the increasing proportion of highly coordinated Si with increasing pressure [39]. The oxygen K-edge ELNES spectra, which reflect the local electronic bonding structure of oxygen, of perovskite and post-perovskite provide the similar trend and a magnitude of changes of spectral feature (≈ 5 eV) to that of MgSiO_3 glasses at high pressure, where the differences of spectral features between perovskite and post-perovskite are induced from closer oxygen proximity in post-perovskite with

rearrangement of SiO_6 octahedral units (i.e., particularly, a corner-sharing oxygen, $^{\text{[6]}\text{Si-O-}^{\text{[6]}\text{Si}}$, in perovskite leads to a oxygen K-edge features around 540 eV while a edge-sharing oxygen, $^{\text{[6]}\text{Si-O-2}^{\text{[6]}\text{Si}}$, in post-perovskite results in features around 545 eV.). Since, the edge-sharing oxygen of SiO_6 octahedral sites in MgSiO_3 post-perovskite has similar atomic configuration to that of oxygen tri-clusters (i.e., oxygen coordinated by three highly coordinated Si atoms) indicating the closer oxygen proximity to next nearest neighboring oxygen than that of corner-sharing oxygen, these current results could imply that the previous assignment of the ≈ 545 eV features as oxygen tri-clusters in Mg-silicate glass at high pressure about 20 GPa is likely to be correct. This structural change of MgSiO_3 glasses at high pressure, also, could affect to the changes of intermediate atomic configuration not only local electronic bonding structures [16].

3. Conclusion

The presented results of solid-state NMR experiments and first-principle calculations of silicates provide the local atomic structure and electronic environments around the target nucleus. The NMR experiments of Na-aluminosilicate glasses provide the effect of network modifying cation on structural changes of sample glasses synthesized at high pressure as a precursor of the silicate melts in Earth's interior above 400 km (~15 GPa). And the non-resonant x-ray Raman scattering experiments for oxygen K-edge of MgSiO₃ glasses at high pressure and relevant calculated ELNES spectra of MgSiO₃ crystalline polymorphs show the pressure effect on local electronic environments of oxygen in MgSiO₃ glasses at high pressure as a precursor of upper mantle above 1000 km (~40 GPa), and used for predicting the atomic configuration of MgSiO₃ melts at higher pressure near the core-mantle boundary condition. These local atomic structure and electronic environments could provide the advanced understanding of transport properties of silicate melts at high pressure and their essential roles on evolution of Earth's system. Because, the dynamic of fluid in Earth's interior, mantle convection, is one of the most important factors causing the evolution of stratified layers and heat transport of Earth's interior [40]. The changes of transport properties caused from the pressure-induced atomic structural changes and its compositional effects are as follows. The diverse evidences of strong correlation between the viscosity and atomic configuration have been being studied in many

previous works. They suggested that the pressure-induced structural changes cause a polymerization of silicate melts, increasing proportions of bridging oxygen and increasing viscosity of which is correlated with the activation barrier of atomic mobility [41, 42].

These presented results could provide the valuable information about not only transport properties but also chemical properties such as elements partitioning and inert gas solubility, and so on. The inert gas solubility which could be one of the structural probes of silicate melts at high pressure and is a primary key of solving the origins of atmosphere of terrestrial planet for exploring the processes of inert gas elements sequestration in Earth's interior with stratified layer during cooling of the magma ocean [14, 17, 43]. The recent experimental results show the anomalous Ar gas solubility versus pressure as Figure 15, incompatible with common sense of the gas solubility of liquid which should increase with increasing pressure because the inert gas elements near the surface boundary move to melts to equilibrate the chemical potential [14, 15, 17, 18]. This anomalous feature of Ar gas solubility at high pressure might be originated from atomic configuration of silicate melts distinguished from its chemical equilibration because the significant atomic structural changes of silicate melts occurred at high pressure change the permeable free volume of Ar gas molecule in silicate melts. And the rapid drop of Ar gas solubility would be caused from the breakdown of silicate melts structure with forming oxygen tri-cluster like configuration. Furthermore, this structural change of silicate melts also could affect to the elements

partitioning between melts and crystal in mantle similar to the case of inert gas solubility with varying the proportion of bridging oxygen [16, 44].

Table 4. The crystallographic information of SiO₂ and MgSiO₃ polymorphs

Crystal	Composition	Lattice Parameter						
		Space Group	a (Å)	b (Å)	c (Å)	α	β	γ
<i>a</i> -quartz ⁽¹⁾	SiO ₂	(152) P3121	4.921	4.921	5.404	90	90	120
Coesite ⁽²⁾	SiO ₂	(15) C2/c	7.136	12.369	7.174	90	120.34	90
Stishovite ⁽³⁾	SiO ₂	(136) P42/mnm	4.18	4.18	2.668	90	90	90
Ilmenite ⁽⁴⁾	MgSiO ₃	(148) R -3	4.728	4.728	13.559	90	90	120
Ortho-enstatite ⁽⁵⁾	MgSiO ₃	(61) Pbc _a	18.225	8.813	5.18	90	90	90
Perovskite ⁽⁶⁾	MgSiO ₃	(62) Pbnm	4.775	4.929	8.897	90	90	90
Post-perovskite ⁽⁷⁾	MgSiO ₃	(63) Cmcm	2.456	8.042	6.093	90	90	90

(1) 2x2x1 super cell (36 atoms), Glinneman et al., Z Kristallogr, 1992 [45]

(2) 2x1x1 super cell (56 atoms), Levien et al., Am. Mineralogist, 1981 [46]

(3) 2x2x1 super cell (48 atoms), Ross et al., Am. Mineralogist, 1983 [47]

(4) 2x1x1 super cell (60 atoms), Horiuchi et al., Am. Mineralogist, 1987 [48]

(5) 1x1x1 single cell (80 atoms), Ohashi, Phys. Chem. Minerals, 1984 [49]

(6) 2x2x1 super cell (80 atoms), Horiuchi et al., Am. Mineralogist, 1987 [48]

(7) 1x1x1 single cell (80 atoms), Murakami et al., Science, Vol. 304, p. 855, 2004 [50]

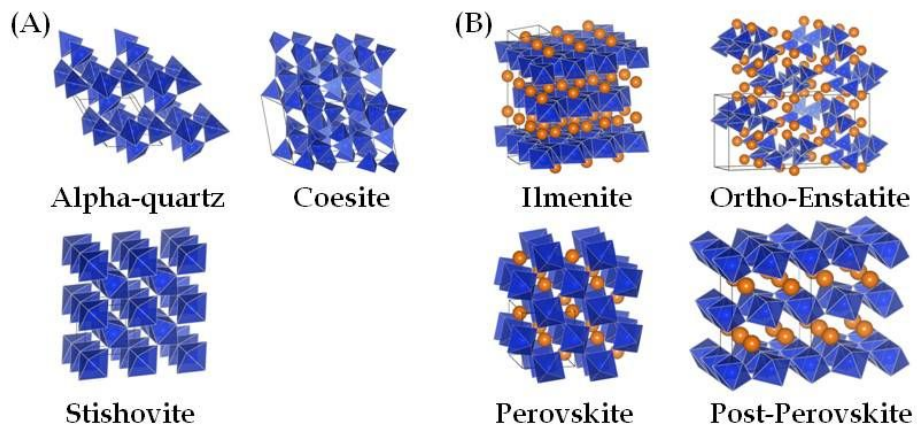


Figure 16. The crystal structures of SiO_2 and MgSiO_3 polymorphs. (A) the crystalline SiO_2 polymorphs; alpha-quartz, coesite, stishovite. (B) the crystalline MgSiO_3 polymorphs; ilmenite, ortho-enstatite (pyroxene), perovskite, post-perovskite

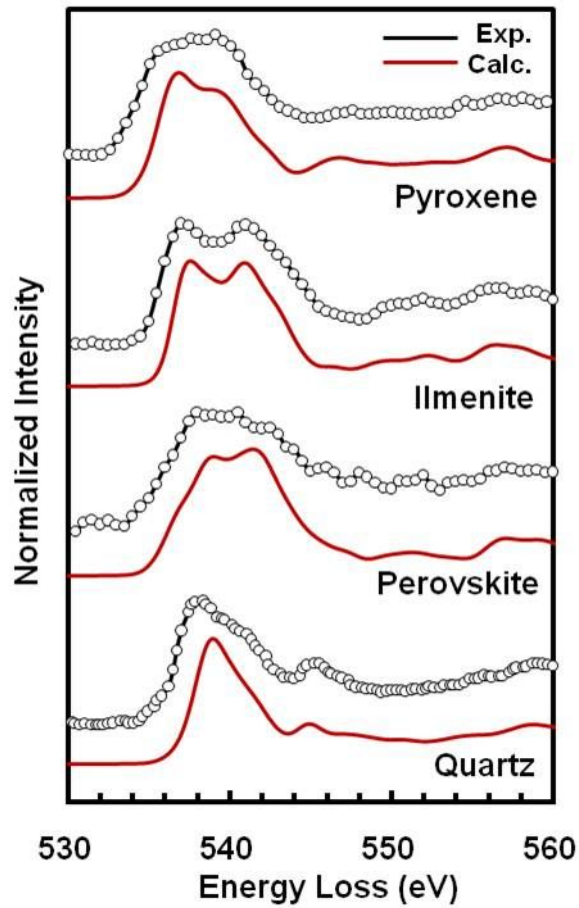


Figure 17. The oxygen K-edge experimental XRS and calculated ELNES spectra of alpha-quartz and crystalline MgSiO_3 polymorphs

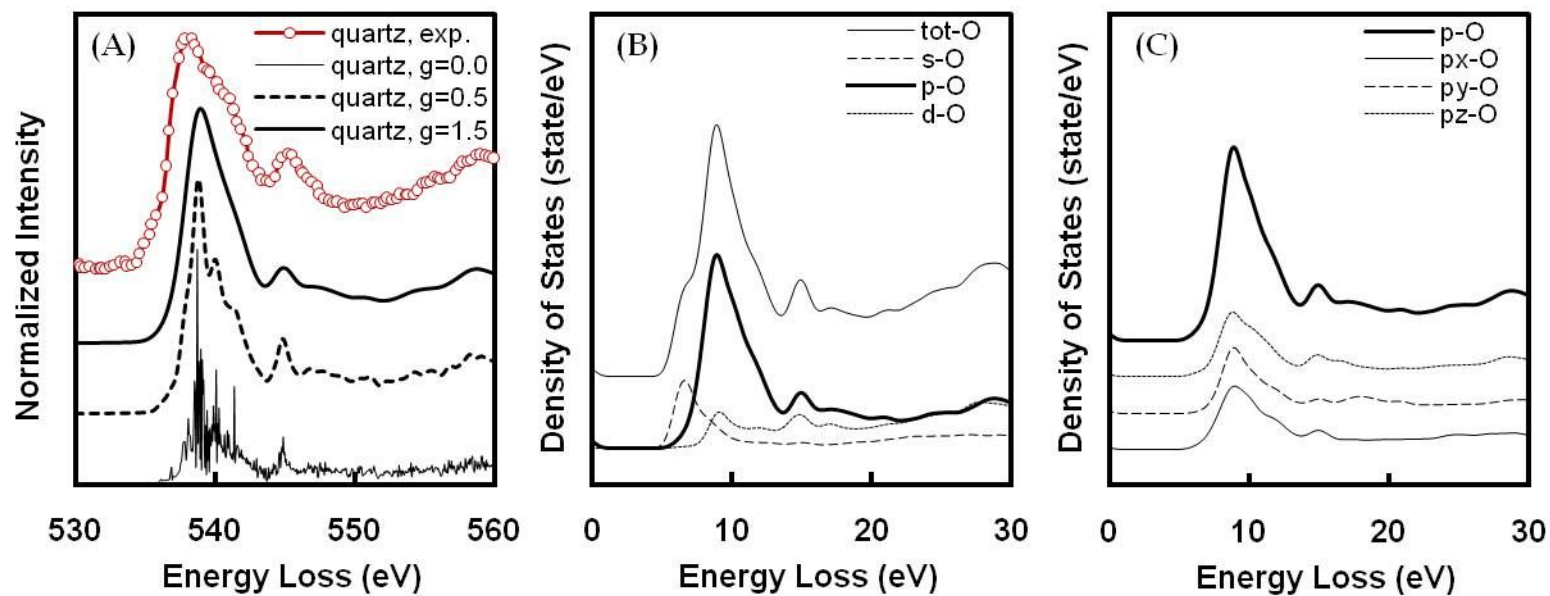


Figure 18. The calculated and experimental results of SiO₂ alpha-quartz. (A) the oxygen K-edge ELNES spectra. (B) the partial density of states (p-DOS) of oxygen. (C) the directional components in p-orbital of oxygen.

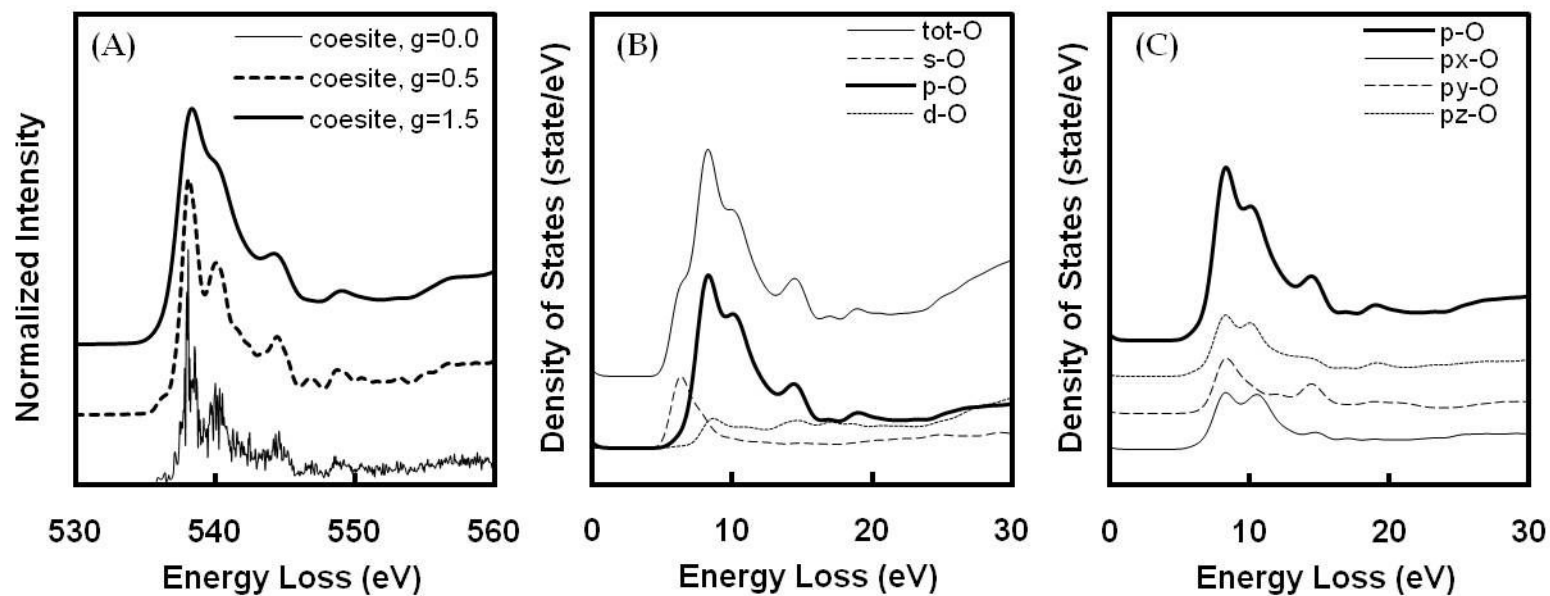


Figure 19. The calculated results of SiO₂ coesite. (A) the oxygen K-edge ELNES spectra. (B) the partial density of states of oxygen. (C) the directional components in p-orbital of oxygen.

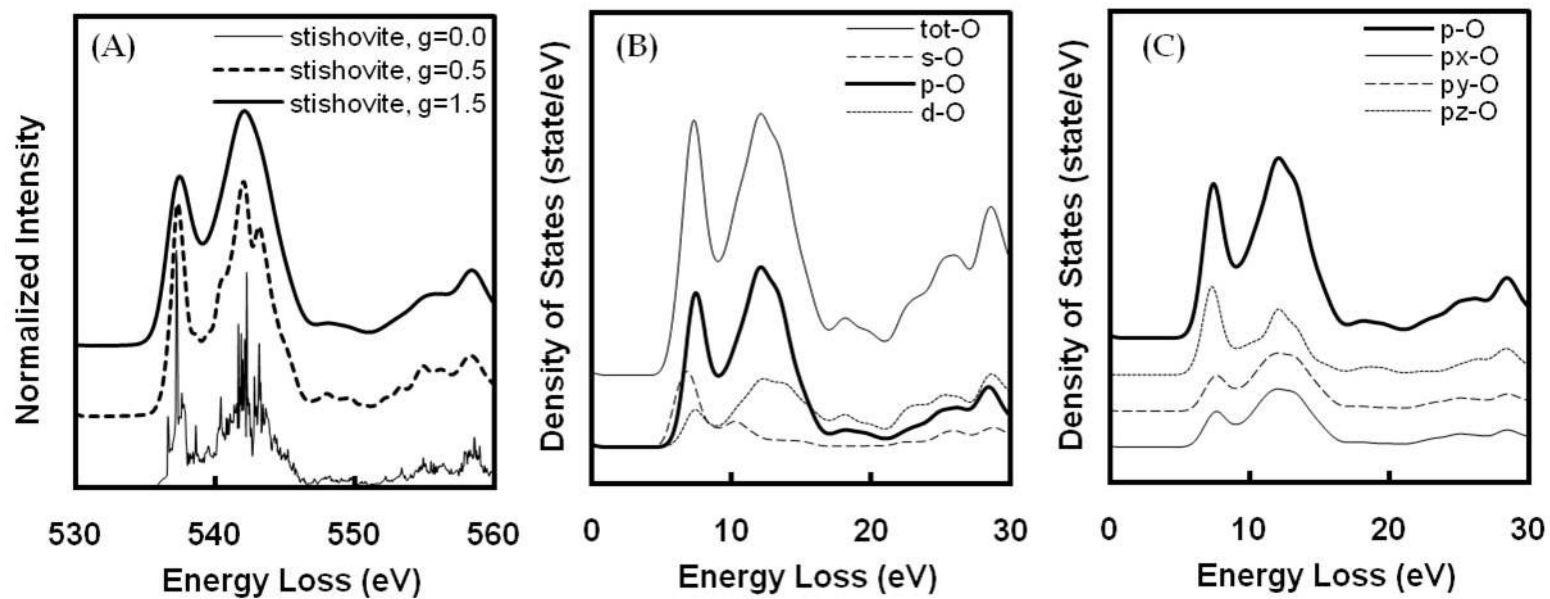


Figure 20. The calculated results of SiO₂ stishovite. (A) the oxygen K-edge ELNES spectra. (B) the partial density of states of oxygen. (C) the directional components in p-orbital of oxygen.

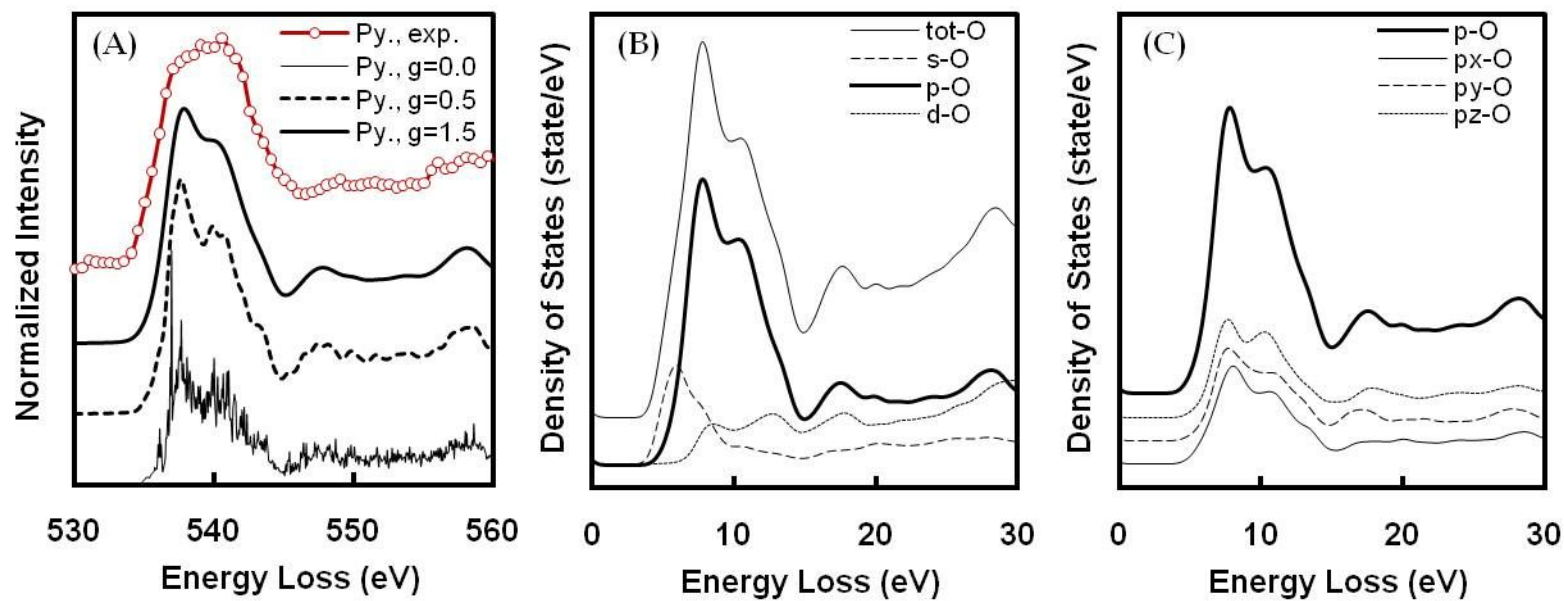


Figure 21. The calculated and experimental results of MgSiO₃ pyroxene (Py; ortho-enstatite). (A) the oxygen K-edge ELNES spectra. (B) the partial density of states of oxygen. (C) the directional components in p-orbital of oxygen.

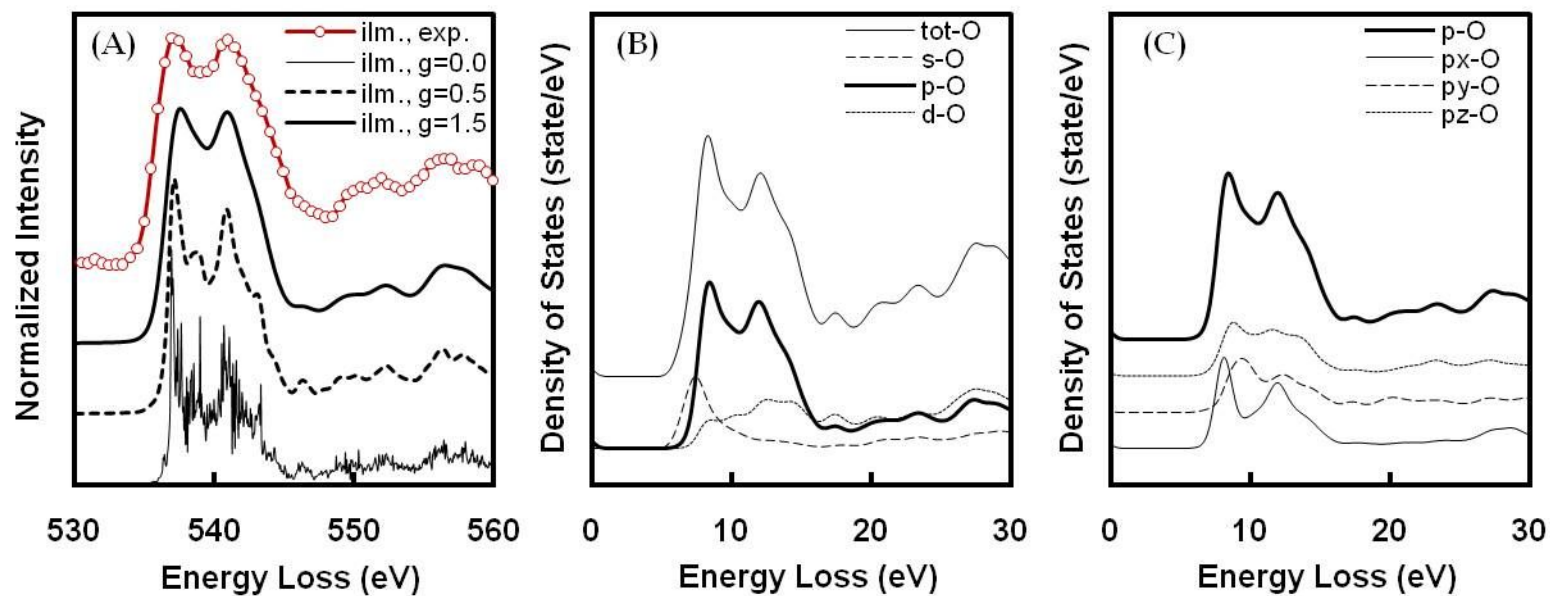


Figure 22. The calculated and experimental results of MgSiO₃ ilmenite (ilm). (A) the oxygen K-edge ELNES spectra. (B) the partial density of states of oxygen. (C) the directional components in p-orbital of oxygen.

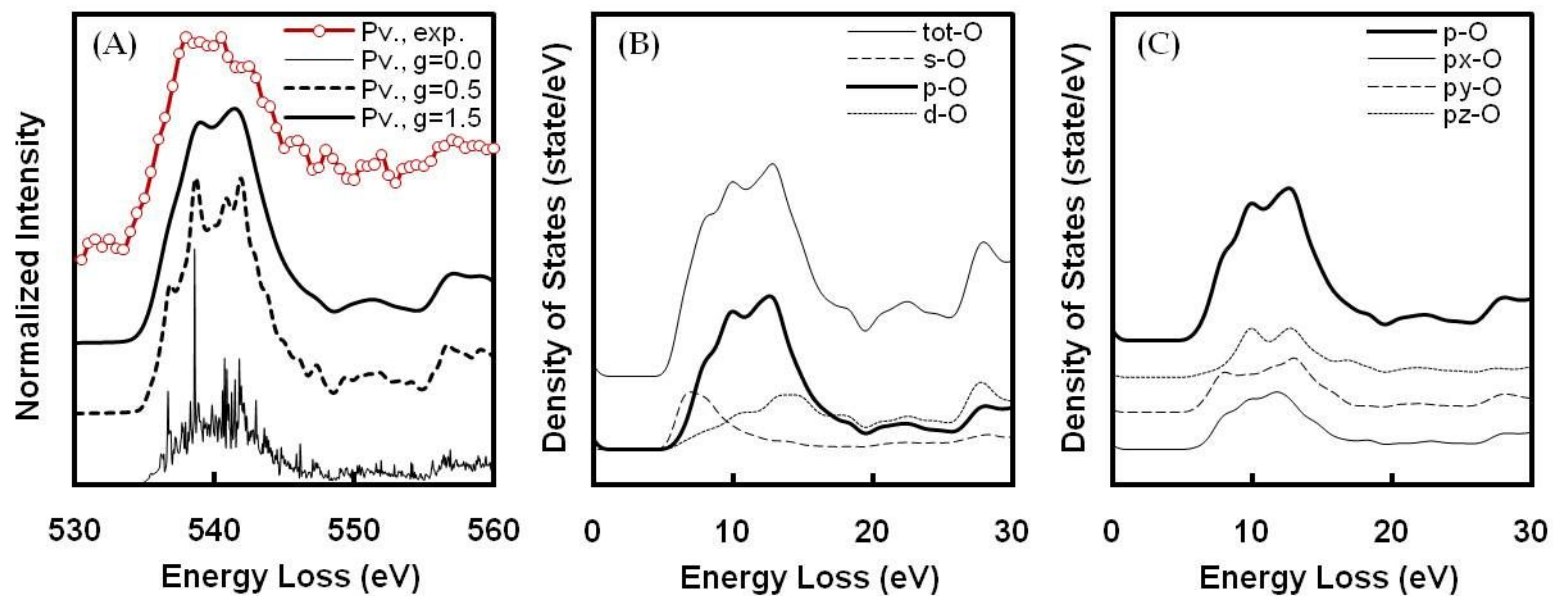


Figure 23. The calculated and experimental results of MgSiO₃ perovskite (Pv). (A) the oxygen K-edge ELNES spectra. (B) the partial density of states of oxygen. (C) the directional components of p-orbital of oxygen.

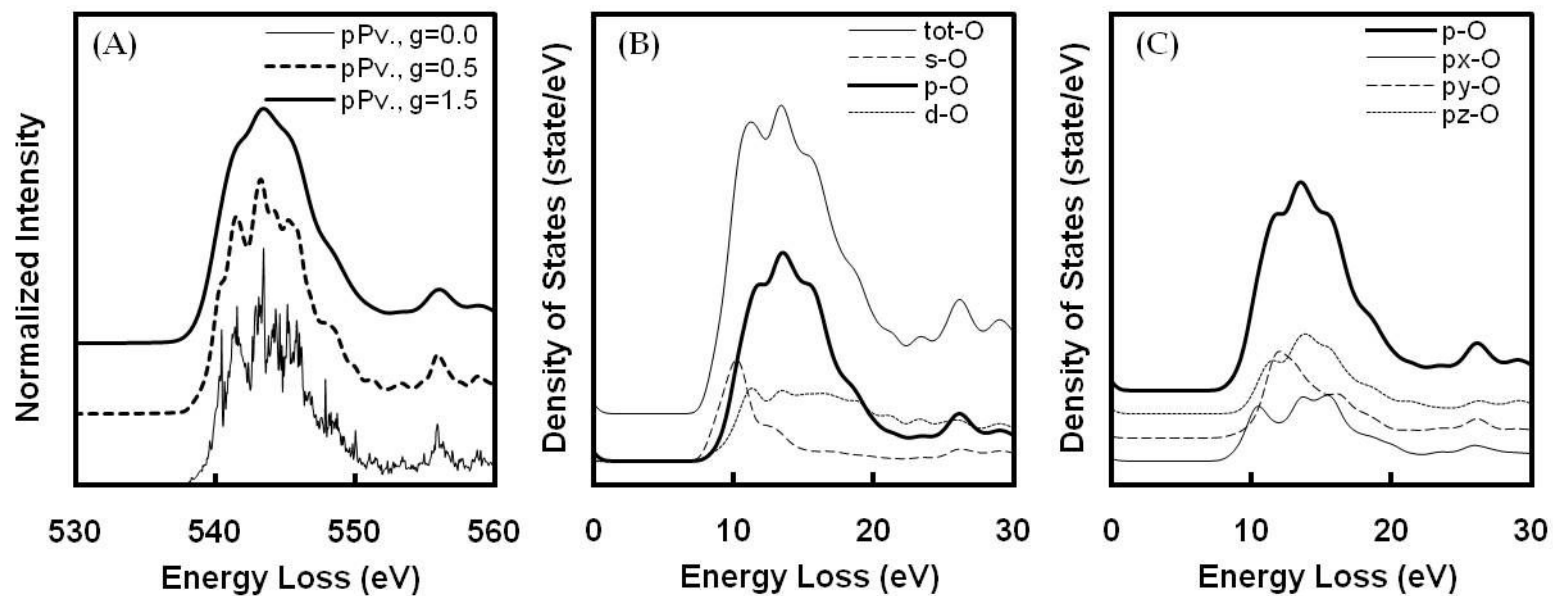


Figure 24. The calculated results of MgSiO₃ post-perovskite (pPv). (A) the oxygen K-edge ELNES spectra. (B) the partial density of states of oxygen. (C) the directional components in p-orbital of oxygen.

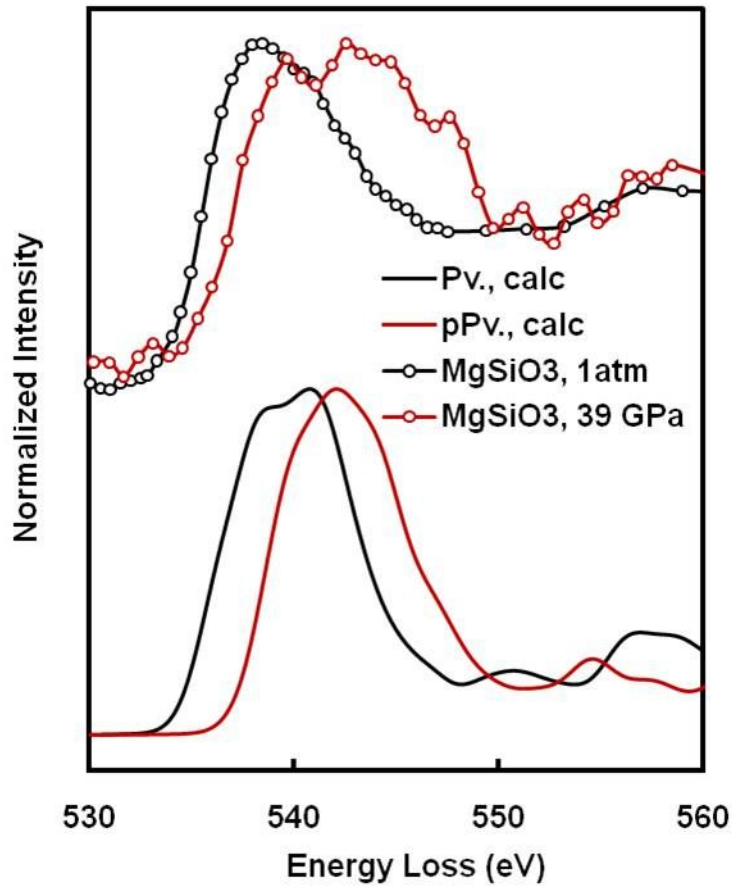


Figure 25. The oxygen K-edge XRS spectra of MgSiO_3 glasses at 1 atm and ≈ 39 GPa and calculated ELNES spectra of MgSiO_3 perovskite (Pv) and post-perovskite (pPv)

References

References from 1 to 18 are used in the first chapter, and from 19 to 50 for the second chapter.

1. Lee, S.K., et al., *Nature of polymerization and properties of silicate melts and glasses at high pressure*. *Geochimica et Cosmochimica Acta*, 2004. **68**(20): p. 4189-4200.
2. Lee, S.K., *Structure of silicate glasses and melts at high pressure: Quantum chemical calculations and solid-state NMR*. *Journal of Physical Chemistry B*, 2004. **108**(19): p. 5889-5900.
3. Hollas, J.M., *Modern Spectroscopy*. 4 ed. 2004: Wiley & Sons, Ltd.
4. Duer, M.J., *Introduction to Solid-State NMR Spectroscopy*. 2004: Blackwell.
5. Levitt, M.H., *Spin Dynamics: Basic of Nuclear Magnetic Resonance*. 2001: Wiley & Sons, Ltd.
6. Levine, I.N., *Quantum Chemistry*. 5 ed. 2006: Prentice Hall.
7. Griffiths, D.J., *Introduction to Quantum Mechanics*. 2 ed. 2005: Prentice Hall.
8. Mysen, B. and P. Richet, *Silicate Glasses and Melts*. *Developments in Geochemistry*. 2005: Elsevier. 35-124.
9. Gibbs, P. *Is glass liquid or solid?* 1997; Available from: <http://math.ucr.edu/home/baez/physics/General/Glass/glass.html>.

10. Lee, S.K. and J.F. Stebbins, *The structure of aluminosilicate glasses: High-resolution O-17 and Al-27 MAS and 3QMAS*. Journal of Physical Chemistry B, 2000. **104**(17): p. 4091-4100.
11. Stebbins, J.F., S.K. Lee, and J.V. Oglesby, *Al-O-Al oxygen sites in crystalline aluminates and aluminosilicate glasses: High-resolution oxygen-17 NMR results*. American Mineralogist, 1999. **84**(5-6): p. 983-986.
12. Charpentier, T., P. Kroll, and F. Mauri, *First-Principles Nuclear Magnetic Resonance Structural Analysis of Vitreous Silica*. Journal of Physical Chemistry C, 2009. **113**(18): p. 7917-7929.
13. Clark, T.M., et al., *Correlated structural distributions in silica glass*. Physical Review B, 2004. **70**(6): p. 8.
14. Bouhifd, M.A., A.P. Jephcoat, and S.P. Kelley, *Argon solubility drop in silicate melts at high pressures: A review of recent experiments*. Chemical Geology, 2008. **256**(3-4): p. 252-258.
15. Bouhifd, M.A. and A.P. Jephcoat, *Aluminium control of argon solubility in silicate melts under pressure*. Nature, 2006. **439**(7079): p. 961-964.
16. Lee, S.K., et al., *X-ray Raman scattering study of MgSiO₃ glass at high pressure: Implication for triclustered MgSiO₃ melt in Earth's mantle*. Proceedings of the National Academy of Sciences of the United States of America, 2008. **105**(23): p. 7925-7929.
17. Chamorro-Perez, E., et al., *Low argon solubility in silicate melts at high pressure*. Nature, 1998. **393**(6683): p. 352-355.
18. White, B.S., M. Brearley, and A. Montana, *Solubility of Argon in Silicate Liquids at High-Pressure*. American Mineralogist, 1989. **74**(5-6): p. 513-529.
19. Tse, J.S., *Ab Initio Molecular Dynamics With Density Functional Theory*. Annual Review of Physical Chemistry, 2002. **53**(1): p. 249-290.

20. Payne, M.C., et al., *Iterative minimization techniques for ab initio total-energy calculations: molecular dynamics and conjugate gradients*. *Reviews of Modern Physics*, 1992. **64**(4): p. 1045.
21. Oganov, A.R. and C.W. Glass, *Crystal structure prediction using ab initio evolutionary techniques: Principles and applications*. *The Journal of Chemical Physics*, 2006. **124**(24): p. 244704-15.
22. Cygan, R.T. and J.D. Kubicki, eds. *Molecular Modeling Theory: Applications in the Geoscience*. *Reviews in Mineralogy and Geochemistry*, ed. J.J. Rosso and P.H. Ribbe. Vol. 42. 2001, The Mineralogical Society of America. 1-30.
23. Neuville, D.R., et al., *The crystal and melt structure of spinel and alumina at high temperature: An in-situ XANES study at the Al and Mg K-edge*. *Geochimica Et Cosmochimica Acta*, 2009. **73**(11): p. 3410-3422.
24. Lin, J.F., et al., *Electronic bonding transition in compressed SiO₂ glass*. *Physical Review B*, 2007. **75**.
25. de Groot, F., *High resolution X-ray emission and X-ray absorption spectroscopy*. *Chemical Reviews*, 2001. **101**(6): p. 1779-1808.
26. Cabaret, D., et al., *Full multiple scattering calculations of the X-ray absorption near edge structure at the magnesium K-edge in pyroxene*. *American Mineralogist*, 1998. **83**(3-4): p. 300-304.
27. Kittel, C., *Introduction to solid state physics*. 8 ed. 2004: Wiley.
28. Ashcroft, N.W. and N.D. Mermin, *Solid State Physics*. 1976: Brooks/Cole.
29. Luitz, J., *Simulation of core level spectra using density functional theory*, in *Engineering Chemistry*. 2006, Technische Universität Wien.
30. Hebert, C., *Practical aspects of running the WIEN2k code for electron spectroscopy*. *Micron*, 2007. **38**(1): p. 12-28.

31. Singh, D.J. and L. Nordstrom, eds. *Planewaves, pseudopotentials, and the LAPW method*. 2nd ed. 2006, Springer.
32. Schwarz, K. and P. Blaha, *Solid state calculations using WIEN2k*. Computational Materials Science, 2003. **28**(2): p. 259-273.
33. Schwarz, K., *DFT calculations of solids with LAPW and WIEN2k*. Journal of Solid State Chemistry, 2003. **176**: p. 319-328.
34. Hebert, C., J. Luitz, and P. Schattschneider, *Improvement of energy loss near edge structure calculation using Wien2k*. Micron, 2003. **34**(3-5): p. 219-225.
35. Schwarz, K., P. Blaha, and G.K.H. Madsen, *Electronic structure calculations of solids using the WIEN2k package for material sciences*. Computer Physics Communications, 2002. **147**(1-2): p. PII S0010-4655(02)00206-0.
36. Blaha, P., et al. *WIEN2k, An augmented plane wave + local orbitals program for calculating crystal properties*. 2001; Available from: <http://www.wien2k.at>.
37. Momma, K. and F. Izumi, *VESTA: a three-dimensional visualization system for electronic and structural analysis*. Journal of Applied Crystallography, 2008. **41**: p. 653-658.
38. Fukui, H., et al., *X-ray Raman scattering for structural investigation of silica/silicate minerals*. Physics and Chemistry of Minerals, 2009. **36**(3): p. 171-181.
39. Gaudio, S.J., S. Sen, and C.E. Lesher, *Pressure-induced structural changes and densification of vitreous MgSiO₃*. Geochimica et Cosmochimica Acta, 2008. **72**(4): p. 1222-1230.
40. Hemley, R.J., ed. *Ultrahigh-pressure mineralogy: Physics and chemistry of the Earth's deep interior*. Reviews in mineralogy, ed. P.H. Ribbe. Vol. 37. 1998, Mineralogical society of America: Washington, DC.
41. Pijush and K. K., *Fluid Mechanics*. 3rd ed. 2004: Elsevier.

42. March, N.H. and M.P. Tosi, *Introduction to Liquid state physics*. 2004: World Scientific Publishing.
43. Pepin, R.O., *On The Origin and Early Evolution of Terrestrial Planet Atmospheres and Meteoritic Volatiles*. *Icarus*, 1991. **92**(1): p. 2-79.
44. Lee, S.K., et al., *Oxygen-17 nuclear magnetic resonance study of the structure of mixed cation calcium-sodium silicate glasses at high pressure: Implications for molecular link to element partitioning between silicate liquids and crystals*. *Journal of Physical Chemistry B*, 2008. **112**(37): p. 11756-11761.
45. Glinnrmann, et al., *Crystal structures of the low-temperature quartz-type phases of SiO₂ and GeO₂ at elevated pressure*. *Zeitschrift für Kristallographie*, 1992. **198**: p. 177-212.
46. Levien, L. and C.T. Prewitt, *High-Pressure Crystal-Structure and Compressibility of Coesite*. *American Mineralogist*, 1981. **66**(3-4): p. 324-333.
47. Ross, N.L., et al., *High-Pressure Crystal-Chemistry of Stishovite*. *American Mineralogist*, 1990. **75**(7-8): p. 739-747.
48. Horiuchi, H., E. Ito, and D.J. Weidner, *Perovskite-Type MgSiO₃ - Single-Crystal X-ray Diffraction Study*. *American Mineralogist*, 1987. **72**(3-4): p. 357-360.
49. Ohashi, Y., *Polysynthetically-Twinned Structures of Enstatite and Wollastonite*. *Physics and Chemistry of Minerals*, 1984. **10**(5): p. 217-229.
50. Murakami, M., et al., *Post-perovskite phase transition in MgSiO₃*. *Science*, 2004. **304**(5672): p. 855-858.

압력에 의한 규산염 비정질 또는 용융체의 원자 구조의 변화를 이해하는 것은 지구 내부의 결정-용융상의 경계부분에서 일어나는 원소의 분배현상 (crystal-melts elements partitioning), 화학적 분화현상 (chemical differentiation), 불활성 기체의 용해도 변화와 같은 현상들을 이해하는데 매우 중요하다. 하지만 비정질 물질의 원자 구조를 직접적으로 분석할 수 있는 알맞은 분석 방법의 부재로 인하여, 위와 같은 규산염 비정질 물질의 구조에 대한 연구는 비교적 최근까지 여러 가지 방면에서 부족한 상황이었다. 근래에 접어들어, 고해상도 고상 핵자기 공명 분광장치 (high-resolution solid-state nuclear magnetic resonance spectrometer; NMR), 비-공명 X-선 Raman 산란 (non-resonant x-ray Raman scattering) 실험, 양자화학계산 (quantum chemical calculations; first-principle calculations)의 발전에 힘입어 규산염 비정질 물질의 원자 구조를 직접적으로 상세하게 파악할 수 있게 되었다. 본 연구에서는 NMR 의 1D MAS 와 2D 3QMAS 실험을 이용하여 Na 이 첨가된 알루미늄-규산염 (Na-aluminosilicate) 비정질 물질의 시료들에 나타나는 압력에 의한 원자단위에서의 구조적 변화, 위상적 변화를 성분과 압력의 변화에 따른 체계적인 변화를 확인하였다. 그리고 양자화학계산을 통한 산소원자의 ELENES (oxygen K-edge ELNES; energy-loss near-edge structure) 스펙트럼을 얻어 압력의 변화에 따른 마그네슘-규산염 (Mg-silicate) 비정질 물질의 국부적인 전기적 환경 (local

electronic environments)의 변화를 확인하고 이를 관련된 이전 실험 결과와 비교 분석하였다.

첫 번째 장에서는, ^{27}Al 과 ^{17}O 의 1D MAS 와 2D 3QMAS 실험을 통하여 Na 이 첨가된 알루미늄-규산염 비정질 물질을, 그 성분 조성의 변화와 압력 조건의 변화 (1 기압 ~ 8 GPa)에 따라 분석하여 연결구조 교란 양이온 (network modifying cation)으로 작용하는 Na 이 압력에 의한 규산염 비정질 물질의 구조 변화에 미치는 영향을 조사하였다. 이러한 실험의 결과들은 연결구조 교란 양이온이 압력에 의한 규산염 비정질 물질의 구조 변화에 미치는 영향을 뚜렷하게 보여주며, 낮은 압력에서 상대적으로 중합도가 높은 규산염 비정질 물질이 고압의 상태에서 더 높은 중합도를 갖는 구조를 형성할 수 있는 가능성을 시사하고 있다.

두 번째 장에서는, FP-LAPW (full-potential linearized augmented plane wave) 방법론을 적용한 계산 프로그램을 이용하여 얻은 MgSiO_3 와 SiO_2 결정질 동질이상 물질들의 산소 K-edge ELNES 스펙트럼을 얻고, 이를 통하여 비정질 MgSiO_3 의 고압상태에서 전기적 연결구조 (electronic bonding structure)에 대한 정보를 얻을 수 있었다. 계산된 산소원자의 ELNES 스펙트럼은 고압상태의 동질이상인 perovskite 와 post-perovskite 에 대하여 특징적인 스펙트럼을 보여준다. MgSiO_3 perovskite 의 $^{16}\text{Si-O-}^{16}\text{Si}$ (i.e., corner-sharing oxygen)는 ≈ 540 eV 부근에서, MgSiO_3 post-perovskite 의 $^{16}\text{Si-O-}2^{16}\text{Si}$ (i.e., edge-sharing oxygen)은 ≈ 545 eV 부근에서 스펙트럼의 최대값을 보여주고 있다. 이러한 스펙트럼의

변화는 비정질 MgSiO_3 의 압력의 증가에 따른 스펙트럼의 변화와 유사한 양상을 보여준다. MgSiO_3 post-perovskite 의 edge-sharing 산소와 산소 tri-clusters (i.e., 고배위수의 Si 원자 3 개가 연결된 산소원자)와 유사한 원자 구조 (atomic configuration)을 갖고 있는 것으로 유추하여, 현재까지의 결과가 이전 연구에서 고압상태의 비정질 Mg-규산염 물질에서 나타난 ≈ 545 eV 가 산소 tri-clusters 에서 기원했다는 제안은 옳은 것으로 생각된다. 위와 같은 실험 및 계산 결과들은 압력에 의한 비정질 규산염 물질들의 원자 구조의 변화와 연결구조 교란 양이온이 이러한 현상에 미치는 영향들을 설명해주고 있다. 이를 통하여 지구 내부의 압력의 증가에 따른 규산염 용융체의 원자 구조의 변화를 고려함으로써 이전 연구들로부터 얻어진 단편적인 지식들에 대한 더욱 상세하고 체계적인 이해를 도모하며, 전 지구적인 시스템의 진화를 이해하는데 있어서도 중요한 정보들을 제공할 수 있을 것으로 기대된다.

주요어: 비정질 Na-알루미노 규산염, 고압, 연결구조 교란 양이온, 고상 핵자기공명 분광장치, 산소원자 K-edge

학번: 2008-20409

감사의 글

NMR 이라는 실험 장비와 비탄선 X-선 산란 실험이나 관련된 양자화학계산들은 대학원에 입학하기 전에는 매우 생소하고 동떨어진 주제들이었습니다. 그렇기 때문에, 처음 연구를 시작하며 실험과 계산을 배우는 과정에서 많은 실수와 어려움이 있었습니다. 하지만 지도 교수님이신 이성근 교수님의 많은 지도와 관련 학과의 여러 교수님들의 뛰어난 강의를 통하여 다양한 경험과 지식을 쌓을 수 있었고, 덕분에 미력하나마 이 글을 완성할 수 있었습니다. 먼저, 바쁘신 와중에도 졸작의 심사에 시간을 할애하여 주신 이용일 교수님과 이준기 교수님께 감사의 인사를 올립니다. 그리고 NMR 실험에 이용된 고압 시료의 합성에 도움을 주신 동경대학교 지진연구소의 三部賢治 (Mibe Kenji) 교수님께도 감사 드립니다.

같은 연구실에서 학회 때를 비롯하여 여러 가지 부족한 점을 도와주셨던 이범한 선배님께도 감사 드립니다. 대학원 생활을 하는 도중에 여러 가지 어려움이 많았지만 김현나 선배님의 조언과 도움이 있어 여러 가지를 극복할 수 있었습니다. 그리고 같이 대학원에 입학하여 어느덧 2 년이라는 시간을 함께 보내고 여러 가지 일들에 신경을 써준 박선영 양에게도 감사의 말을 드립니다. 지난 학기에 대학원에 입학하여 연구실의 일원으로 합류하여 연구실 생활에 많은 도움을 주고 있는 김효임, 김은정 후배님들께도 감사 드립니다. 다른

연구실에 있지만, 여러 가지 상담을 해주고 도움을 주신 한영철 선배님께도 감사의 말씀을 드립니다.

대학원에 입학한 이후로는 많이 소홀해진 것 같지만, 6 년이라는 시간 동안 얼굴을 보며 술잔을 기울였던 재석이, 성재, 지금은 군복무중인 승윤이, 큰형님, 길 건너 동네에 살면서 수시로 술친구가 되어준 희근이 항상 내 불평불만을 들어줘서 고맙다는 말을 전하고 싶습니다. 말상대가 되어주고 여러 가지 컴퓨터 관련 문제를 던져주어 스트레스를 푸는데 도움을 줬던 지원누나에게도 작은 감사를 전합니다. 그리고 후배이지만 후배 같지 않고 잘 어울려 줬던 세진이와 방원이에게 감사의 말을 전합니다. 그리고 일일이 열거할 수는 없지만, 여러 도움을 주고 받았던, 대학 동기 친구들에게 모두 감사의 말을 전하고 싶습니다.

마지막으로 항상 저를 생각해주시고, 지금까지 물심양면으로 지원을 해주신 부모님께 가장 깊은 감사의 말씀을 올립니다.